Sharp, Graham James (2015) *Metamaterials and optical sensing at visible and near infra-red wavelengths.* PhD thesis.

Glasgow Theses Service
http://theses.gla.ac.uk/
theses@gla.ac.uk

Metamaterials and optical sensing at visible and near infra-red wavelengths

Graham James Sharp

November 2014

A thesis submitted to the
School of Engineering
University of Glasgow

In fulfilment of the degree of
Doctor of Philosophy (Ph.D)

Abstract

Developments in the field of optical sensing have seen the creation of a wide variety of new structures and materials. These include metamaterial sensors, which comprise of nanostructures with physical dimensions smaller than the wavelength of light. Two of the most widely researched metamaterial structures are the Split Ring Resonator (SRR) and fishnet. Both of these structures can be physically altered (in terms of geometry, material composition or periodicity) to exhibit plasmonic resonances at frequencies as far as the visible regime. The near-infrared frequency range is of particular interest with regard to optical sensing as many molecular absorption bands can be found here.

This thesis studies the effectiveness of different designs of optical sensors and the fabrication techniques used to produce them. By changing the dimensions and constituent metal of SRRs, their resonance response is analysed and parameters such as the Quality factor (Q-factor) obtained. The sensitivity of a single gap SRR to the presence of a thin film and localised block of Polymethyl methacrylate (PMMA) is experimentally measured. By changing the position of the localised PMMA block, it can be used as a material probe for the sensor, enabling the areas of greatest sensitivity to be determined. The sensitivity of the SRR is found to greatly depend on the polarisation of the incident electric field with respect to the structure, varying between 143 nm/RIU and 612 nm/RIU when PMMA is positioned at the gap in the ring. Complementary simulations offer additional insight into the behaviour of the structure at a range of frequencies. In addition to plasmonic structures, the fabrication and characterisation of a polymer photonic biosensor is also studied. This sensor utilises a distributed Bragg reflector (DBR) cavity adjacent to a rib waveguide to create a narrow stop-band that can potentially be used in the sensing of specifically targeted biological analytes.

For optical sensors to make a transition from research environment to commercial application, the costly fabrication techniques associated with the research and development of nanostructures need to be avoided. Nanoimprint lithography (NIL) offers multiple benefits in terms of cost, fabrication time and the patterning of large areas and is well suited to the commercial sector. NIL has been extensively used throughout the work detailed in this thesis to pattern SRRs, fishnets and polymer sensors.

Publications

First Author

1. **G. J. Sharp,** S. I. Khan, A. Z. Khokhar, R. M. De La Rue, "Negative index fishnet with nanopillars formed by direct nanoimprint lithography." Materials Research Express, 1, 045802, 2014.

2. **G. J. Sharp,** S.I. Khan, A. Z. Khokhar, R. M. De La Rue, N. P. Johnson, "Negative index fishnet structures with nanopillars formed by nanoimprint lithography." SPIE Photonics Europe, 2014, Brussels, Belgium.

3. **G. J. Sharp,** M. Yuce, X. Hu, M. Sinworapun, A. Z. Khokhar, N. P. Johnson, "Metamaterial fishnet structure formed from nanoimprint lithography." Metamaterials VIII, 2013, Prague, Czech Republic.

4. **G. J. Sharp,** A. Z. Khokhar, N. P. Johnson, "Fabrication of 70nm split ring resonators by nanoimprint lithography." SPIE Conference 8423: Metamaterials, 2012, Brussels Belgium.

5. **G. J. Sharp,** A. Z. Khokhar, S. G. McMeekin, N. P. Johnson, "Fabrication of 65 nm wide Split Ring Resonators by Nanoimprint Lithography." Micro- and Nano-Photonic Materials and Devices, MINAP, 2012, Trento, Italy.

Co-authored

1. N.P. Johnson, B. Lahiri, **G.J. Sharp,** I. G. Mbomson, R. M. De La Rue, S. G. McMeekin, "Nano-plasmonic sensors from asymmetric split-ring resonators (A-SRRs)". SPIE Photonics Europe, 2014, Brussels, Belgium.

2. S. I. Khan, **G. J. Sharp,** R. M. De La Rue, T. D. Drysdale, N.P. Johnson, "Modelling angle resolved complex reflection and transmission coefficients from fishnet structure formed from nanoimprint lithography." SPIE Photonics Europe, 2014, Brussels, Belgium.

3. N. P. Johnson, B. Lahiri, **G. J. Sharp,** R. M. De La Rue, S. McMeekin, "Fano resonances of organic films on asymmetric split-ring resonators." 7th International Congress on Advanced Electromagnetic Materials in Microwaves and Optics, 2013, Bordeaux, France.

4. N. P. Johnson, **G. J. Sharp,** M. Yuce, X. Hu, M. Sinworapun, A. Z. Khokhar, "Metamaterial fishnet structures and small (70 nm) split ring resonators formed by nanoimprint lithography." 15th International Conference on Transparent Optical Networks (ICTON 2013), 2013, Cartagena, Spain.

5. D. Giannone, F. Dortu, D. Bernier, N. P. Johnson, **G. J. Sharp,** L. Hou, A. Z. Khokhar, P. Furjes, S. Kurunczi, P. Petrik, R. Horvath, T. Aalto, K. Kolari, S. Ylinen, T. Haatainen, H. Egger, "NIL fabrication of a polymer-based photonic sensor device in P3SENS project." Organic Photonics V, 2012, Brussels, Belgium.

6. N. P. Johnson, B. Lahiri, **G. J. Sharp,** A. Z. Khokhar, "Nanophotonic Sensors." Micro- and Nano-Photonic Materials and Devices, MINAP, 2012, Trento, Italy.

7. N. P. Johnson, B. Lahiri, **G. J. Sharp,** G. A. Rahman, P. Velha, A. Z. Khokhar, R.M. De La Rue, S. McMeekin, "Photonic sensors at the nanoscale." Transparent Optical Networks (ICTON), 14th International Conference on, 2012, Coventry, UK.

8. F. Dortu, H. Egger, K. Kolari, T. Haatainen, P. Furjes, Z. Fekete, D. Bernier, **G. J. Sharp,** B. Lahiri, S. Kurunczi, J. C. Sanchez, N. Turck, P. Petrik, D. Patko, R. Horvath, S. Eiden, T. Aalto, S. Watts, N. P. Johnson, R. M. De La Rue, D. Giannone, "Design and process development of a photonic crystal polymer biosensor for point of care diagnostics." Proceedings of SPIE: OSA Biomedical Optics, 8087, 2011, Munich, Germany.

9. R. M. De La Rue, M. Sorel, A. Samarelli, P. Velha, M. Strain, N. P. Johnson, **G. J. Sharp,** F. Rahman, A. Z. Khokhar, D. S. Macintyre, S. G. McMeekin, B. Lahiri, "Planar nanophotonic devices and integration technologies." Photonics & Micro- and Nano- structured Materials, 841402, 2011, Yerevan, Armenia.

Table of Contents

List of Tables

List of Figures

Acknowledgement

To begin my acknowledgements by mentioning anyone other than my supervisor would be disingenuous in the least and heartless at most. Throughout my research, Dr Nigel P. Johnson has provided immeasurable guidance, support and encouragement. It is no exaggeration to say that I owe a huge amount of my academic and personal development to him and the experiences he has provided to me. For that I will be forever grateful.

Prof. Richard De La Rue has been a source of great inspiration and guidance for me. His vast knowledge spans many fields of study and I have always enjoyed our numerous discussions and have found his suggestions to be enormously helpful and fruitful. Despite his many collaborations, boundless experience and multiple interests he has always been very generous in finding time to meet with me and discuss my work. To him I can only say thank you, merci, dziękuję and спасибо.

I have had the great fortune to work with many talented people in a number of capacities. I owe a great debt of gratitude to Dr Basudev Lahiri and Dr Ali Z. Khokhar, particularly in the early stages of my PhD research, in teaching me many of the aspects of cleanroom fabrication and optical characterisation. They have both always been receptive to my numerous questions and queries and keen to offer assistance if needed. I would especially like to thank Dr Lahiri for the many discussions we have shared concerning metamaterials and, in particular, the split ring resonator.

There is no doubt that without the numerous technicians present in the James Watt Nanofabrication Centre (JWNC) none of the fabricated devices and structures contained in this thesis would exist. Their skill and knowledge in nanofabrication is surpassed only by their helpfulness and good humour. While fabrication tools and equipment can come and go, to my mind their input and dedication to the JWNC and its users is irreplaceable.

I would like to acknowledge the financial support from the EPSRC in the form of a doctoral scholarship.

Finally, I would like to thank my friends. They may not know it and I may never say it, but their support and encouragement has often been a source of strength for me throughout my studies and I thank them wholeheartedly.

Author's Declaration

I declare that, except where explicit reference is made to the contribution of others, that this thesis is the result of my own work and has not been submitted for any other degree at the University of Glasgow or any other institution.

Graham J. Sharp

Definitions and abbreviations

AFM	Atomic force microscopy
A-SRR	Asymmetric-split ring resonator
A.U.	Arbitrary unit
CT	Computer tomography
E-beam	Electron-beam
EBL	Electron beam lithography
EM	Electromagnetic
EOT	Extraordinary optical transmission
F_{13}-OTCS	Tridecafluoro-1,1,2,2-tetrahydrooctyl-Trichlorosilane
FDTD	Finite-difference time-domain
FIB	Focused ion beam
FOM	Figure of merit
FTIR	Fourier transform infrared
HSQ	Hydrogen silsesquioxane
ICP	Inductively coupled plasma
IPA	Isopropanol
LSPR	Localised surface plasmon resonance
MCT	Mercury-cadmium-telluride
MIR	Mid-infrared
MRI	Magnetic resonance imaging
NEP	N-Ethyl-2-Pyrrolidone
NIL	Nanoimprint lithography
NIM	Negative index material

NIR	Near-infrared
ODT	Octadecanthiol
PI	Polyimide
PMMA	Polymethyl methacrylate
Q-factor	Quality factor
RF	Radio frequency
RIE	Reactive ion etching
RIU	Refractive index unit
RO	Reverse osmosis
SEM	Scanning electron microscope
SNR	Signal-Noise ratio
SOI	Silicon on insulator
SP	Surface plasmon
SPP	Surface plasmon polariton
SPR	Surface plasmon resonance
SRR	Split ring resonator
TE	Transverse electric
TEOS	Tetraethyl orthosilicate
TIA	Transient ischemic attack
TIR	Total internal reflection
TM	Transverse magnetic
TMAH	Tetramethylammonium hydroxide
UV	Ultraviolet

Overview of chapter cover images

Chapter 1

Micrograph of a gold Asymmetric-split ring resonator on silicon.

Chapter 2

A periodic array of gold nano-sized "L-shapes".

Chapter 3

Array of nanoimprinted aluminium split ring resonators.

Chapter 4

Split ring resonator with a block of PMMA localised at the gap of the ring.

Chapter 5

A directly imprinted single active layer metamaterial fishnet with nanopillars.

Chapter 6

A Bragg grating cavity on a silicon nanoimprint stamp used for patterning polymers.

Chapter 7

A gold "nano-mouth" array fabricated using colloidal lithography and pattern transfer technique.

Chapter 1

Introduction
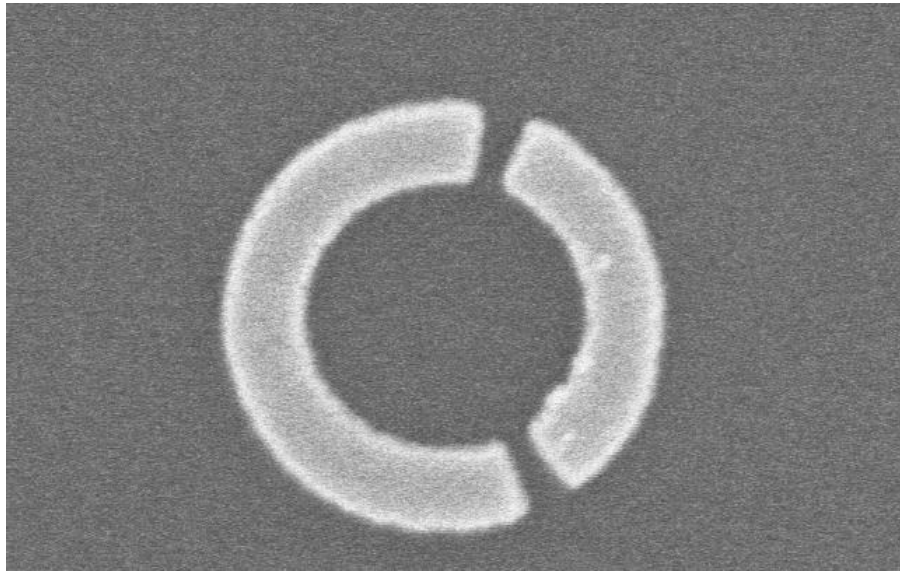
1.1 An introduction to metamaterials

The derivation of the word "metamaterial" helps offer some brief insight into their characteristics and functionality. The prefix "meta" originally comes from the Greek for "after" or "beyond". With time the meaning of the word has developed to denote a change in or development to the discipline or entity appended to it. Examples include metaphysics and metaphilosophy. Applying this meaning to "materials", one can sensibly come to the conclusion that metamaterials offer something different to conventional materials that is beyond their typical capabilities.

Metamaterials are synthetic materials consisting of manmade micro and nanoscale structures designed to interact in a specific way with incident light. These structures, which can take a variety of different shapes and configurations, have smaller dimensions than the wavelength of light and respond to it in a way unlike any naturally occurring material. These irregular responses can include, but are not limited to, a negative index of refraction [1], superlensing to achieve resolution beyond the diffraction limit [2], electromagnetic cloaking [3] and enhanced absorption [4]. Metamaterial applications (and potential applications) utilise these features for use with optical sensors, antennas, high resolution imaging and absorbers amongst others.

Metamaterials consist of an array specially arranged structures, each fabricated using conventional materials that are comprised of elements and the atoms within them. These structures, sometimes referred to as "artificial molecules" or "meta-atoms", interact or control incident electromagnetic waves. The response of or change in the electromagnetic waves is dependent on the shape of the artificial molecule, its size, its constituent elements as well as their periodic arrangement and proximity to each other or indeed other materials or structures. Therefore by altering these parameters the electromagnetic response can be adapted, or "tuned", as desired. In this way, these artificial molecules can be thought of as acting in a similar sense to the atoms in natural materials [5]. With the artificial molecules smaller in dimension than the wavelength of incident light, the metamaterial can be considered as effectively a homogeneous material. The relationship between the size and shape of metamaterials and their response gives

rise to the importance of fabrication techniques and the need to manufacture increasingly small or complicated structures.

1. 2 Fundamental principles of electromagnetics

As a field of optoelectronics that can be described using classical electromagnetic theory (as opposed to quantum theory), metamaterials can be understood by applying Maxwell's equations. These equations set out the relationship between the electric and magnetic field components of an electromagnetic wave. Visible, near-infrared and mid-infrared light is of course a particular frequency range of the electromagnetic spectrum. When solved in the frequency domain, when the fields oscillate harmonically in time with angular frequency ω, they can be written as:

$$\nabla \times E(r) = -j\omega B(r) \tag{1.1}$$

$$\nabla \times H(r) = j\omega D(r) + J(r) \tag{1.2}$$

$$\nabla \cdot D(r) = \rho(r) \tag{1.3}$$

$$\nabla \cdot B(r) = 0 \tag{1.4}$$

E denotes the electric field vector, H the magnetic field vector, D the electric flux density, ρ the scalar charge density, J the current density vector and B the magnetic flux density. When written in the above form, all of the above quantities are independent of time and are functions of space (r) only. As well as a real component the solutions also have a complex part, signified by j. Maxwell's equations can be applied, in various forms and with supplementary constitutive relations, to metamaterials and solved to calculate their electromagnetic response. Constitutive relations govern how the electric and magnetic flux relate to the electric and magnetic field respectively. In an isotopic medium (one in which the electromagnetic response is independent of the field vector direction), the constitutive relationships for both D and B are:

$$D = \varepsilon E \qquad\qquad\qquad (1.5)$$

$$B = \mu H \qquad\qquad\qquad (1.6)$$

Where ε is the electric permittivity and μ is the magnetic permeability. In this linear, isotropic example the permittivity is a scalar quantity that signifies the extent of the electric flux that exists per unit charge in a given medium. The permeability can be viewed as the magnetic equivalent of ε, denoting the response of the magnetic flux of a material to the magnetic field. When expressed as a function of frequency, both ε and μ can have real and imaginary components.

The electric permeability defines the response of a material to the electric field and can be expressed as

$$\varepsilon = \varepsilon_r \varepsilon_0 \qquad\qquad\qquad (1.7)$$

where ε_r is the relative permittivity of the material and ε_0 is the permittivity of free space. Likewise the magnetic permeability defines the material response to the magnetic field and is expressed as

$$\mu = \mu_r \mu_0 \qquad\qquad\qquad (1.8)$$

where μ_r is the relative permeability of the material and μ_0 is the permeability of free space.

1.2.1 Refractive index

Both the permittivity and permeability of a material are intrinsic in determining its refractive index. The refractive index, sometimes referred to as RI, the index of refraction and denoted by "n", is the ratio of the phase velocity of an electromagnetic wave in a vacuum and the phase velocity of the same wave propagating in a given medium. All materials whether naturally occurring or synthetic have an associated refractive index. The refractive index can be denoted by

$$n = \frac{c}{v} \qquad\qquad\qquad (1.9)$$

Where n is the refractive index, c is the phase velocity of the electromagnetic wave in a vacuum and v is the velocity of the wave in a given medium. For this reason a vacuum has an n value of 1. For convenience this is regularly assumed to be the refractive index of air. The RI of a material is dependent on its optical density (not to be confused with physical density) which determines the velocity at which the electromagnetic wave propagates through it. The optical density of a medium concerns the ease at which an electromagnetic wave can propagate without hindrance from the atoms that form the said material. The unrelated physical density is simply the ratio of physical mass to volume. A wave will propagate with a slower velocity through a highly optically dense material than a material that is less optically dense.

The refractive index of a medium does not remain constant but changes depending on the wavelength of the incident wave. The extent of which n changes with λ is governed by the particular material the wave is interacting with. This change in n is brought about by the relationship

$$c = \lambda \times f \tag{1.10}$$

with c representing the speed of the propagating wave, λ the wavelength and f the frequency. As previously stated ε and μ are vitally important in determining n and in an isotropic medium are related by [5]

$$n = \sqrt{\varepsilon_r \mu_r} \tag{1.11}$$

where the symbols have their usual meanings. By including the complex imaginary parts of ε and μ we can derive a complex value of n, with both real and imaginary components.

$$\varepsilon = \varepsilon' + j\varepsilon'' \tag{1.12}$$

$$\mu = \mu' + j\mu'' \tag{1.13}$$

and considering equation 1.11,

$$n = n' + jn'' \tag{1.14}$$

The real part of the refractive index, *n'*, indicates the magnitude by which the phase velocity of light is decreased when compared with a vacuum. The imaginary part of n denotes the optical extinction, or losses, associated with the medium and is used to produce a figure of merit (FOM), a dimensionless number derived from the ratio of the component governing the ease at which the wave can propagate (real part) and the optical extinction of the medium (imaginary part).

$$FOM = \frac{Re(n)}{Im(n)} \qquad\qquad (1.15)$$

1.2.2 Negative refractive index

All naturally occurring materials have a refractive index real part that is positive, i.e. above zero. However metamaterials have the potential to exhibit a negative refractive index where n < 0. It should be stressed that it is not a conditional requirement that a medium has a negative refractive index in order to be termed a metamaterial, only that it has fabricated features that are smaller in dimension to the wavelength of incident radiation. The concept of a material exhibiting a negative refractive index was proposed by Victor Veselago, suggesting it as a result of the material possessing both a negative permittivity and permeability [7]. In his 1968 paper, Veselago gives four varying combinations with regard to positive and negative values of both ε and μ and discusses the significance of each. By defining four quadrants using an x and y axis, ε and μ can be categorised as either both positive, both negative, ε positive and μ negative or ε negative and μ positive. This can be seen in figure 1.1. The response (and indeed the strength of the response) depends not only on which of the four quadrants a material falls into, but also the ratio of the real parts of ε and μ to their respective complex components.
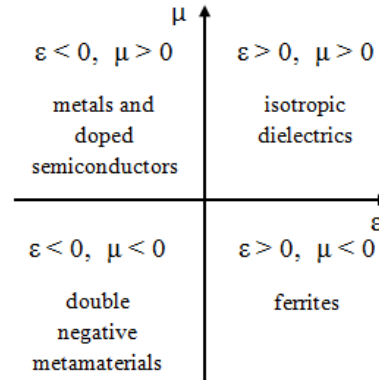
Figure 1.1: Diagram showing the four separate positive and negative combinations of both permittivity and permeability and the type of materials that exhibit those properties. The values of ε and μ can change with wavelength, meaning materials cannot always be confined to a single quadrant.

Taking equations 1.11, 1.12 and 1.13 into consideration, a negative refractive index can be achieved if:

$$\varepsilon'|\mu| + \mu'|\varepsilon| < 0 \tag{1.16}$$

Obeying this equation ensures a negative real part of the refractive index. If both ε' and μ' are less than zero (often termed "double negative") the conditions for a negative real part of n will always be satisfied. However n' can still be negative if, as is the case in some metals, μ' is positive and ε' is sufficiently negative in value. In these circumstances the related FOM is generally smaller than that of double negative metamaterials.

The refractive index, or more specifically a refractive index change, also determines the direction of wave propagation as well as its phase velocity. In a material with a negative refractive index real part, the phase velocity will travel directly against the propagating energy flow [2]. When a wave of light travels from one medium into another medium with a different refractive index, the wave direction will change as a result of refraction. Snell's law, also known as the law of refraction, states that when light passes from one medium (1) to another (2):

$$\frac{sin\theta_1}{sin\theta_2} = \frac{v_1}{v_2} = \frac{n_2}{n_1} \tag{1.17}$$

where θ_1 is the angle of incidence from the normal, θ_2 is the refracted angle in relation to the normal, v is the phase velocity in the respective medium and n is the refractive index of the respective medium. Snell's law can be applied to metamaterials as well as conventional positive index media. As figure 1.2 shows, when light passes from a low index medium (for example air, n = 1) into a higher index medium, it is refracts to the right of the normal. Replacing the high index medium with one with a negative index (n_2 < 0) sees the light refract to the opposite of the normal. In such materials, where both ε and μ are less than zero, the phase velocity of the propagating wave is anti-parallel to the Poynting vector direction and the commonly cited "right-hand rule" (used to donate electric and magnetic field vectors) does not apply. For this reason media that exhibit a negative refractive index were termed as "left-handed" by Veslago [7]. They are also sometimes known as negative index materials (NIMs). Irrespective of whether n_1 and n_2 are positive or negative, the angle of refraction is determined by the magnitude of both n values and their combined ratio, as well of course as the angle of incidence, θ_1. Snell's law does not consider the presence of reflected light at the refractive index interface and the subsequent change in amplitude of the refracted wave. This can be explained using Fresnel equations.
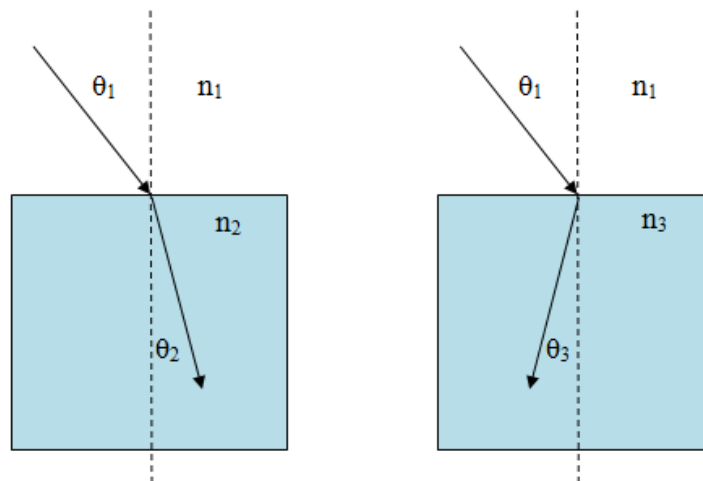
Figure 1.2: Light refracts differently when passing into a medium with a negative index compared to one with a positive index, although Snell's law still applies in both cases.

In the above left example of figure 1.2, light passes from one medium (with refractive index n_1) to another medium (refractive index n_2), where n_1 < n_2 but both are positive in magnitude. The example on the right shows light passing from medium with index n_1 to a medium with index n_3, where n_3 is negative. The light

in this latter example can be seen to refract "backwards", i.e. at a negative angle (θ_3) with respect to the normal.

1.2.3 Total internal reflection & the critical angle

It should be noted that depending on the refractive index contrast between two media, Snell's law cannot be applied to all angles of incidence. Under certain circumstances under Snell's law, when light passes from a high index medium to a medium with a lower index, a large angle of incidence would require the sine of the angle of refraction to be larger than 1. This is of course is an impossibility. Rather, when the light is incident upon the material interface at a large enough angle to the normal it is completely reflected within the high index medium. This is called "total internal reflection" (TIR). Light will only continue to be refracted into the low index medium when the incident light is at an angle less than what is termed the critical angle, θ_{crit}, defined as

$$\theta_{crit} = arcsin\left(\frac{n_2}{n_1}\right) \quad\quad\quad (1.18)$$

Light incident upon the boundary at the critical angle is refracted so that it travels along the interface between the two materials. Increasing the angle of incidence above the critical angle sees the occurrence of TIR. Total internal reflection is of particular importance in the propagation of light along a waveguide. To ensure losses are kept to a minimum and transmission is high, a significant contrast in the refractive index between both media is desirable. With a greater refractive index contrast the critical angle is reduced in value meaning less light is refracted and more light is confined to the waveguide, assuming light is primarily propagating parallel to the material boundary.

1.3 Optical Magnetism

Metamaterials are commonly fabricated using metals to construct the "meta-atoms", although recent studies have seen various nitrides be adopted as the constituent material [8,9]. All metamaterials investigated in this thesis utilise a metal in their construction. When an electromagnetic plane wave at optical wavelengths is incident upon a metamaterial, there is much greater coupling between the electric-field component of the light and the atoms of the

metamaterial structure than there is of the magnetic-field component. As a result the µ value of the constituent material (such as a metal) is close in magnitude to that of the free space value. This differs from the permittivity as the ε value of the constituent material is substantially different to that of ε in free space. Because of the differences in ε and µ values in constituent materials, the electric resonance is usually present at shorter wavelengths than the magnetic resonance.

To achieve a negative refractive index and thus negative refraction, both an electric and magnetic response are required from the metamaterial. While some metals exhibit a negative ε value at optical frequencies, the magnetic response must be separately engineered. Therefore metamaterials must be designed in such a way that they produce a magnetic resonance when subjected to an electromagnetic wave. This is commonly achieved by creating a metamaterial structure that behaves in a similar fashion to an equivalent inductive-capacitive model, or LC oscillatory circuit. Fishnets, split ring resonators (SRRs) and asymmetric split ring resonators (A-SRRs) are each different metamaterial structures that are examined in latter chapters of this thesis.
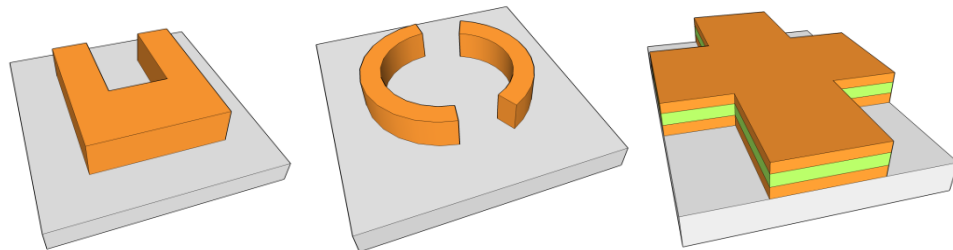
Figure 1.3: Single unit cell of a) a split ring resonator (SRR), b) an asymmetric-split ring resonator (A-SRR) and c) a single active layer fishnet. All three of the structures induce an inductance and capacitance when excited by an electromagnetic wave, creating a magnetic resonance.

All three of the structures shown in figure 1.3 have a separate inductive and capacitive component that, when excited by an incident electromagnetic wave, produce a magnetic field that opposes the magnetic field of the incident wave. This diamagnetic response can be explained by Lenz's Law, which states that the magnetic field of the induced current opposes the change in the applied field that produces it.

$$\varepsilon = -\frac{\delta \Phi_B}{\delta t} \qquad\qquad (1.19)$$

In equation 1.19, $\delta\Phi_B$ represents the change in magnetic flux. The negative sign of the magnetic flux indicates that it opposes the electric permittivity, ε. As a result the "LC oscillatory circuit" provides a magnetic resonance and can potentially produce a negative real part for μ, thus making a negative refractive index achievable.

1.4 Plasmons & surface plasmon polaritons

Metals each have an associated free electron gas that is caused by valence electrons being detached from the ions of the metal. Oscillations of these free electrons are called plasmons and occur at the plasma frequency, ω_p, which is determined by the metal type. The presence of an incident electromagnetic wave can excite the plasmons, which will resonate at the plasma frequency while energy is lost due to the associated damping of the metal. The plasma frequency can be expressed as follows,

$$\omega_p = \frac{n_e e^2}{m_{eff}\varepsilon_0} \hspace{4cm} (1.20)$$

with n_e defined as the electron density, e is the electron charge, m_{eff} is the effective mass of an electron and ε_0 is the dielectric constant in vacuum. As well as the presence of plasmons in the bulk of the metal, additional surface plasmons (SP) also exist and reside at interfaces between the metal and a dielectric. As with "ordinary" plasmons, an oscillation in surface plasmons can be induced by an incident electromagnetic field. The interaction of surface plasmons with an incident light wave (photon) produces, if the resonant frequency of both components is the same, a surface plasmon polariton (SPP). Surface plasmon polaritons propagate in a given direction along the interface of the metal depending on the polarisation of the incident wave. The polarisation determines the orientation of the orthogonal electric and magnetic field components of the incident wave.

The complex dielectric function defines the absorption properties of a metal and is expressed as:

$$\varepsilon = \varepsilon_1 + i\varepsilon_2 \hspace{4cm} (1.21)$$

In this complex function, ε is the dielectric constant and ε_1 and ε_2 are the real and imaginary components respectively. The Drude model, which describes the motion of electrons in a material, defines these components as [9]:

$$\varepsilon_1 = 1 - \frac{\omega_p^2}{\omega^2 + \gamma^2} \qquad\qquad (1.22)$$

$$\varepsilon_2 = \frac{\omega_p^2 \gamma}{\omega(\omega^2 + \gamma^2)} \qquad\qquad (1.23)$$

where ω is the frequency of the incident wave and γ is the collision frequency (also known as the damping constant).

For metallic shapes and particles that are sufficiently small in size, such as in the nanometre scale, an incident electromagnetic field can interact with the free electrons in the metal to create an oscillation. The movement of electrons on the metal nanoparticle produces an electric dipole response and a resultant resonance. The frequency of this plasmonic resonance is dictated by the plasma frequency of the metal and the physical dimensions of the particle.

1.5 Skin effect

The skin effect of a metal describes the distribution of the current flow in the conductor. The current density is found to be greatest near the surface of the metal and decreases as the depth from the surface increases. It can be a significant factor in the resistance of a metallic structure, particularly at high frequencies when the skin depth is reduced. The skin depth (δ) in a metal can be calculated using equation 1.24 [11].

$$\delta = \frac{1}{\sqrt{\pi f \mu_r \mu_0 \sigma}} \qquad\qquad (1.24)$$

The frequency is denoted by f, μ_r is the relative permeability of the metal (assumed to be 1), μ_0 is the permeability of free space and σ is the conductance.

The electric field strength below the surface of a metal decreases exponentially with depth and can be found from equation 1.25 [12].

$$|E(z)| = |E_0|e^{-z/\delta} \hspace{4cm} (1.25)$$

where E_0 is the electric field at the metal surface, z is the depth from the surface and δ is the skin depth of the metal.

1.6 Optical Sensing

There are many different methods in which a material can be characterised, or sensed, optically. Raman scattering, white light interferometry, Fourier transform spectroscopy and fluorescence spectroscopy are all optical platforms that enable the measurement of structures and devices [13]. However, the ability to sense a material very often depends on more than just the retrieval technique.

Plasmonic and metamaterial sensors [14] are one way of aiding the detection of analytes (a substance or chemical being studied) in a sample. Bragg grating and photonic crystal sensors are amongst many other types [15]. However irrespective of the type of sensor being characterised, certain concepts can be applied to gauge the effectiveness of the sensor in the detection of analytes [16]. The first of these concepts is the sensor's ability to detect an analyte and the minimum quantity of analyte that can be sensed. Generally, the smaller the quantity of analyte that is detected the more desirable the sensor as it demonstrates high sensitivity to the presence of small quantities. Similarly the sensor should be able to provide a good signal to noise ratio (SNR), irrespective of the amount of analyte present. Failure on this factor risks limiting the accuracy of the sensor and falsely "sensing" a spectral feature. If a sensor does not possess an adequate spectral resolution so that, for example, a narrowband or weak molecular feature cannot be detected then inaccurate results can also be produced. The optical sensor must also be precise and have a high level of repeatability, in that it can provide the same output with the same conditions applied for a suitable number of measurements or given time. Finally, it is useful for a sensor to be able to react in response to particular conditions of the analyte and not just as a binary sensing mechanism. These conditions could, depending on the analyte, include quantity, temperature and concentration. A sensor that can detect changes in these or other variables widens its potential application.

1.7 Aims and objectives

The principle objective of this thesis is to investigate the ability and functionality of certain optical sensors at near-infrared (and to a lesser extent visible) wavelengths. This includes the manufacture of sensors using techniques that enable them to be used in a commercial environment and not solely in a research environment. The aims include:

- Quick and inexpensive production of optical sensors and resonators over large surface areas, while maintaining a high quality of fabrication.

- Experimental study of optical sensitivity to particular analytes.

- Determination of areas of high sensitivity in split ring resonator sensors using experimental techniques to verify (or otherwise) simulated behaviour.

- Develop new and novel fabrication techniques using nanoimprint lithography to produce plasmonic and polymer sensors.

- Development of nanoimprint technique for the production of polymer waveguides and distributed Bragg reflectors (DBR) for optical biosensing.

1.8 Chapter conclusions

This chapter has introduced basic principles that contribute to the understanding of the research work detailed in this thesis. This includes an overview of electromagnetics, classical optics, plasmonics and optical sensing. Additional background information is included in subsequent chapters. The defining characteristics of metamaterials are discussed as well as concepts that determine their behaviour, such as the plasma frequency of a metal and the skin effect. Desirable properties of optical sensors are also given and the aims and objectives of this thesis are stated.

Chapter 2

Fabrication and measurement
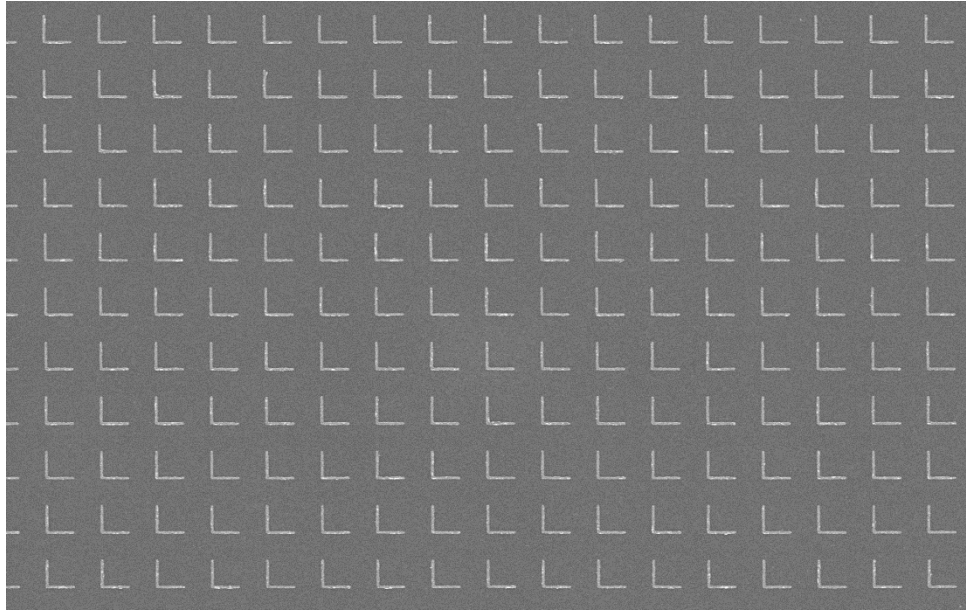
2.1 Introduction

With fabrication and characterisation forming a significant proportion of the work reported in this thesis, this chapter will explain much of the background information regarding the lithography techniques and measurement arrangements used. A detailed description of the specific fabrication process used in producing each of the structures studied is contained in the respective chapters. Likewise measurement techniques used in characterising each structure is also included in each relevant chapter. However this section will explain many of the fundamental principles for the fabrication and characterisation procedures used.

Two nanofabrication techniques are employed to pattern the structures studied throughout this thesis: electron-beam lithography (EBL) and nanoimprint lithography (NIL). There are numerous advantages and disadvantages associated with both techniques and these too will be discussed.

2.2 Electron-beam lithography

Electron-beam lithography, or e-beam lithography, is a patterning technique that involves scanning a beam of electrons onto an electron sensitive polymer called an e-beam resist. The direction and movement of this electron beam is determined by a complicated arrangement of lenses, beam deflectors and apertures that both focus the beam onto the e-beam resist and control its motion. The e-beam resist is patterned by its exposure to the electron beam, replicating a design input electronically. The University of Glasgow primarily uses a Vistec Vector Beam 6 ultra-high resolution, extra-wide field (UHR-EWF) electron-beam lithography tool, housed in the James Watt Nanofabrication Centre (JWNC). All samples in this thesis patterned using EBL were exposed using this tool.

EBL is particularly desirable in the fabrication of structures with very small feature sizes (<100 nm). The Vistec VB6 tool has the capability of producing an electron-beam with a 4 nm wide spot size and minimum resolution of 0.5 nm at either 50 or 100 kV. This is a particular advantage when fabricating metamaterials with features smaller than the wavelength of incident light.

There are a number of factors that determine the quality of a pattern exposed in e-beam resist. The electron-beam spot size, exposure dose and beam step size (BSS) are all variable parameters from the EBL tool that have a profound effect on the quality of the exposure. Reduced beam spot sizes (such as 4 nm) are almost certainly required to pattern small features while the exposure dose (measured in $\mu C/cm^2$) determines the charge applied by electrons and the extent of area of resist that they expose. The beam step size is a measure of the period (physical distance) between each exposure of electrons. If this period is too small in value the pattern can be "over-exposed" while too large a period can see the resist "under-exposed". In both cases quality will be reduced and the pattern may not resemble the desired design.

Consideration must also be given to the e-beam resist and the consequences this has on the exposure. In all cases regarding the work discussed in this thesis, resists were spin coated onto a substrate. As well as the type of resist used, the spin-speed, acceleration and spin duration are all factors in determining the final thickness of the resist film. Resists can also be diluted with a solvent to acquire a reduced thickness. Thinner resist films are commonly utilised when very small features are required to be patterned. Reduced spin speeds, or highly viscous resists can result in the presence of a non-uniform film, typified by "beads" (an increased thickness) at the edge of the substrate. For this reason the physical dimensions of the substrate may also be a consideration in achieving a desirable resist film.

2.2.1 Electron-beam resists

E-beam resists can generally be categorised into one of two groups: negative tone and positive tone. Areas of negative tone resist that are exposed to electrons remain present after being chemically developed while areas of resist not exposed are removed, leaving the written pattern in the resist. Conversely positive tone resists are chemically weakened when exposed and therefore removed when developed, with non-exposed regions remaining. This concept is shown in figure 2.1.
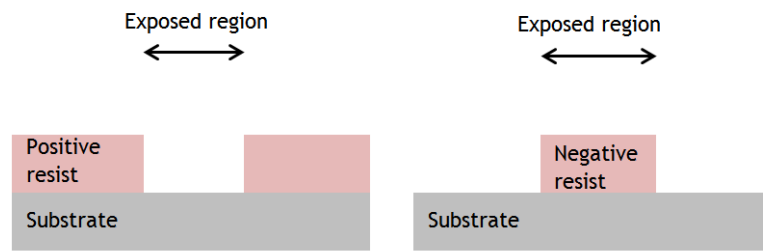
Figure 2.1: Ideal positive and negative resist profiles following exposure and development.

When a positive tone resist is exposed to an electron beam the polymer bonds are broken (polymer chain scission) and made susceptible to removal by chemical developer. With a negative tone resist the effect is opposite. Energy from the electrons cross-links polymer chains making them resilient against a developer.

Two e-beam resists are used in the entirety of this thesis: Polymethyl methacrylate (PMMA) and Hydrogen silsesquioxane (HSQ). PMMA is used as a positive tone e-beam resist and HSQ is used as a negative resist. PMMA is, amongst other things, used to pattern substrates that are subjected to metallisation and a process termed "lift-off". This involves clearing areas of the PMMA resist by way of exposure and development and then depositing a layer (or layers) of metal. Metal deposited within the areas removed of resist adhere to the substrate while the remainder of the metal sits on top of the PMMA. Placing the sample in warm acetone removes the PMMA from the substrate as well as the metal on top of it, leaving metal structures in the exposed regions. This is shown in figure 2.2. With this "lift-off" fabrication technique it is desirable, if not necessary, to have a non-vertical, undercut PMMA sidewall profile before metal is deposited. This ensures that as metal is deposited, such as by way of evaporation, it does not adhere to the PMMA sidewalls of the pattern. This enables acetone to infiltrate the resist and remove unwanted metal. An undercut in the PMMA sidewall is achieved by spin-coating a bilayer of PMMA with two different molecular weights. By spinning PMMA with a low molecular weight onto the substrate, baking it so that it hardens, then spinning PMMA with a higher molecular weight on top, an undercut can be produced following exposure and development. This is caused by the low molecular weight PMMA being more susceptible to polymer chain scission than the PMMA with a higher molecular weight. With more of the bottom layer of PMMA removed than from the top layer, an overhang creates an undercut profile while acting as a mask for deposited metal.
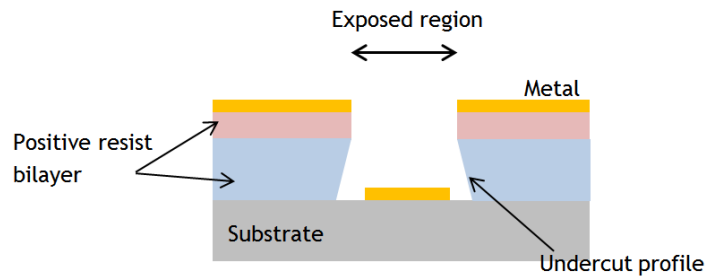
Figure 2.2: Undercut profile of a developed PMMA bilayer. The undercut in the bottom layer of resist allows metal to be deposited without it adhering to the resist sidewall.

As a negative tone resist, HSQ is commonly used for different fabrication processes than PMMA. The nature of the pattern being written and its fill factor (ratio of written areas to un-written areas of resist) often determine which electron-beam resist is most suitable. HSQ exhibits a higher dry-etch selectivity ratio to PMMA, meaning that it is more resilient to etch processes and acts as a better etch mask [17].

2.2.2 Proximity effect

The behaviour of electrons in the electron-beam changes significantly when they interact with the e-beam resist. Electrons can be applied with an accelerating voltage up to 100 Kv when fired from the electron-gun of the lithography tool. When these high energy electrons strike an electron-sensitive polymer in a low-pressure chamber under vacuum, their trajectory and velocity change rapidly. Furthermore, their mean free path in the polymer exceeds the thickness of the resist on top of the substrate. Upon incidence with the resist, electrons can suffer from forward scattering [18,19]. This inelastic collision involves electrons from the beam colliding with electrons already present in the resist, thus transferring energy to them. These secondary electrons can then propagate in differing directions through the resist and expose a larger area than where the beam was incident, creating a pear-shaped distribution in the resist [18]. Electrons that penetrate the depth of the resist and interact with the substrate undergo an elastic collision. In this instance the negatively charged electrons collide with positively charged nuclei, causing the electrons to scatter in a broad range of directions. This unwanted extra exposure from the backscattered electrons is termed the proximity effect, in that it is determined by the density of electron-beam exposure over a given area. The behaviour of forward scattered and backscattered electrons in e-beam resist on a substrate is shown in figure 2.3.
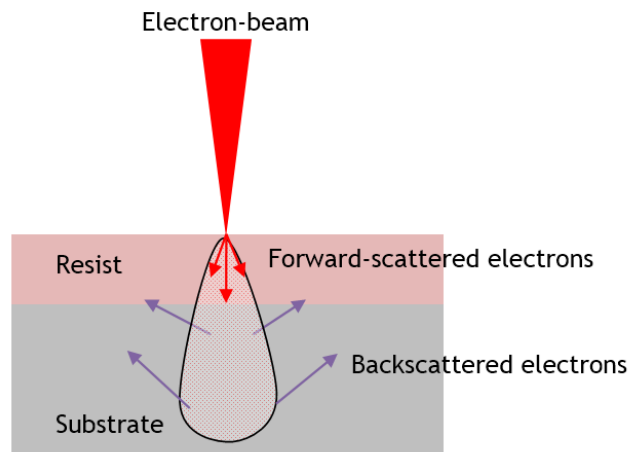
Figure 2.3: Diagram showing the presence of forward scattered electrons and backscattered electrons in the resist and substrate.

With forward scattered and backscattered electrons exposing an enlarged area of resist, the patterns produced may differ from the original design. This is particularly the case for small features or for structures requiring exposures with a very short periodicity. For example if 10% of a given area of resist is exposed using an electron-beam, the presence of forward scattered electrons and backscattered electrons will be less than if 50% of the area is exposed. The shape of the pattern being written can also effect the concentration of and distribution of forward scattered and backscattered electrons.

The negative consequences of the proximity effect, namely overexposure, a reduction in the resolution and an increase in the pattern size, can be limited using proximity correction software. This software fractures the pattern design into a range of component shapes and varies the exposure dose applied to each depending on the geometry of the shape and surrounding exposure density. Optimisation of the electron-beam parameters (such as dose, beam spot size and accelerating voltage) and the electron-beam resist (such as thickness and dilution, if any) can also help reduce defects caused by the proximity effect.

2.3 Nano-imprint lithography

In comparison to EBL, nano-imprint lithography (NIL) uses a stamp to make physical contact with the sample being patterned in order to define the desired design [20,21]. The sample being patterned by the stamp will be referred to as the "target sample" throughout this thesis. Whereas EBL uses software to control a series of magnets and lenses that determine the exposure pattern, NIL uses a

stamp with a three dimensional profile of the desired pattern. NIL stamps can be made using a variety of materials, with silicon and fused silica being common [22,23]. A diagram showing the nanoimprint lithography process is shown in figure 2.4. The non-uniform surface of the stamp means that when it is pressed into a resist or polymer on the target sample, an impression of the stamp is made. After separating the stamp from the target sample the imprinted pattern can be used for the purposes of metallisation or etching in the same way as used for samples patterned by EBL. As the patterned polymer is physically displaced during imprinting, unlike EBL no chemical development of the polymer is required. However, compression of areas of polymer in contact with the stamp leave a residual layer that must be removed if metal is required to be deposited onto the substrate. This residual layer can be removed by etching the polymer before depositing metal. In most scenarios the stamp can be re-used after imprinting to pattern other samples.
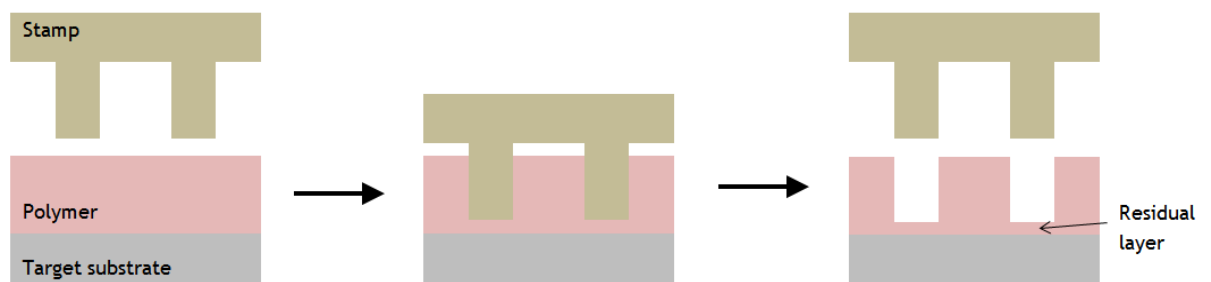
Figure 2.4: Diagram showing a typical nanoimprint lithography process.

The imprinting process can commonly be categorised into one of two types: thermal imprinting or ultra-violet (UV) imprinting. With thermal imprinting, heat is applied to the stamp, target sample or both in order to improve the flow of the polymer so that it can fully infiltrate the deeper or narrower regions of the stamp. Ultraviolet aided imprinting uses a UV curable polymer that is exposed to UV light during imprinting to achieve the same effect. Under this latter technique, either the stamp or target sample must by transparent in order for UV light to expose the polymer.

There are a number of considerations to be made in relation to nano-imprinting. The viscosity of the polymer used can limit the imprint depth of the stamp and hamper its filtration into small features of the stamp, resulting in a degradation in the quality of the imprinted structure. The imprint force applied to the stamp

is also an important parameter in NIL. Imprinting into highly viscous polymers or strong materials is likely to require a higher imprint force than if a low viscosity material is used. This requires the substrates of the stamp and target sample to be suitably strong, either by selecting an adequate material or increasing the substrate thickness to reduce the likelihood of it breaking.

For the work contained in this thesis, two nanoimprinting tools were used. For the fabrication of structures using thermal NIL an Obducat Nanoimprinter was used and is shown in figure 2.5. In work where the required imprint pressure was greater than the capability of the Obducat tool (30 bar), a Specac hydraulic press with a maximum imprint force of 15 Tons was utilised. This latter scenario covers fabrication contained in chapter 5.
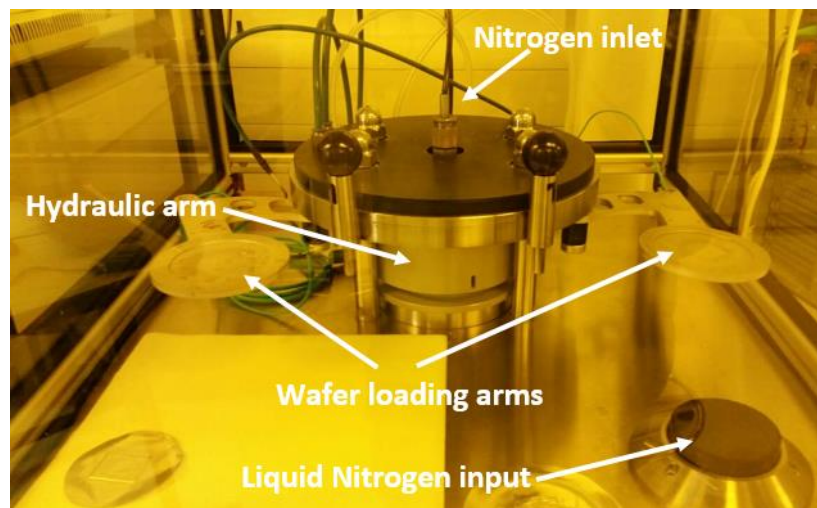
Figure 2.5: Picture of an Obducat Nanoimprinter used for thermal imprinting. The key component parts of the tool are indicated.

In order to pattern using the Obducat Nanoimprinter, shown above, both the stamp and target substrate are placed on a single loading arm, which is then moved into position above a hydraulic arm. The hydraulic arm is raised to secure the loading arm into place beneath a flexible imprinting plate. Nitrogen gas is then pumped into a chamber above the imprinting plate, pushing it down onto the stamp and thus imprinting onto the target substrate. The imprint force can be varied by changing the pressure of the nitrogen gas. A heating filament is contained within the wafer loading arms and a thermocouple enables control of their temperature.

2.4 Comparison of lithographies

There are of course advantages and disadvantages to both electron beam and nano-imprint lithography and these usually determine their application in both research and commercial environments. A comparison of EBL and NIL is made in table 2.1.

Lithography	Advantage	Disadvantage
Electron-beam	Software controlled exposure of patterns meaning versatility in pattern design.	Exposure process is slow and not suited to commercial environments. Pattern area is limited in size.
	High resolution structures with minimum feature sizes <10 nm.	Equipment and operation is costly.
Nano-imprint	Lithography process is much cheaper than EBL and suited to commercial applications, such as roll-to-roll NIL.	Etching of residual polymer layer is required for deposition of materials onto substrate.
	Sub 10 nm features can be obtained. Large areas can be patterned quickly and stamps can be re-used.	Production of stamps can be expensive and time consuming. New patterns require new stamps to be produced.

Table 2.1: A comparison of the advantages and drawbacks of electron-beam and nano-imprint lithography.

While EBL may be beneficial in a research environment, where fabrication is often performed on cleaved substrates rather than complete wafers or other substrates of equivalent size, it is not viable in the mass production of nanotechnologies. Patterning using EBL is slow and time consuming, particularly for small, intricate shapes, and the patterning time is proportional to the area being written. Nanoimprint lithography however enables large areas to be patterned simultaneously and quickly at a comparatively low cost. Although fabrication of nano-imprint stamps typically requires EBL and etching processes, the stamps can often be re-used, either on different target samples or sequentially on the same sample. This latter example is termed "step-and-repeat" nano-imprinting and is a technique that enables the patterning of large areas without the need for large, expensive stamps. Where mass production of a patterned material or substrate is required, roll-to-roll imprinting can be used [24]. This method involves feeding a substrate through a rotating cylindrical feed that has the pattern required to be imprinted on its surface. Although fast and inexpensive, this technique is not

suitable for all fabrication processes, particularly where, for example, critical alignment between layers is required.

For metamaterials and optical sensors to realistically be used in a commercial setting, a move away from electron-beam lithography as a patterning technique must be made. Much of the work detailed in subsequent chapters attempts to show that nanoimprint lithography can be a viable alternative to EBL, not just for commercial practices but also in terms of research and development.

2.5 Dry etching

In order to create the three dimensional profile required of nano-imprint stamps and to remove the residual polymer layer present following imprinting, dry etch processes are required. Dry etching is the removal of specific materials on a sample through use of various gases. This differs from wet etching which etches substances by immersing them in liquid chemicals. Dry etch techniques use plasmas containing certain gasses that react with a sample material and remove them from the wafer or thin film. The reactive gases used are dependent on the material being etched. Silicon etches for example typically use a sulphur hexafluoride and oxygen (SF_6/O_2) plasma. Certain parameters used in the creation of the plasma-gas mixture, such as the tool chamber pressure, bias voltage and gas flow rate, can be altered to increase or decrease the etch rate of the material. More aggressive etches, such as those that are characterised by a high gas flow rate or high bias voltage, can be useful in etching materials at a faster rate. This is often utilised when a deep etch, typically removing many microns of a material, is required.

There are a variety of dry etch processing techniques, including reactive ion etching (RIE) etching and inductively coupled plasma (ICP) etching. Both RIE and ICP processes utilise reactive gasses in plasma to etch selective materials. An alternative method to RIE and ICP dry etching is focused ion beam (FIB) milling of a material. FIB etches use a focused beam of ions operated at high currents to bombard the sample material and sputter atoms from the substrate, essentially scribing an etch pattern. In RIE systems, a diagram of which is shown in figure 2.5, reactive gasses are pumped into a chamber containing two electrodes, one at the top and the other at the bottom. A strong radio frequency (RF) electromagnetic

field is applied via the two electrodes and thereby accelerating the electrons in the gas in a unilateral direction. This ionizes the gas molecules and creates plasma. The free electrons can be removed through a grounding plate, such as the chamber wall. With negatively charged electrons removed from the plasma there now exists a greater concentration of positive ions. The plasma contains ions, such as fluorine or chlorine ions – depending on the reactive gas input. While the electrons in the chamber move at great speed, the much heavier ions drift towards the negatively charged bottom electrode. It is on this electrode that the wafers being etched are placed. When they collide with the wafer the ions react chemically with the material as well as physically removing atoms due to bombardment. This latter occurrence increases in frequency as the kinetic energy of the ions is increased. Free radical atoms present in the plasma also contribute to the etching of the wafer. As a result of the applied electromagnetic field, the ions move in a linearly downward direction. This can produce anisotropic sidewall profiles that do not exhibit the undercut or angled sidewalls seen as a result of wet chemical etching.
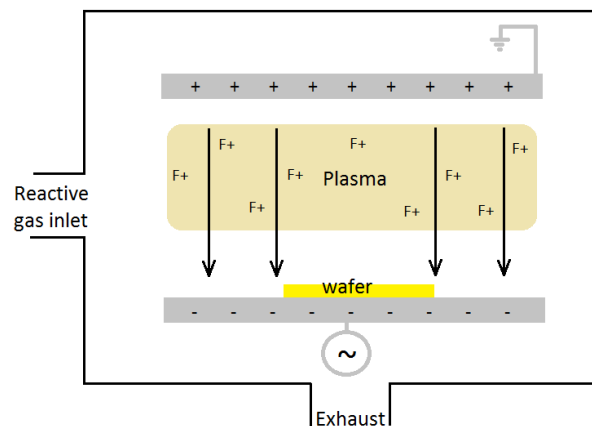
Figure 2.6: A schematic showing the operation of a RIE system in which ions are directed laterally towards a wafer by an applied electromagnetic field.

In order to etch selective regions of a sample rather than its entirety, a mask must be present to shield areas not to be removed. This mask must be made from a material that is more resilient to the etch gas than the substrate.

2.6 Experimental measurement techniques

As with fabrication techniques, specific measurement details and procedures are stated in the relevant chapters. This section will describe in detail the two

spectroscopy techniques most frequently used in the bulk of the work contained in this thesis. These are Fourier transform infrared spectroscopy (FTIR) and monochromator scanning spectroscopy. Both of these spectroscopy techniques can be used to obtain reflection and transmission spectra from a specimen. However the method used to produce and detect each spectrum differs.

2.6.1 Fourier transform infrared spectroscopy

Fourier transform infrared spectroscopy is a technique that can be used to measure a sample's ability to absorb light over a wide range of frequencies. A broadband light source produces the light frequency spectrum to be measured. This light is collimated and shone upon a beamsplitter, which splits the light into two rays and directs both rays to two different mirrors. This forms an arrangement known as a Michelson interferometer. Of these two mirrors one is stationary and has a constant path length from the beamsplitter while the other is movable in the plane perpendicular to its reflective surface, altering the path length. The difference between the optical path length for the stationary mirror and the movable mirror is called the retardation. Varying the retardation changes the wave interference at the point where both beams recombine at the beamsplitter. The beams are both partially transmitted and partially reflected, with one beam returning towards the light source while the other is incident upon the sample being measured and the detector. Changes in intensity in the output beam, due to constructive and destructive interference, are a function of the optical path difference. For example displacement of the moveable mirror by a distance of $\lambda/4$ changes the optical path length by $\lambda/2$. This results in the two beams being $180°$ out of phase when they recombine and produces destructive interference. A plot of the intensity measured by the detector is known as an interferogram. This interferogram is processed by applying a Fourier transform function to produce a reflection or transmission spectrum with respect to frequency.
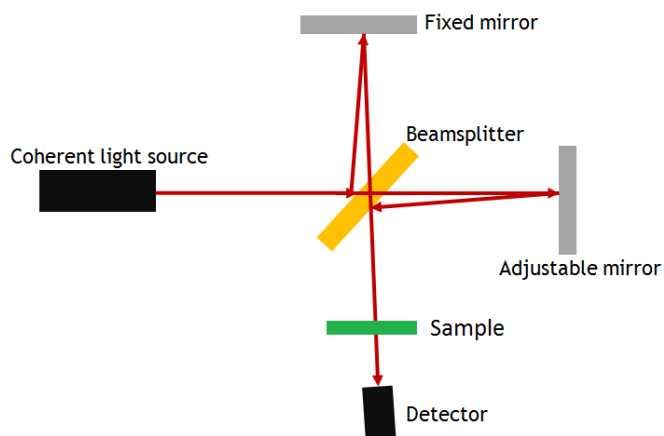
Figure 2.7: A diagram of a Michelson interferometer for use in FTIR spectroscopy.

The results from all FTIR measurements reported in the following chapters were performed on a Bruker Vertex FTIR with a Hyperion microscope attached. A mercury-cadmium-telluride (HgCdTe, MCT) direct bandgap photo-detector was integrated within the microscope and used to obtain transmission and reflection spectra. Liquid nitrogen is used to cool the detector and keep it at an operational temperature. For near infra-red measurements, classed as between 900 nm and 5000 nm, a calcium-fluoride ($CaF_{2)}$ beamsplitter was used. Measurements that extended into mid-infrared wavelengths (range 1.25 µm to 16 µm) used a potassium-bromide (KBr) beamspitter. A series of software controlled mirrors were used to change the beam path of the light. Transmission measurements passed light through the sample from its underside to the MCT detector located above the top surface. Reflection measurement shone light onto the top surface of the sample and measured the light reflected back. In both reflection and transmission measurements light was incident on the sample at normal incidence. For experiments requiring TE and TM modes to be produced separately, a zinc-selenide (ZnSe) polariser was placed in the beam path directly in front of (before) the sample.

In order to acquire a reflection or transmission spectrum from a sample a background spectrum must first be taken. Depending on the sample being characterised what quantifies the background may differ. With respect to the FTIR results contained in this thesis, a sheet of un-patterned metal (gold or silver) was used as a background for reflection measurements involving metallic structures on a substrate. For a background spectrum for transmission measurements the light was passed through the transparent substrate and measured. Following

measurement of the background, the sample spectrum is obtained. In this instance the fabricated pattern is measured using the same reflection and transmission arrangement as described for the background. The final reflection or transmission spectrum is a ratio of the sample spectrum and the background spectrum. It is imperative that the polarisation and area being measured are identical for measurement of both the background and sample. Changes to either can result in the production of an inaccurate spectrum. For example, if a planar sheet of gold is measured as a reflection background and is twice the area of the measured metal structure array on the sample, the amount of reflected light will be disproportionately high in the background spectrum. In this circumstance the intensity of any features from the sample would be reduced in amplitude from their true value. Atmospheric features such as H_2O and CO_2 will also be more accurately displayed if the background spectrum and sample spectrum are measured under the same atmospheric conditions.

There are numerous advantages to FTIR spectroscopy that make it an attractive option in the optical measurement of devices and structures. As data from the entire spectral range (within the capabilities of the light source and detector) is measured simultaneously, spectra can be obtained quickly. This is unlike monochromator scanning spectroscopy. A short measurement time has particular appeal with regard to sensing applications in industry or, for example, front-line medical care. Secondly, simultaneous measurement of a spectrum provides an improved signal to noise ratio (SNR) compared to dispersive measurement techniques. This is because of the Fellgett advantage, which specifies that systems in which noise is primarily attributed to that of the detector can yield an improvement in the SNR if the measured signal is multiplexed rather than obtained sequentially [25]. As there is no dispersive element to an FTIR system, such as gratings and optical slits, there is little restriction in the amount of light that is incident upon the measured sample. This is known as Jacquinot's advantage. The slits and gratings present in a monochromator scanning system attenuate the infrared light used for measurement. One of FTIR spectroscopy's greatest advantages however is its resolution capability. Spectral resolutions of 4cm-1 are typical, with higher resolutions also available. For a dispersive monochromator to achieve the same resolution, the entrance and exit slits would need to be extremely narrow.

Conversely, there are a number of considerations that should be made with regard to the limitations of FTIR spectroscopy. FTIR systems produce an interferogram to which a Fourier transform function is applied to create a spectrum. They do not directly measure spectra. By obtaining an interferogram of the light source (background measurement) followed by an interferogram of light transmitted through or reflected off of a sample, an absorption spectra as a function of wavenumber can be produced by conversion using a fast Fourier transform (FFT) algorithm. Therefore the accuracy of the spectrum produced is significantly dependant on the Fourier transform. Secondly, as a spectrum is obtained simultaneously noise (such as source noise, shot noise) is applied across the entire wavelength range, rather than being confined to a single wavelength as would be the case in a dispersive system. However, it should be noted that detector noise limiting features can be applied to negate this problem.

2.6.2 Monochromator scanning spectroscopy

Unlike an FTIR system, a monochromator based scanning spectrometer obtains the reflection or transmission from a sample by increasing the wavelength of the incident light sequentially and measuring the response. Measuring using this technique requires a different a different set of equipment and arrangement to that of FTIR spectroscopy. Primarily, a monochromator is needed to produce a single wavelength of light from an input broadband light source. A common monochromator arrangement, and the one used for experimental work contained in this thesis, is the Czerny–Turner setup. For work at visible and near-infrared frequencies, a tungsten white light lamp was used as the broadband light source. In the Czerny–Turner arrangement, the broadband light is input to the monochromator through a narrow entrance slit. This slit is placed at the focal point of a concaved mirror positioned opposite, which acts as a collimator. The collimated light, in which the rays are ideally parallel and do not disperse with distance, is directed towards a series of gratings that can be rotated by computer control. The grating diffracts the collimated light, with the diffraction dependant on the angle of the gratings with respect to the collimator. The diffracted light is then directed to a second mirror which refocuses it at an exit slit. At this exit slit, the spectral range of the dispersed light is incident upon the plates that define the slit. However only light of a given wavelength (determined by the grating pitch and their angle relative to the beam-path) will pass through the slit and be output.

The width of the slits (gap) determines the wavelength range of output light, i.e. the spectral resolution.

As the gratings in the monochromator are slowly rotated, the wavelength of light that passes through the exit slit changes. Therefore, with the proper computer control, a spectrum of light can be produced over a period of time by the monochromator. For the purposes of measurement, light output from the monochromator is passed through an optical chopper, a device that periodically interrupts the light beam through use of a rotating wheel. The chopper interrupts the light at a fixed rate depending on the rotation speed of the wheel and the periodicity of the slots on it. It is directly connected to a lock-in amplifier, which also receives the output signal from the photodetector. This experimental setup is shown in a diagram contained in figure 2.7. A microscope is used to focus the modulated light from the optical chopper onto the sample being characterised before being detected by the photodectector. All visible range measurements used a silicon photodiode with a wavelength detection range of 400 nm to 1000 nm.
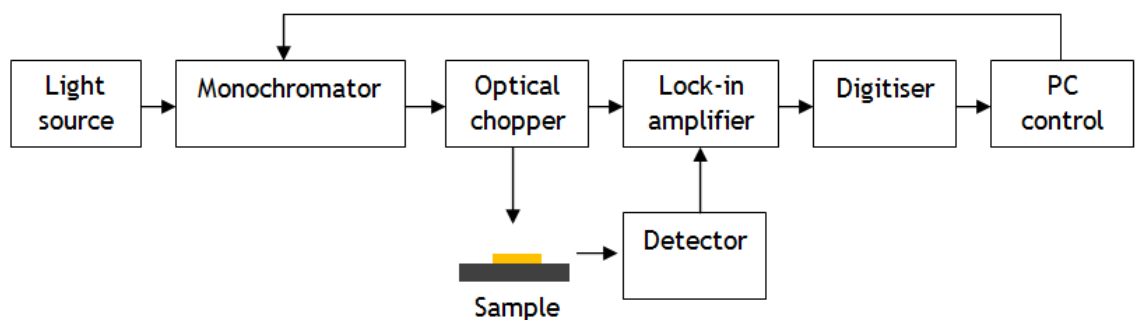
Figure 2.8: Diagram of the experimental setup used for measuring samples with under a scanning monochromator and lock-in amplifier configuration.

The frequency at which the light is modulated by the optical chopper is used as a reference signal by the lock-in amplifier. With this signal as an input, the lock-in amplifier can amplify solely parts of the signal from the photodiode that are modulated at the same frequency, i.e. light that has passed through the optical chopper. In doing so background noise can be substantially reduced and the signal to noise ratio significantly improved. This amplified signal is then processed by a digitiser and input to a controlling computer which, using software, can plot the light intensity against the wavelength of incident light (based on the position of the gratings in the monochromator).

Unlike FTIR spectroscopy, the monochromator scanning method directly measures a reflection or transmission spectrum from a sample and does not apply a mathematical transform function to it. The spectral range of measurement can be varied by changing the pitch of the gratings within the monochromator, provided that the light source produces a sufficiently broad wavelength spectrum. The photodiode detector must also be compatible with the spectral range output from the monochromator, with a number of materials with suitable bandgaps available for this purpose. Despite these advantages, a significant drawback to this spectroscopy technique is the increased time required to measure a sample, making it unattractive for industrial and front-end applications.

2.7 Finite-difference time-domain modelling

All simulations regarding work reported in this thesis utilised Lumerical FDTD (Finite-difference time-domain) Solutions software to model the fabricated structures. FDTD modelling is a grid-based numerical technique that employs Maxwell's equations, which are dependant to time and in partial differential form, to simulate the behaviour of a structure over a given frequency range. Rather than applying Maxwell's equations continuously across the model to be simulated, they are applied discretely using space and time partial derivative approximations. This creates multiple finite-difference equations that can be solved in turn to give the electric field and magnetic field components for a volume of space within the simulation grid. When repeated and the finite-difference equations throughout the entire simulation grid have been solved, the results can be complied to show the calculated electromagnetic field behaviour across the entire structure over a range of wavelengths.

In order for the discrete approximations of Maxwell's equations to be solved the material properties of each component part of the model must be specified. This can be achieved in one of two ways. Either the permittivity and permeability of each material can be input or a modelling function can be applied to approximate the electromagnetic behaviour. As FDTD simulations are performed over a range of frequencies, it is essential that the permeability and permittivity (and therefore refractive index) values for each material are wavelength dependant in order to give accurate and reliable results. Mathematical models, such as Lorentz, Drude and Debye, can be applied to a material in order to approximate its dispersive

behaviour in the absence of raw material data. In these instances alternative material data, such as the plasma frequency and damping (collision) frequency, may be used to help provide an approximation [26]. Throughout the simulations performed in the subsequent chapters, in which an array of periodic structures are illuminated, a plane wave light source was used. FDTD modelling does however allow for alternative sources to be used if required, including a single point light source or an applied electrical field.

Using the FDTD method to model structures has a number of advantages. As a broad range of frequencies are applied to the model and simulated simultaneously, FDTD is particularly useful in modelling structures that exhibit a broadband response. Furthermore, if the resonant frequency of a structure is unknown, the FDTD method can be used to simulate all feasible frequencies to efficiently find the resonance. This can save a significant amount of time if a model is simulated in advance of any fabrication work, as in most circumstances the simulation process can be completed in a shorter time than the fabrication. As the structure is simulated using a simulation grid of physical space, the electromagnetic response at a given point of the structure can be obtained. Refinement of the simulation grid, i.e. increasing the resolution of the model, can result in the behaviour of smaller features being more accurately portrayed. The fact that the simulation is performed in the time domain means that the electromagnetic behaviour of a structure (or specific parts of a structure) can be displayed my means of an animation. This is not only a useful visual representation of the model, but can help verify that the simulation is operating as expected.

2.8 Chapter Summary

This chapter provides background information relating to the fabrication and measurement techniques used in the work covered. Many of the concepts discussed, such as the proximity effect and the fundamental principles of FTIR spectroscopy, are important in understanding the limitations in fabricating metamaterials with very small features (particularly below 100 nm) and the means in which experimental results are obtained, respectively. Similarly an overview of the FDTD modelling technique provides reasons as to why this method is used in simulating the metamaterials and optical sensors. The strengths and weaknesses of electron-beam and nanoimprint lithographies are also compared. This presents

important basis for much of the work described in subsequent chapters, namely a requirement for metamaterials and other optical sensors to be produced cheaply and efficiently if they are to be used outside of a research environment.

Chapter 3

High resolution small-scale split ring resonators fabricated by nanoimprint lithography
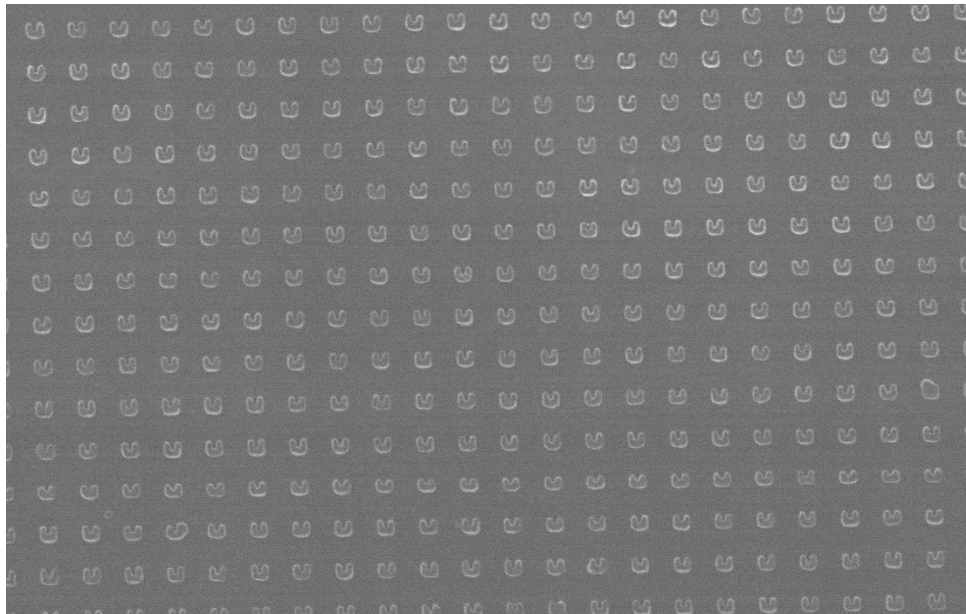
Abstract

Split ring resonators (SRRs) were amongst the first metamaterial structures to be intensely studied and they continue to be researched still. They can take a variety of forms but commonly resemble a "rectangular U" shape and are fabricated using either gold or aluminium. Reducing the size of an SRR increases the resonant frequency of the structure up until the point of saturation, at which the resonance will no longer shift irrespective of the SRR dimensions.

The principle aim of the work in this chapter was to fabricate SRRs that would experimentally demonstrate the resonance shift saturation for very small-scale, structures (sub 100 nm) with high quality features. This would be performed using a novel nanoimprint lithography technique rather than conventional electron-beam lithography. The benefits and disadvantages of this NIL method would be assessed by comparing with small-scale SRRs fabricated by EBL.

3. 1 Introduction

3.2.1 The split ring resonator

Since their inception [27,28] and initial investigation into producing negative refractive indices [29-31], the split ring resonator has been one of the most widely investigated metamaterial structures. As intimated in the previous chapter their shape, a variation of a "rectangular U" or "circular C" (as shown in figure 3.1) geometry, enables them to exhibit an electromagnetic effects that are not seen in naturally occurring materials. When light is incident on the SRR, the electrons present in the metal of the structure oscillate, creating an electromagnetic response. This response can be altered by changing the size and shape of the SRR. The arms of the SRR create a physical gap that introduces a capacitive element to the structure while the wire that connects both arms can be considered as acting like a single coil inductor. This enables the SRR to be thought of as an LC equivalent circuit.
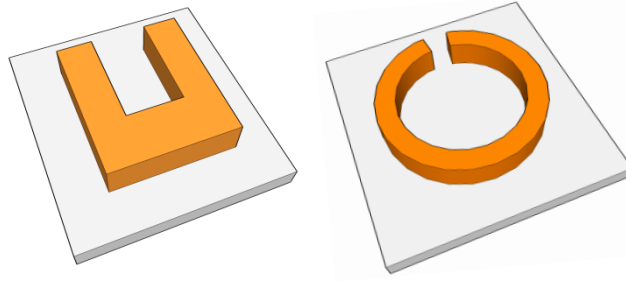
Figure 3.1: Diagrams of two split ring resonator shapes. Both the "U-shaped" (a) and "C-shaped" (b) SRRs have an intrinsic capacitance and inductance.

When the electric field component of an incident electromagnetic wave spans across the gap of the SRR, it couples with the capacitance and creates a current that flows around the structure. This current generates a magnetic field in the metallic structure and creates an electromagnetic, LC resonance [32] that interacts with the incident electromagnetic wave. This LC resonance can be written as:

$$\omega_0 = \frac{1}{\sqrt{LC}} \tag{3.1}$$

For a "U-shaped" SRR, Tretyakov adds additional terms to this equation [33].

$$\omega_0 = \frac{1}{\sqrt{(L + L_{add})(C + C_{add})}} \tag{3.2}$$

where

$$L_{add} = \frac{l_{eff}}{\varepsilon_0 w h \omega_p^2} \tag{3.3}$$

where l_{eff} is the effective conductor length, ε_0 is the permittivity of free space, w is the SRR width, h is the height and ω_p is the plasma frequency of the metal. The effective conductor (or ring) length, is approximated as $l_{eff} = (\pi/2)l$, where l is the total physical length of the metal. The additional capacitance, C_{add}, is given by:

$$C_{add} = \frac{\varepsilon_0 \varepsilon_r w h}{l_{eff}} \tag{3.4}$$

where ε_r is the relative permittivity. The L and C components are approximated using the round loop inductance and parallel-plate capacitance respectively:

$$L \approx \mu_0 \frac{l^2}{h} \tag{3.5}$$

$$C \approx \varepsilon_0 \varepsilon_c \frac{wh}{\delta} \tag{3.6}$$

Where ε_c is the dielectric constant of the substrate and the gap width is denoted by δ.
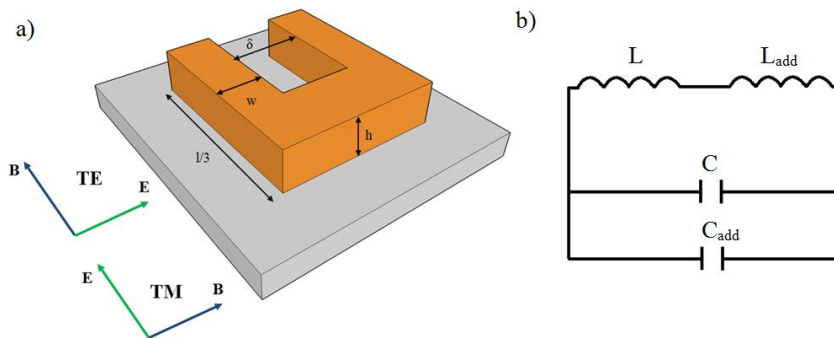
Figure 3.2: a) An annotated diagram of an SRR, showing the arm width (w), gap (δ), structure height (h) and effective conductor length (l). In this example each of the three wires that create the "U shaped" SRR is of length 1/3, as l/3 equals 2w+ δ. The orientation of the magnetic (B) and electric (E) fields are shown for both transverse electric (TE) and transverse magnetic (TM) mode. b) An equivalent circuit of the SRR.

As shown in figure 3.2, the orientation of the electric (E) and magnetic (B) fields of the incident electromagnetic wave are significant with regard to the response of the SRR. For the SRR structures discussed in this chapter, under transverse electric (TE) mode the electric field component couples with the capacitance of the SRR gap, creating a circulating current and resultant magnetic response from the inductive "wire" of the structure. In transverse magnetic (TM) mode, the electric field cannot couple to the SRR gap, preventing current from circulating around the structure and generating a magnetic response. Under this condition, the only response is a plasmon resonance, created by the incident wave exciting plasmons in the constituent metal of the SRR. This plasmon resonance is also observed under TE conditions. As will be discussed in subsequent chapters, the definition of TE and TM modes is dependent on the geometry of the metamaterial.

3.1.2 - Shifting the LC resonance to shorter wavelengths

There has been a significant effort to shift the resonance of metamaterials to ever shorter wavelengths, particularly into the visible range [34-36]. This is in part because no naturally occurring materials offer magnetic properties as these high frequencies. The LC resonance has been shown to be dependent on the physical dimensions of the SRR, with the capacitance and inductance proportional to the size of the structure. Therefore the LC resonant wavelength can be deemed to shift proportionally with the size of the SRR. However scaling the dimensions of an SRR to shift the LC resonance to shorter wavelengths can only remain relevant while the constituent metal behaves as such. As shown in equation 3.3 the plasma frequency of a metal becomes an increasingly dominant component as the dimensions of an SRR get ever smaller. At high frequencies (short wavelengths) such as at the visible regime, the kinetic energy of the electrons in the metal reduces the ability to generate a current loop in the SRR [37], thus hampering the magnetic response. For this reason the resonant wavelength will reach a limit at which scaling the SRR to smaller dimensions will fail to shift it to shorter wavelengths. Constructing a split ring using a metal that possesses higher plasma frequency can help push the LC resonance towards or into the visible range. Gold for example has a plasma frequency, ω_p, of 2175 THz whereas aluminium exhibits $\omega_p = 3750$ THz. Fabricating an SRR using Al rather than Au will reduce the additional inductance (L_{add}) and shift the LC resonance to a shorter wavelength [36].

Zhou et al [37] theoretically proposed a SRR structure with four "capacitive gaps", or "cuts" in 2005 that exhibits a resonance at shorter wavelengths than single gap SRRs. However this proposed structure offers significant challenges in terms of fabrication due to extremely small feature sizes.

The substrate material on which the SRRs sit also has significant influence on the resonant wavelength of the structure. Silicon for example has a refractive index real part of 3.78 and extinction coefficient of 0.012 at 700 nm [38] compared to silica which has an n value of 1.45 and a negligible extinction coefficient at the same wavelength. SRRs fabricated on substrates with a comparatively low refractive index exhibit an LC resonance at shorter wavelengths compared to SRRs on a substrate with a higher n value, assuming the geometry and constituent metal of the structures has not changed [36]. The refractive index of a silicon substrate can also be modified at wavelengths below the electronic band-gap of silicon (1.1

µm) by exciting electron-hole pairs [39]. This can feasibly reduce the magnitude of resonant peaks (LC and plasmon) from the metamaterial.

3.2 Design and fabrication

3.2.1 SRR design

Three SRR designs were created (figure 3.3) for fabrication using NIL with the aim of resonating as close to the resonance saturation limit as possible. This saturation point can be found when a reduction in the SRR dimensions does not yield an increase in the resonant frequency.
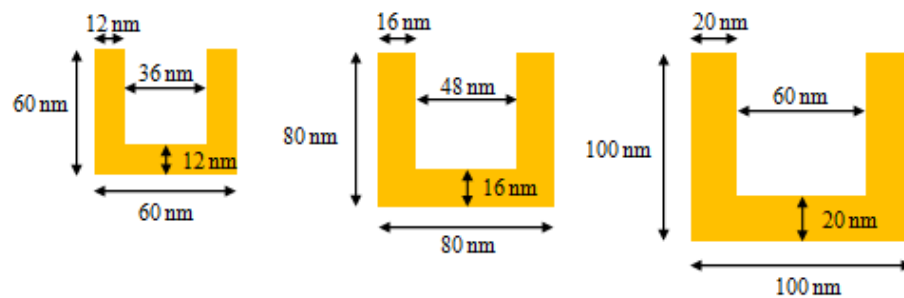
Figure 3.3: Schematic of SRRs designed for fabrication using NIL. The metal thickness in all cases is 15 nm.

Assuming the structure is lossless and ignoring the effect of the plasma frequency of the metal, the idealised resonant wavelength can be found using equation 3.2 and converting the value from frequency to wavelength (λ = c/f). The idealised resonant wavelength was calculated to be 593 nm, 474 nm and 355 nm for SRRs of size (2w+ δ) 100 nm, 80 nm and 60 nm respectively. As silicon substrates are used to support the SRRs the dielectric constant of Si (11.68) was used in the calculations. The limiting effect of the plasma frequency in structures with such small dimensions means that the actual resonant wavelengths will be longer and will not scale linearly.

An SRR design was also created for fabrication using electron-beam lithography. This array of SRRs would enable a comparison to be made between the two lithography techniques in terms of feature size and quality as well as between their spectral responses. For these SRRs the aluminium thickness was increased from 15 nm to 50 nm to produce an improved effective conductor and, consequently, a sharper resonance. To counter the proximity effect, the SRR design was deliberately reduced in dimension, as shown in figure 3.4. By exposing

the electron-beam resist (PMMA) at these dimensions, the final fabricated structure would more closely resemble an SRR with the sizes seen in figure 3.3.
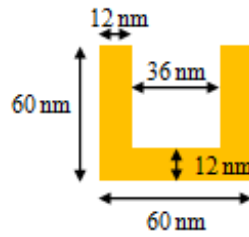
Figure 3.4: SRR dimensions as patterned in PMMA using EBL. All dimensions are reduced in size to counter the increase in size caused by the proximity effect.

3.2.2 Fabrication of SRRs using NIL

Two separate samples must be fabricated to produce the SRR array. A nano-imprint stamp is required to physically define the SRR patterns in a polymer mask. This latter sample, which is patterned by the stamp, will be referred to as the "target sample" throughout this thesis. Fabrication by NIL was performed as follows.

1. A polished silicon substrate is cleaned in ultrasonic bath using acetone, methanol and isopropanol (IPA).

2. 80 nm hydrogen silsesquioxane (HSQ) diluted at a ratio of 1:3 with methyl isobutyl ketone (MIBK) and is spin coated onto the silicon and baked on a hotplate for 5 minutes at 95 °C.

3. The sample is patterned using a Vistec VB6 ultra-high resolution e-beam lithography writer.

4. The HSQ is developed in a temperature controlled environment using tetramethylammonium hydroxide (TMAH) at 23 °C for 30 seconds. It is then rinsed thoroughly in reverse osmosis (RO) water and IPA.

5. Post development, the stamp is hard baked in a furnace at 600 °C for 3 hours.

6. The sample is treated in a hydrophobic, non-stick coating solution of F$_{13}$-OTCS ((Tridecafluoro-1,1,2,2-tetrahydrooctyl)-Trichlorosilane) and heptane (ratio 1:100) for 10 minutes. It is again rinsed in RO water and IPA.

7. 2.5 % 2010 polymethyl methacrylate (PMMA) is spin coated on the silicon target sample and baked for 30 mins at 180ºC, giving a thickness of 60 nm.

8. The stamp is imprinted into the PMMA on the target sample for 5 minutes at a pressure of 25 Pa and temperature of 180 ºC using an Obducat Nanoimprinter.

9. After the stamp is released the thin residual layer of PMMA that remains in the imprinted regions is removed by an anisotropic oxygen reactive ion etch (RIE).

15 nm Al is then evaporated onto the target sample before excess metal is lifted-off by placing the sample in warm acetone. The sample is then rinsed clean in RO water and IPA. The stamp is cleaned using acetone before it is re-used.
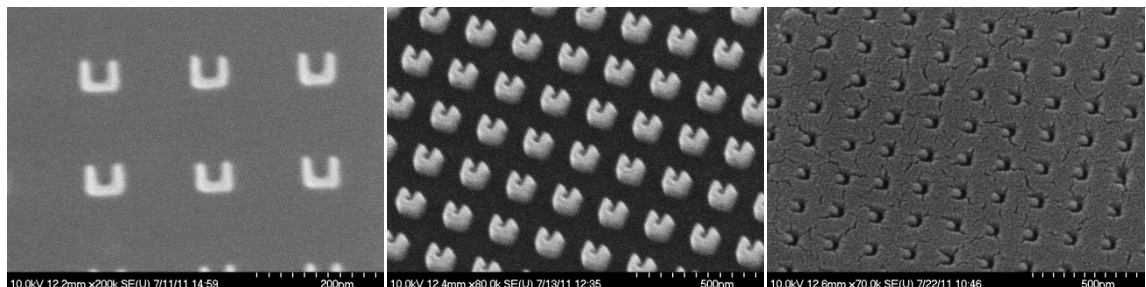
Figure 3.5: Scanning electron micrographs taken during the fabrication process. a) SRRs formed of HSQ with structural width, 2w + δ = 60 nm, b) The stamp shown at a tilted angle, c) The PMMA layer on the target sample following imprinting and showing SRR profiles depressed into the thin film.

The HSQ and MIBK solution is only spun to a thickness of 80 nm to enable the patterning of very small features on the stamp, namely the narrow arms of the SRR. As a result of the HSQ layer being so thin and no etching being performed on the silicon stamp, the PMMA layer being imprinted into is also required to be thin. In this instance it is 60 nm thick. Furthermore, as there is only one layer of PMMA on the target sample that is etched anisotropically to remove residual resist on the substrate, no undercut is present in the resist profile. This lateral sidewall profile of the thin PMMA layer limits the maximum thickness of metal as it will

gradually collect on the imprinted sidewall during deposition and make lift-off in acetone difficult. This concept is visualised in figure 3.6.
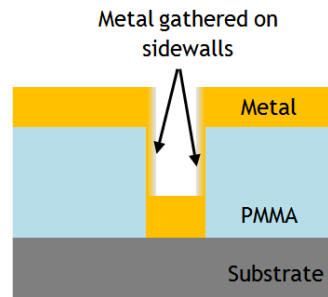
Figure 3.6: Diagram showing the limitations of depositing increased thicknesses of metal with vertical sidewalls and no undercut. Metal build-up on the sidewalls prevents acetone infiltrating the PMMA and lifting-off.

With this fabrication method, using the patterned HSQ to imprint into the target sample rather than an etched stamp represents a novel, "etch-free" technique to patterning small-scale features. Etching features on a stamp can result in tapered or non-lateral sidewalls that can enlarge the dimensions of the imprinted pattern and, consequently, the optical response. It should be noted that SRRs fabricated using tilted NIL [40] and a NIL-ion milling technique [41] have also been reported.

3.2.3 Fabrication of SRRs using electron-beam lithography

To gauge the effectiveness of SRRs fabricated by NIL, SRRs were also fabricated by conventional electron-beam lithography. This allows both sets of split rings to be compared with regard to the quality of their fabrication and their optical behaviour. Aluminium was deposited at a thickness of 50 nm so that the effect of a thicker metal (increase in h, figure 3.2) could be seen. The fabrication of SRRs using EBL was performed as follows.

1. A polished silicon substrate is cleaned in ultrasonic bath using acetone, methanol and isopropanol (IPA).

2. An 80 nm thick layer of 2.5% 2041 PMMA is spun onto the substrate and baked at 180 ºC for 30 minutes.

3. A second, 40 nm thick layer of 2.5% 2010 PMMA is spun on top to create a bi-layer. The sample is baked for 16 hours.

4. The sample is patterned by electron-beam lithography.

5. Resist development is performed using IPA and RO water (at a ratio of 7:3 respectively) for 30 seconds at a temperature of 23 °C.

6. 50 nm aluminium is deposited by evaporation.

7. Excess metal and remaining resist is removed by lift-off, by placing the sample in warm acetone. The sample is rinsed in RO water.

3.2.4 Simulations

The dimensions of the fabricated structures were measured using a scanning electron microscope and used to create a 3D model of the SRRs using Lumerical FDTD solutions software. A single unit-cell of the SRR structure was illuminated using a plane wave source with firstly TE and latterly TM polarisation of the wave at normal incidence (as defined in figure 3.2). The wave source was given a wavelength range from 500 nm to 1000 nm, the same as used for experimental measurements. A periodic boundary condition was applied to the area surrounding the structure to replicate the periodicity of the SRRs in the fabricated array in both the x and y axes. A mesh size of 3 nm was used for the FDTD simulation region. The wavelength dependant real and imaginary components of the refractive index of silicon were taken using data experimentally measured by Palik [42] and applied to the model substrate. The silicon was assumed to be semi-infinite for simulation purposes. The dielectric properties of the Al metal were produced using a Lorentz-Drude model with plasma and collision (damping) frequencies. A perfectly matched layer (PML) was imposed on the material edges within the simulation region to remove unwanted reflections at the boundaries.

The Lorentz-Drude model uses the plasma frequency (ω_p) and a damping constant (γ) associated with a given material to calculate the relative permittivity and permeability. Equations for the calculation of a material's relative ε and μ are given in equations 3.7 and 3.8 respectively [43].

$$\varepsilon_r(\omega) = 1 - \frac{\omega_{p,e}^2}{\omega^2 - \omega_{0,e}^2 + i\gamma_e \omega} \qquad (3.7)$$

$$\mu_r(\omega) = 1 - \frac{\omega_{p,m}^2}{\omega^2 - \omega_{0,m}^2 + i\gamma_m\omega} \tag{3.8}$$

For both equations 3.7 and 3.8 the resonant frequency is denoted by ω_0 and the electric and magnetic responses are represented by the subscripts e and m respectively.
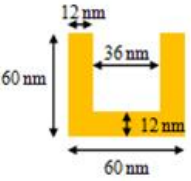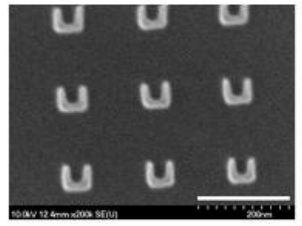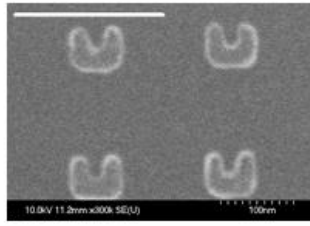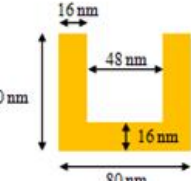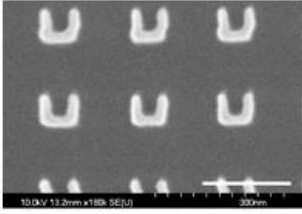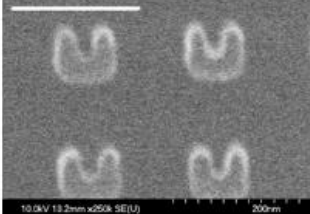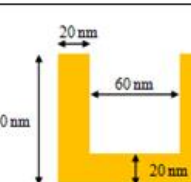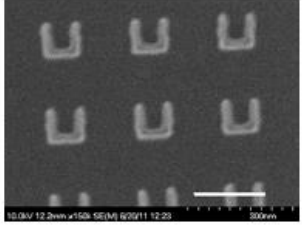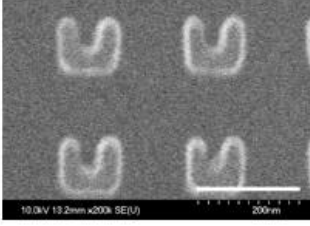
3.3 Results

3.3.1 SRRs fabricated by NIL

Figure 3.5 shows micrographs obtained by SEM of the nanoimprint stamps and the fabricated SRRs and compares the change in dimensions between them. It was found that following imprinting and subsequent metal deposition the arm width (w) and total structural width (2w+ δ) of the Al SRRs increased slightly from the HSQ stamp. This divergence from the dimensions of the imprinting stamp was typically 10 nm or less. Potential explanations for this expansion could include lateral movement of the stamp during separation from the target substrate, etching of the residual layer of PMMA and the comparatively large granularity size of aluminium compared to metals such as gold and silver. The deviance in the fabricated dimensions of the SRRs from the original designs is also quantified in figure 3.7. The total area of the imprinted array, as defined by the stamp, is 5 mm^2.

Due to the absence of an undercut in the imprinted PMMA layer, it was found that only very thin layers of metal could be deposited for lift-off in acetone to be successful. With a total PMMA thickness of 50 nm following the etching of the residual PMMA, metal deposited at a thickness of more than 20 nm was found not to lift-off in acetone. This remained the case despite the sample being subjected to an increased time in acetone and ultrasonic agitation. An increase in the quantity of metal deposited served to raise the likelihood of it collecting on the PMMA sidewalls and preventing the infiltration of solvent for its removal.

Design	HSQ stamp	Metal SRRs	Features
			Total width = 70 nm Gap (δ) = 30 nm Arm width (w) = 20 nm
			Total width = 90 nm Gap (δ) = 40 nm Arm width (w) = 25 nm
			Total width = 110 nm Gap (δ) = 50 nm Arm width (w) = 30 nm

Figure 3.7: Design and micrographs showing differences between NIL stamp patterned with HSQ and fabricated metal SRRs. Feature sizes of the fabricated structures are also given. In all instances the white scale bar represents 200 nm.

Reflection measurements of both TE and TM polarisations were taken using the monochromator and lock-in amplifier with Si detector setup described in chapter 2, figure 2.8 and are shown in figure 3.8 alongside simulated spectra. Measurements were obtained with both incident and reflected light at normal incidence using a 10x objective lens with a numerical aperture of 0.25. Incident light is collimated by the monochromator. Resonant peaks are experimentally measured at 855 nm, 840 nm and 830 nm for SRRs with widths (2w+ δ) 110 nm, 90 nm and 70 nm respectively. A plasmonic peak is visible experimentally at a constant 630 nm with TE polarised light incident.
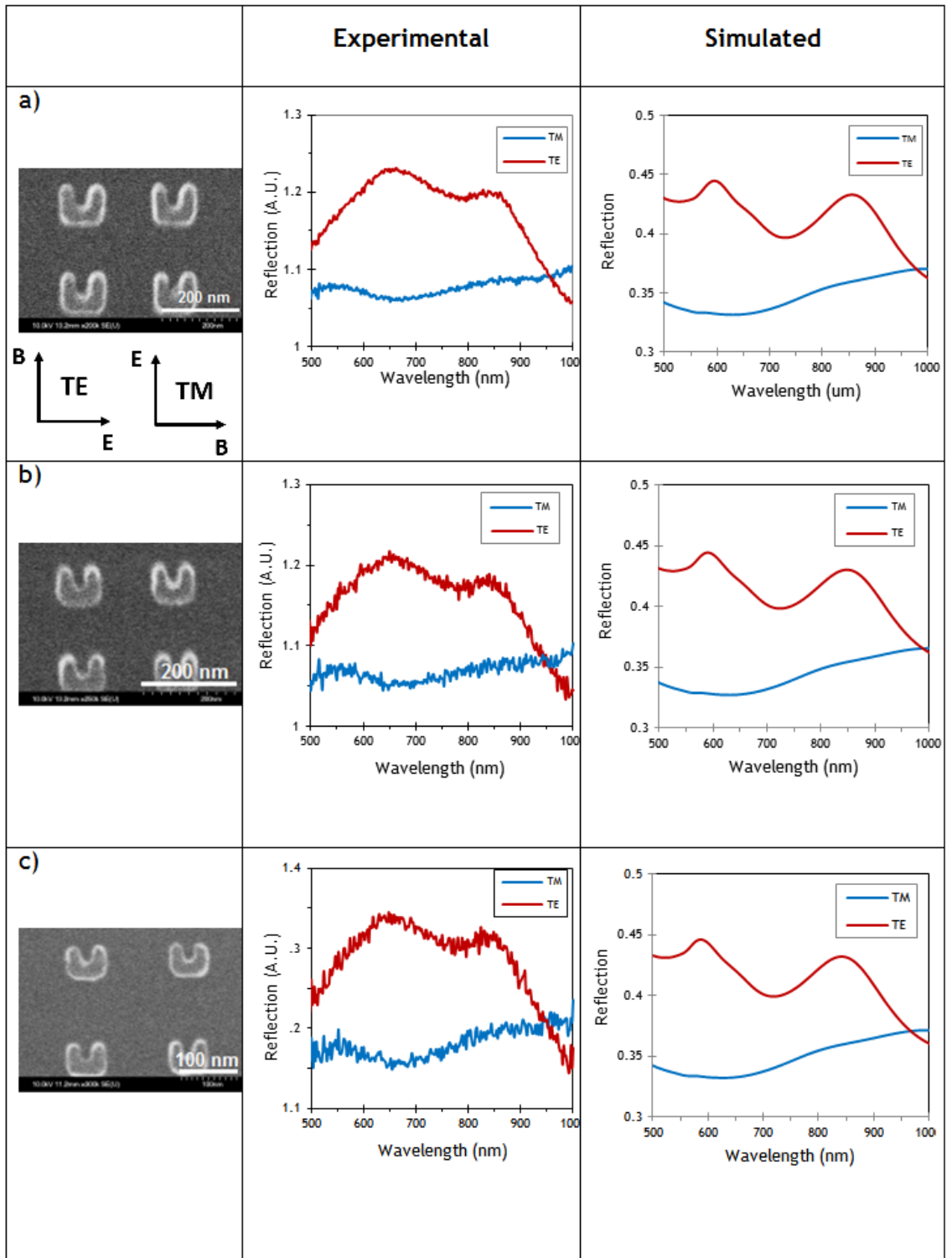
Figure 3.8: Experimental and simulated reflection spectra for SRRs of width (a) 110 nm, (b) 90 nm and (c) 70 nm. An SEM image of part of the respective SRR array is also shown. The reflectance from experimental measurements is given in arbitrary units (A.U.) while simulated spectra are normalised to show a fraction of absolute reflectivity.

There is very close agreement between the experimental and simulated reflection measurements. LC resonance peaks are seen at 860 nm, 852 nm and 843 nm for SRRs with structural width 110 nm, 90 nm and 70 nm respectively. In all cases two peaks are prominent when the electric field of the incident light couples across the gap of the SRR (TE mode). With incident light polarised in TM mode, no significant spectral features are observed. Under TM conditions the electric field fails to couple across the gap that separates the two "arms" of the SRR. As a result a current loop cannot form within the structure and the LC resonance fails to materialise, resulting in a featureless response at the respective wavelength. Because of the limitations in increasing the thickness of the SRRs, the amplitude of the LC peaks is inhibited by the 20 nm aluminium which behaves as a diluted metal. This means that the physical dimensions of the structures confines the mobility of electrons in the metal, preventing them in behaving as they would in a bulk metal and thus affecting the amplitude of the LC response. As these measurements are taken in the visible and near-infrared range, the incident light is below the electronic band-gap of silicon and therefore excites electron-hole pairs in the substrate, reducing the magnitude of spectral peaks. The plasmonic peak and the LC resonance peak in the simulated spectra appear sharper than the experimental counterpart. This can largely be attributed to imperfections in the fabricated structures, such as enlargement and distortion of features. The small fluctuations in the experimental measurements are caused by systematic noise from the monochromator, microscope and lock-in amplifier spectrometer rig. This could perhaps be reduced by measuring a larger area of SRRs to improve the signal-to-noise ratio (SNR).

Although the reflectance of the TE and TM spectra shown in each of the individual plots of figure 3.8 are comparable, it should be highlighted that the reflection scale is given as an arbitrary unit (A.U). This is because transmission measurements required to obtain a percentage reflection value were unable to be taken. It should also be noted that both experimental and simulated spectra have a "false zero", i.e. the value at the origin does not represent zero reflection.

As the change in resonant wavelength is small between the three SRR dimensions, the shift is shown in greater detail in figure 3.9.
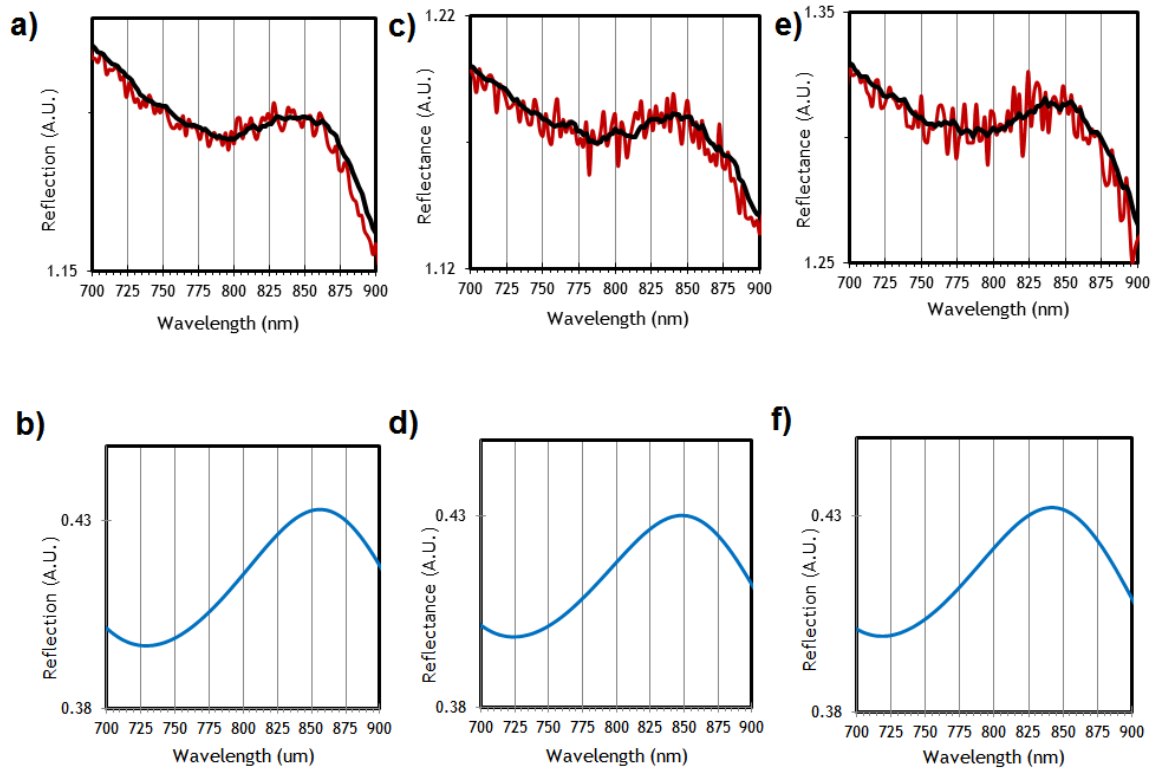
Figure 3.9: Reflection spectra of the fabricated and simulated SRRs showing the LC resonance in greater detail. A moving averaged line of the experimental measurements is shown in black to distinguish the response from systematic noise.   (a) Experimental measurement for 70 nm structure, (b) simulated spectra for 70 nm SRR, (c) Experimental spectra from 90 nm SRR, (d) simulated measurements for 90 nm model, (e) experimental measurement from 110 nm SRR, (f) simulated measurement for 110 nm structure.

The effects brought about by the losses associated with a resonator, such as the SRRs discussed in this thesis, can be quantified in terms of a dimensionless number called the Quality factor, or Q-factor. These effects are usually exhibited spectrally by a damping of the LC resonance peak, including a broadening of the peak and a decrease in its amplitude. The Q-factor is calculated by the following equation:

$$Q = \frac{\omega_r}{FWHM} \tag{3.9}$$

where ω_r is the resonant wavelength and FWHM is the full-width half maximum. The FWHM can be described as the bandwidth of the peak at half of the maximum amplitude. The Q-factor of the SRRs fabricated by NIL is found to be approximately 11.1. This compares to a Q-factor of 8.45 for the simulated SRRs. Study of the measured spectra shows that the comparatively broad plasmonic peak at 650 nm in TE mode narrows the bandwidth of the LC resonance, giving a deceptively high Q-factor.

As the width of the SRR from outer arm to outer arm (2w+ δ) is a defining property in determining the resonant wavelength of the structure, a plot showing the measured LC peak wavelength against the physical size of the SRR is displayed in figure 3.10. As already discussed the ability for the resonant wavelength to scale linearly with the physical dimensions of the SRR begins to breakdown as the structures become increasingly small. Fabricating the SRRs on a lower index substrate such as fused silica has been shown to shift the LC resonant wavelength of SRRs into the visible range. In Lahiri's 2010 paper [36], the fabrication of similar sized SRRs, made using EBL, on a fused silica substrate were shown to produce an LC resonance between 500 nm and 700 nm in wavelength.

Imprinting SRRs into PMMA on a fused silica substrate was rigorously tested. Using the same method as described, a silicon stamp with SRRs patterned in HSQ was imprinted into a 60 nm PMMA layer, but in this instance on top of a 1 mm thick, polished fused silica substrate. Despite the success in using silicon as a target substrate, silica failed to yield the same results. Imprinted patterns in this instance exhibited poor definition in the form of rounded edges and an increase in dimension. A possible cause of this failure is the difference in the thermal conductivity, k, between silicon and fused quartz. The thermal conductivity denotes how heat is transferred through a given material and is measured in Watts per metre Kelvin ($Wm^{-1}K^{-1}$). Thermal NIL requires that the polymer being imprinted into is heated in order to reduce its viscosity and aid its flow around the stamp or mould. A reduced polymer heat can result in patterns failing to be properly defined as well as non-vertical sidewalls. Silicon has a thermal conductivity of k = 149 $Wm^{-1}K^{-1}$ whereas fused quartz exhibits k = 1.3 $Wm^{-1}K^{-1}$, meaning heat can transfer through silicon at a greater rate than in fused quartz. In addition to the silicon substrate having a much higher thermal conductivity to the fused quartz substrate, the Si target substrate has a thickness of 500 μm compared to the 1 mm thick quartz. The Obducat Nanoimprinter used in fabrication only provides heat from beneath the target sample and not from the direction of the imprinted stamp positioned on top. Although 15 nm of Al was deposited onto the patterned PMMA on quartz (again following an etch of the residual PMMA layer), metal lift-off was repeatedly unsuccessful. This suggests a continuous film of Al was present and prevented acetone from removing the PMMA layer. Recreating the structures shown at ever smaller dimensions on a silicon substrate introduces multiple

fabrication problems and, even if achieved, will not significantly increase the resonant frequency [34,37].
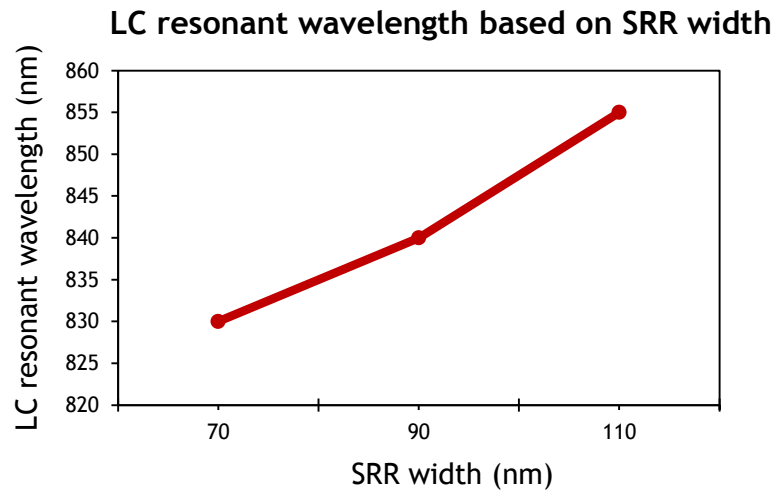
Figure 3.10: LC resonance wavelength against the total width of the SRRs.

3.3.2 SRRs fabricated by EBL

The SRR array fabricated by electron-beam lithography was measured using the same method as was used for the SRRs fabricated by NIL. A micrograph of the fabricated metamaterial is shown in figure 3.11. It is observed that the structural similarity to the original design is not as close as seen with the previously used NIL stamp and consequent SRRs. Furthermore the SRRs exhibit less uniformity, often differing in size and shape, and a broadening of the "wire" that connects both arms. The total width of each SRR was found to be approximately 90 nm with an average gap between the two arms of 30 nm. As a result of the deviance from the original design the periodicity of the SRRs in both the x and y axis is approximately two and a half times (rather than double) the width of the structure.
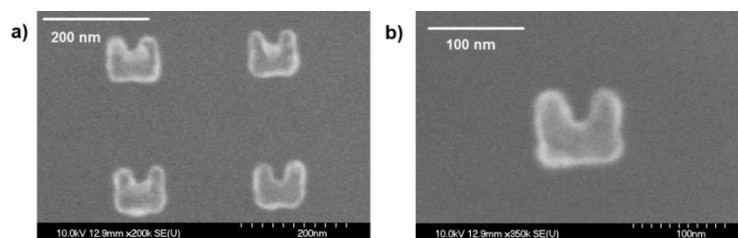
Figure 3.11: Micrographs of the SRRs fabricated by electron-beam lithography. (a) Four SRRs, showing the lack of uniformity from structure-to-structure, (b) A single SRR with total width 90 nm.

The experimental reflection measurement of the array (figure 3.12) shows a broad resonance under TE mode at approximately 850 nm. Although broad, with a FWHM of around 150 nm, the LC peak is much more prominent than seen for the SRR

made by NIL. This is because of the increase in the metal thickness used from the nanoimprinted SRRs, from 15 nm to 50 nm Al. The Q-factor is calculated as 5.66. It should be remembered that the reflection scale is given in arbitrary units, meaning a direct comparison of the measured amplitude of the peaks obtained from the NIL fabricated and EBL fabricated structures cannot be done accurately. However reflection measurements from the EBL fabricated structures show a stronger LC resonance than plasmon resonance, likely due in part to the increased metal thickness. A shift in the plasmon resonance is also noted, from 630 nm to approximately 560 nm. This shift can be caused by combined changes in the dimensions of the structures and their periodicity [43].
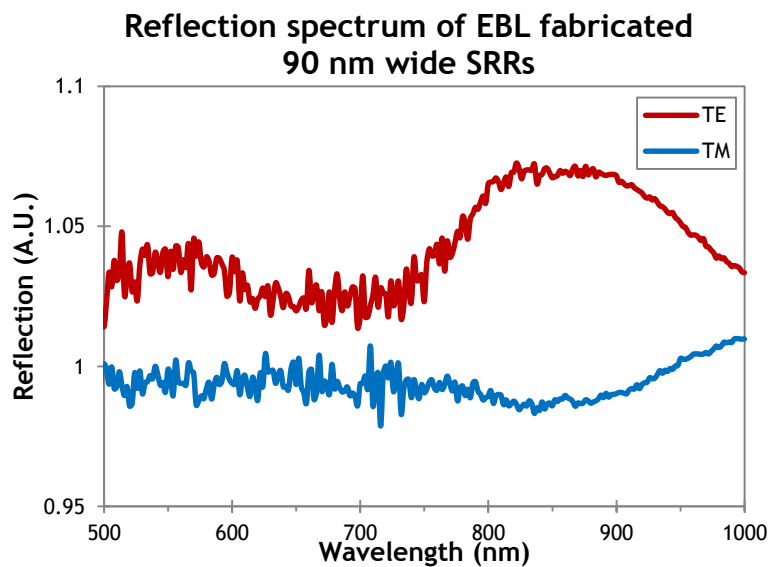
Figure 3.12: Reflection measurement for 90 nm wide SRR fabricated by EBL with 50 nm thick Al.

3.4 Discussion

It is observed from the reflection measurements taken of the SRRs made using NIL (figure 3.9) that, although small, there continues to be a measureable shift in the LC resonance between the three SRR designs. The shift in the resonant wavelength decreases as the total width of the SRRs are reduced from 110 nm to 90 nm and finally to 70 nm. It is reasonable to presume that any further reduction in the dimension of the SRRs would fail to significantly reduce the resonant wavelength. Furthermore, successfully fabricating SRRs with smaller features than shown in this chapter becomes increasingly more difficult due to lithography limitations. Fabrication of small-scale SRRs on a lower index substrate such as fused silica would reduce the resonant wavelength but the saturation effect due to the mobility of electrons in the metal would still be inhibitive.

The inability to deposit metal at thicknesses greater than 15 nm reduces the amplitude of the LC resonant peak. Comparison of the SRRs fabricated by NIL with those made using EBL shows that Al 50 nm thick produces a distinct LC resonance peak that is more prominent than the plasmon peak. This is despite the structural quality (uniformity and definition of features) not being as good as seen with the imprinted SRRs. There does not appear to be any significant difference between the LC resonance bandwidths of either set of resonators and the resonant wavelength is also unchanged.

3.5 Chapter conclusions

Small-scale "U-shaped" SRR have been fabricated by NIL and measured both experimentally and by simulation. The SRRs were found to be of dimensions that were close to the theoretical saturation limits that prevent a reduction in the resonant wavelength. This work in this chapter demonstrates a nano-imprint technique that enables the fabrication of small-scale SRRs with a minimum feature size of 20 nm. Using patterned HSQ resist to imprint represents a novel stamp production technique that does not require any etching of the substrate. This method could be used to imprint other designs and patterns with sub-100 nm features. SRRs fabricated by imprinting were compared with equivalent structures made using EBL. There were no significant differences in the resonant wavelength or peak bandwidth. It was found that the maximum metal thickness was inhibited by the NIL process, resulting in a resonant peak amplitude lower than seen with SRRs made by EBL.

Chapter 4

Optical detection of organic materials using SRRs
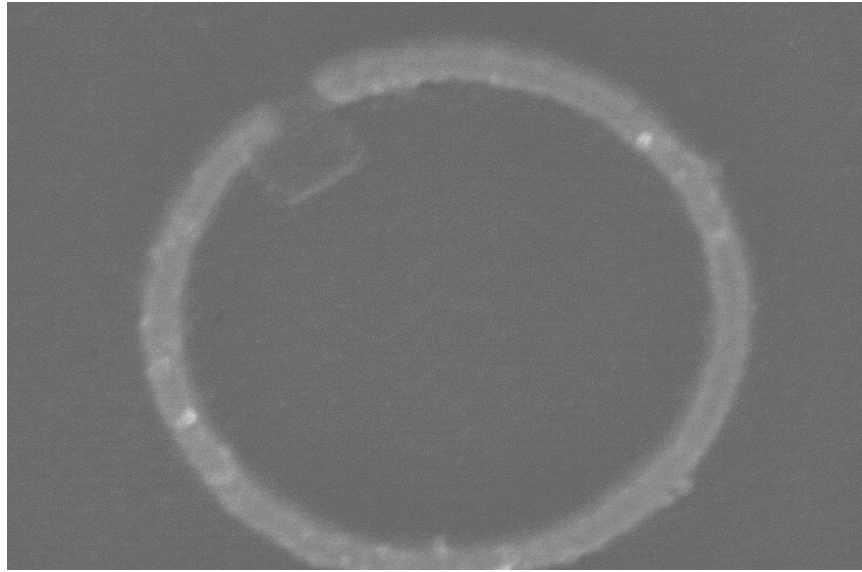
4.1 Introduction

It has been shown in chapter 2 that split ring resonators can be used to produce electromagnetic resonances at given wavelengths by changing the dimensions of the structure, namely the width or diameter. By "tuning" these resonances to the same resonant wavelength of a given material or molecule, the molecular resonance can be significantly enhanced. Using SRRs, and indeed other structures that produce a plasmonic resonance, to examine the spectroscopic behaviour of a wide variety of substances of interest is an increasingly important application of metamaterials [44-50]. This use as an optical sensor makes metamaterials of ever increasing interest to commercial ventures. By locating a material or organic compound at certain strategic regions within close proximity to a SRR it is possible to increase the resonant absorption of a phonon resonance. Designing and manufacturing a split ring resonator that is characterised as being highly sensitive makes it possible to enhance the molecular resonance of even very tiny quantities of a substance. This has advantages in the fields of security, defence and healthcare.

This chapter will study the means in which split ring resonators (and their various geometries) can be used to sense organic materials. In particular the sensitivity of numerous regions of a SRR are researched to experimentally distinguish the positions most advantageous for optical sensing; the so called "hot-spots" [51], areas where the electric field is strong in the structure. This is achieved by optically measuring the reflection spectra of SRRs designed to exhibit resonance at a close wavelength to that of the carbonyl bond resonance present in PMMA that is localised at positions physically near or on the SRR. Commonly these hot-spots are distinguished using computer modelling of an SRR structure [52-54].

4.1.1 Molecular spectroscopy

Characterising a substance using optical spectroscopy to quantify its presence and properties can offer a number of advantages when compared to alternative methods used, such as chemical sensing [55]. Firstly, the spectrometers widely commercially available can typically measure a wide frequency range, from visible or near infra-red frequencies up to terahertz range. This wide spectral range covers the resonance and absorption frequencies of a multitude of organic

compounds and substances, particularly in the infra-red region [56,57]. Secondly, in most instances characterising a material using optical spectroscopy, either by reflection or transmission, is non-invasive and does not damage or alter the substance under examination. This may not be the case if the material is photo-sensitive. Perhaps one of the greatest advantages of sensing using spectroscopy from a commercial perspective is that it measurements can be obtained quickly and at low cost.

As will be shown later in this and the subsequent chapter the absorption peaks from H_2O and CO_2 present in the surrounding atmosphere are detectable by FTIR – present near 6 μm (and other broad wavelength ranges) and 4.25 μm respectively. Examining a substance that has molecular resonance or absorption at the same wavelength as atmospheric features can make characterisation difficult, particularly if the response from the molecule is not enhanced. This interference can be minimised by purging the atmosphere surrounding the sample and FTIR spectrometer with an inert gas such as nitrogen or argon.

4.1.2 The effects of SRR geometries on optical response

The previous chapter has shown the optical response of small-scale "U-shaped" SRRs and discussed the limitations in reducing their dimensions. Although shifting the resonance to ever shorter wavelengths becomes increasingly difficult, modifying the geometry of the basic "U-shaped" single split ring resonator can produce an optical response that yields certain advantages, particularly with respect to sensing. However for the purpose of optical sensing, in which the molecular resonance of a particular substance is enhanced to make it more easily detectable, it is important that a metamaterial exhibits a high quality factor. This ensures that only the molecular resonance of the substance of interest is enhanced but other molecules that resonate at nearby frequencies are not enhanced. Furthermore the application of a detectable substance to a metamaterial shifts the wavelength of the plasmonic, owing to the refractive index change. This will be demonstrated later in this chapter. A resonance shift can be more easily detected with a sharp, narrow transmission or reflection peak than a broadband peak with low amplitude.

Introducing asymmetry into the split ring structure has been shown to increase the quality factor of the peaks generated by optical stimulus and introduce new resonance modes [45,58]. These asymmetric-split ring resonators (A-SRRs), shown in figure 4.1, are characterised by having two splits (gaps) in the ring resonator. This additional capacitive element and the presence of two separate arcs of differing length (and therefore differing inductance) produce two resonances compared to the single peak exhibited by single-gap SRRs. With the electric field strength strongest at the ends of the arcs of a SRR, the asymmetry of the double split structure leads to the generation of plasmonic resonances that are enhanced by the end of the neighbouring arc.
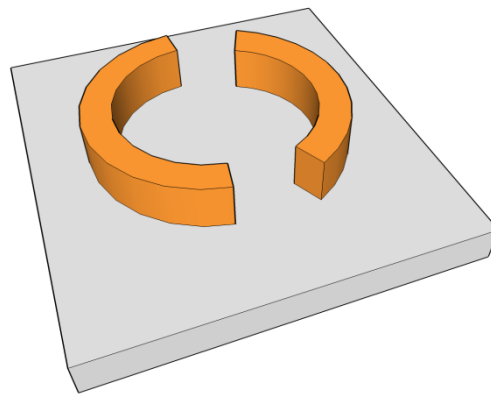
Figure 4.1: A model of an A-SRR structure.

As with the single-split, symmetric SRR, the optical response of the A-SRR is dependent on the polarisation of incident light. In order for two distinct resonances to be produced (one from each arm of the A-SRR) the electric field vector must run parallel to the length of the metal arcs. Under this transverse electric condition, each arm of the structure produces a plasmonic resonance and their close proximity to one another results in a phase change at either side of the top and bottom gaps. Depending on the level of asymmetry in the structure, under transverse magnetic conditions a current loop cannot easily circulate around the structure due to the inability for electric field coupling across the gaps between the arcs. This results in peaks with greatly reduced amplitude (if at all) to those seen under transverse electric polarised light, where the electric field is orientated along the length of each individual metal arc, perpendicular to the gap. When comparing with single-gap SRRs, the definition of TE and TM modes for

A-SRRs can, in simplistic terms, be thought of as a 90° rotation of the electric field.

It should be noted at this point that A-SRRs also exhibit a hidden resonance in which the optical electric field is distributed within the A-SRR structure. This is commonly referred to as the "trapped mode" and exists at the trough between the two resonance peaks shown in reflection measurements in figure 4.2. It is also noted in this figure that two peaks with a reduced amplitude are visible under TM incident light. This is a result of minor "leakage" of the TE mode through the polariser which induces a weak current in the structure. The magnitude of the unpolarised light transmitted through the polariser compared to the transmitted polarised light can be determined by the degree of polarisation (DOP), where a DOP of 100% indicates a perfectly polarised wave and a DOP of 0% indicates an unpolarised wave. Depending on the DOP, a partially polarised wave will create a superposition of the polarised and unpolarised components.
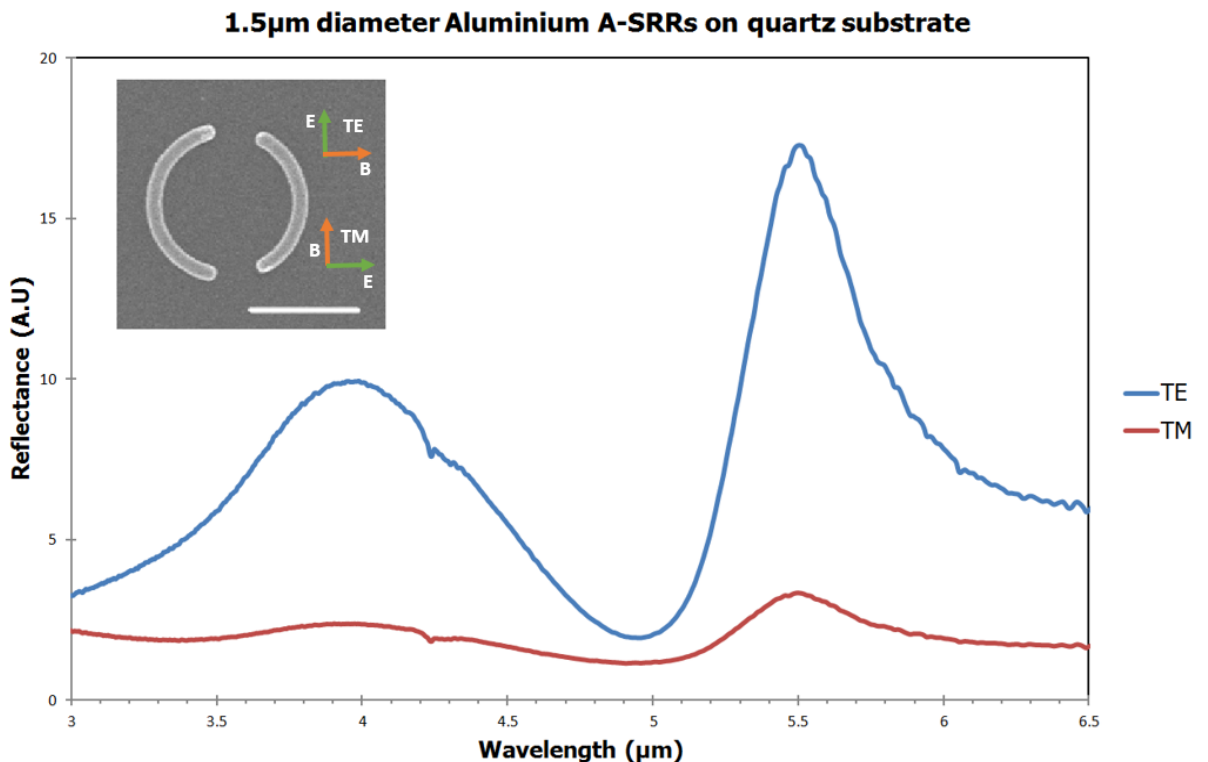
Figure 4.2: Reflection spectra from an A-SRR from both TE and TM polarised incident light with SEM of A-SRR inset. The scale bar represents 1 μm.

Similarly to SRRs, the resonant wavelength of the asymmetric ring structures shifts proportionally with dimensions, as the inductive and capacitive values are changed. This shift in resonant wavelength can be seen in figure 4.3, in which the

resonance of the CO_2 absorption band at 4.25 µm is progressively enhanced by varying the diameter of A-SRRs. When the resonant wavelength of the A-SRR matches that of the CO_2 absorption band the reflection signal can be seen to increase significantly in amplitude.
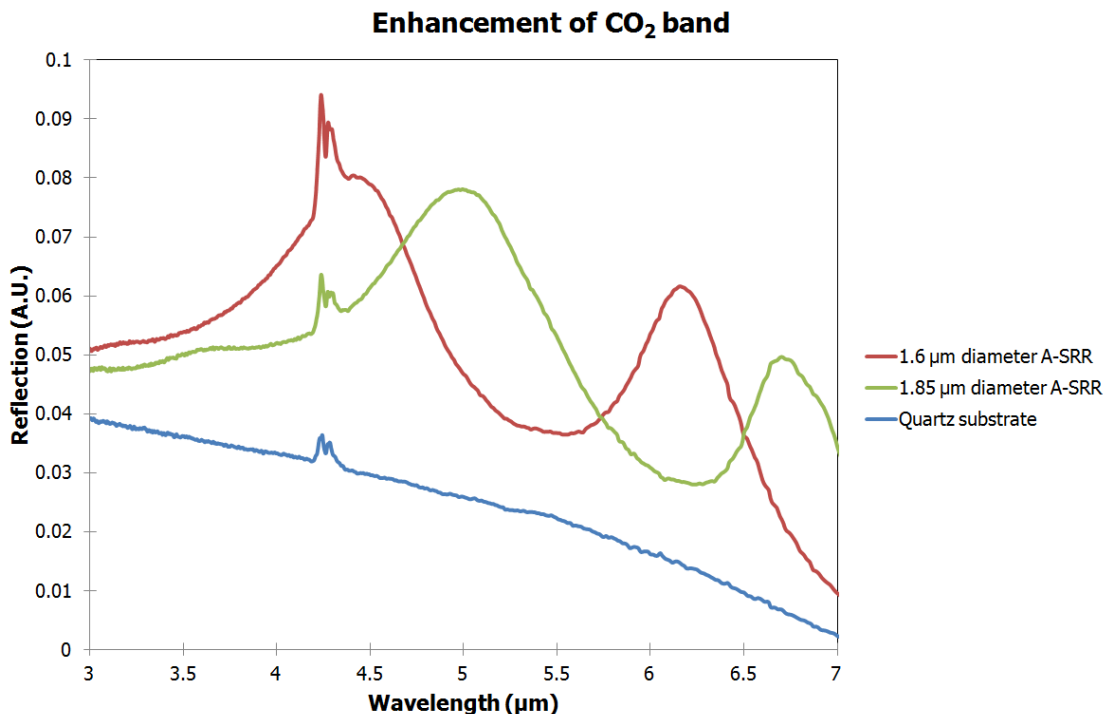
Figure 4.3: Enhancement of the resonance of the CO_2 absorption band. The resonance at 4.25 µm can be seen to increase in amplitude from a bare, unpatterned quartz substrate (blue) to slight amplification when positioned on the leading edge of a peak (green) to greater enhancement when tuned to the resonant peak of an A-SRR (red).

Although A-SRRs can exhibit a greater quality factor than their SRR counterparts and have the added advantage of producing two plasmonic peaks in reflection and a trapped mode, this chapter will primarily focus on "C-shaped" single-gap SRRs. By localising PMMA at confined positions on or within close proximity to a SRR designed to resonate at a particular wavelength, it is possible to experimentally demonstrate the regions that exhibit the greatest sensitivity or, in other cases, a much reduced sensitivity. This PMMA localisation concept follows on from work by Zhang et al in which monolayers of octadecanthiol (ODT) covering the entirety of a SRR array are detected [59]. PMMA has previously been used, both in the form of thin films and localised blocks, to demonstrate the ability of A-SRRs in detecting the molecular Fano resonance of organic materials [60].

The "C-shaped" single-gap SRRs that are investigated in this chapter have been designed to resonate in the mid-infrared and have a small (in comparison to the

ring structure) 150 nm gap to improve resonant coupling between the ends of the arc.

4.2 Detection of PMMA

PMMA has several benefits as an analyte in optical sensing. It exhibits a C=O stretching band of ester known as the carbonyl bond [61] that absorbs at 5.75 μm, as shown in figure 4.4. The near infra-red and mid infra-red wavelength range is of great interest for the optical sensing of a variety of molecules and organic compounds. PMMA's function as an electron-beam resist also makes it particularly useful for the purpose of localisation. It can, depending on the molecular weight, be spun on a substrate at a wide range of thicknesses by varying the spin speed. Furthermore, as PMMA is a positive electron-beam resist, it can be patterned to leave localised blocks by exposing the regions that are to be removed. This "inverted" method of writing patterns in PMMA is time consuming and not reproducible on a large scale, but it does enable the accurate positioning of an organic compound in small quantities and at small dimensions. PMMA can be used as a negative resist if written using extremely large doses [62]. However although this would make the localisation process simpler, exposing PMMA at such high doses breaks the free carbonyl bond at 5.75 μm and diminishes its usefulness as an analyte [62].
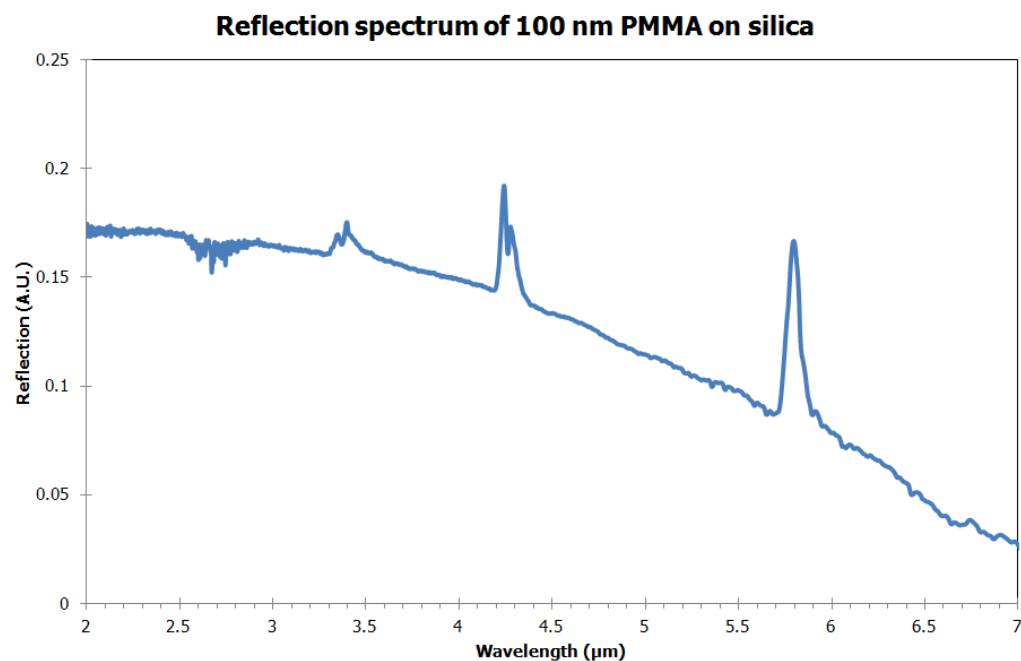
Figure 4.4: Reflectance spectrum of 100 nm PMMA on fused silica.

The carbonyl group is common to numerous organic compounds, including ketone and ester, and is characterised by a carbon atom double bonded to an oxygen atom, shown in figure 4.5. The positive carbon atom is susceptible to attack from negatively charged ions (nucleophiles). Under such circumstances the double bond between the carbon atom and oxygen atom is broken and a water molecule is removed.
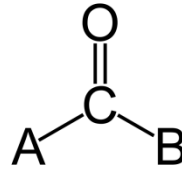
Figure 4.5: The carbonyl group, exhibiting a double bond between the carbon and oxygen atoms and single bond to molecules A and B.

Figure 4.4 also shows numerous features other than the carbonyl bond at 5.75 µm. The two peaks near 3.3 µm are attributed to the C-H bond stretching of CH_2 and CH_3 [63]. A sharp peak visible at 4.25 µm is caused by the presence of CO_2 in the surrounding atmosphere. Small, narrowband troughs between 2.5 µm and 3 µm and 5 µm and 7 µm are indicative of the presence of H_2O. This chapter will focus on the enhancement of the most prominent feature obtained spectroscopically from the PMMA, the free carbonyl bond at 5.75 µm. Table 4.1 lists the molecular vibration and absorption features that are found from PMMA [63,64].

Wavelength (µm)	PMMA feature
3.42	CH_2 and CH_3 stretching vibration
5.75	Free carbonyl bond
5.89	Carboxylic acid groups present in the PMMA
6.07	Carbon atom double bonding, C=C.
6.63	CH_3 bending
6.89	In-phase bending of CH_3

Table 4.1: List of molecular vibrations and absorptions exhibited by PMMA and the wavelength at which their presence is visible.

Using PMMA as an analyte and inversely exposing it to leave blocks of the substance at positions of interest on or near a SRR enable it to act as a probe of the metamaterial. By designing and fabricating SRRs to resonate at approximately the

same wavelength as the carbonyl absorption band at 5.75 µm, the optical reflection response of the PMMA can be detected. By localising the PMMA into small, square blocks and positioning it in different locations of interest, the response from each location can be measured to determine the regions of the SRR that offer the greatest sensitivity. This can be quantified and used to indicate the metamaterial's ability to function as a sensor of organic compounds.

4.3 Fabrication and simulation

SRRs were designed and fabricated as shown in figure 4.6. Localised PMMA blocks 150 nm by 150 nm were placed in regions of particular interest, namely the "hot spots" and "cold spots", which are discussed later in this chapter. The periodicity of the SRR array was 3.1 µm in both the x and y axis, twice the diameter of the structure.
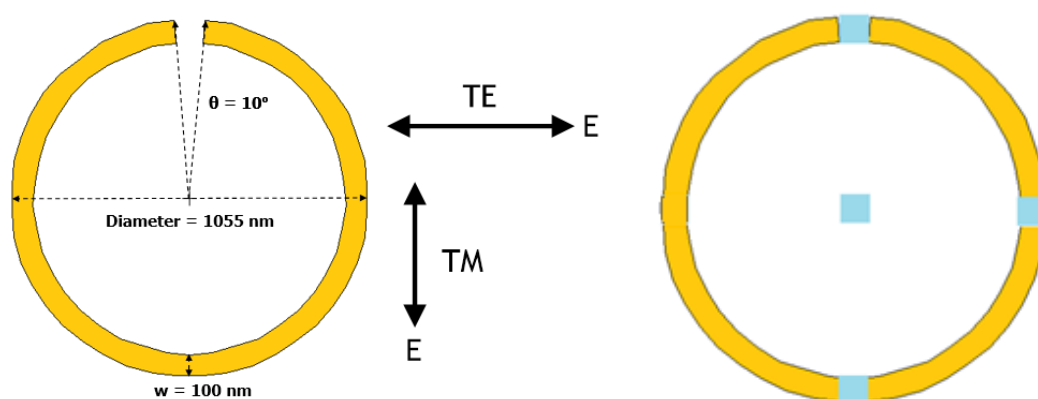
Figure 4.6: SRR geometry and polarisations used and regions of particular interest for probing using PMMA.

4.3.1 Fabrication

Fabrication of the split rings with localised PMMA involves a number of additional steps when compared to the SRRs fabricated by EBL in chapter 2. Firstly, a series of metal alignment markers must be fabricated onto the substrate to act as a constant positional reference for all subsequent patterning. Fused quartz, SiO_2, was chosen to act as a substrate due to its refractive index being significantly lower than silicon, approximately 1.45 for SiO_2 [65] compared to 3.42 for Si [66]. This comparatively low index substrate shifts the resonance of an SRR of given dimensions to shorter wavelengths than would be seen if fabricated on Si or another high index material. This simplifies the fabrication of the SRRs and the

subsequent localisation of PMMA as the dimensions of the structures are larger than would be necessary if made on Si.

The fabrication and localisation process is performed as follows and is shown in figure 4.7. As, unlike Si, fused quartz is non-conductive, a thin 6 nm charge dissipation layer of Al is deposited on top of the electron-beam resist in advance of each EBL exposure. This Al layer is removed after exposure but before development using Microposit CD-26 developer.

1. Alignment markers are exposed using EBL and then deposited with 10 nm Ti and 100 nm Au.

2. The SRR structures are fabricated in the way as described in chapter 2 using EBL, only aligned with respect to the Au markers. 10 nm Ti and 100 nm Au are used as the constituent metals.

3. A 100 nm thick layer of single type PMMA (4% 2010) is spun onto the sample. As PMMA is a positive electron-beam resist, the regions of PMMA that are to be removed are exposed. Therefore only the areas that will become localised PMMA blocks are not exposed. This makes the pattern particularly sensitive to the electron-beam proximity effect. The PMMA is developed using a mixture of IPA and RO water at a ratio of 7:3.
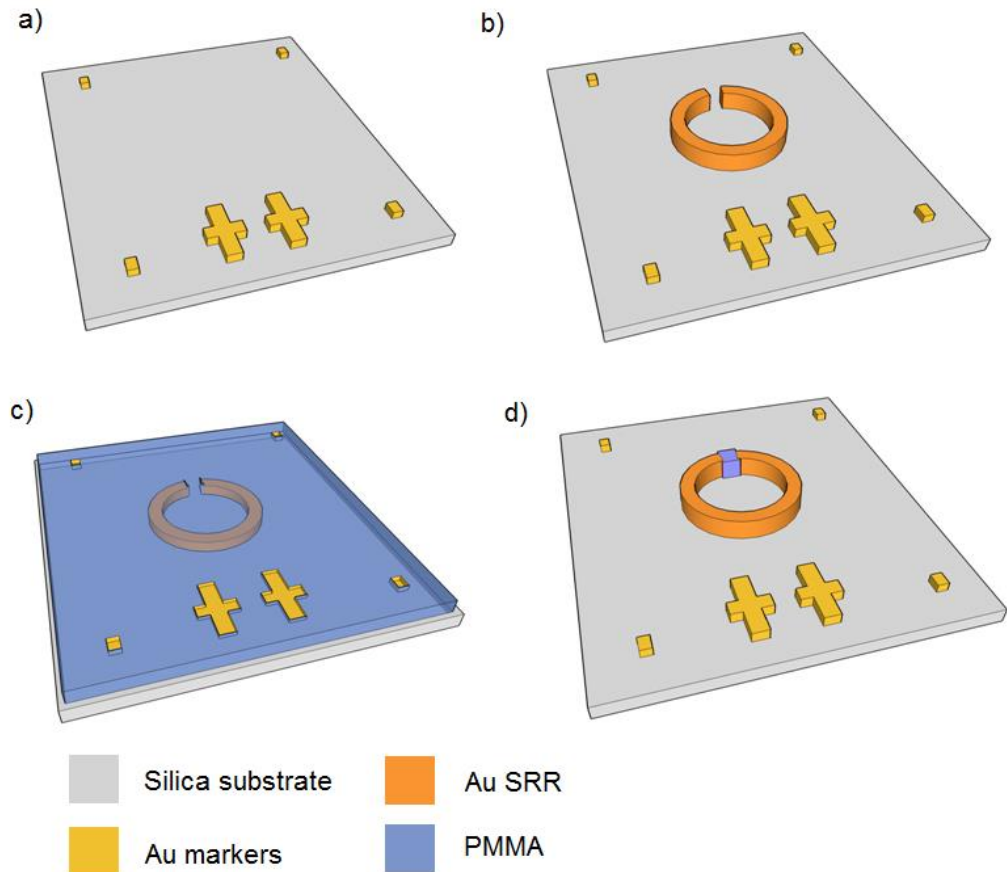
Figure 4.7: Fabrication process used in localising PMMA on or near SRRs. (a) Ti/Au markers are patterned and deposited on the silica substrate, (b) The SRRs are exposed in proximity to the markers and metal deposited, (c) A 100 nm PMMA layer is spun on the sample (d) The PMMA is exposed to leave the localised block in the required position, again using the markers as a reference.

4.3.2 Simulation

The SRR structures with localised PMMA were simulated by Henrique Vilhena and Scott McMeekin of Glasgow Caledonian University using Lumerical FDTD software. A single unit-cell of the SRR was created and periodic boundary conditions with perfectly matched layers applied. The Ti and Au metal layers, the SiO_2 substrate and PMMA were modelled using the complex refractive index data from Palik [67]. A plane wave source with a wavelength range from 3 μm to 16 μm was applied to the top face of the unit-cell and the reflectance measured. Field plots showing the simulated electric field behaviour of the structure (Ez component) were also obtained.

4.4 Measurement and results

All optical experimental measurements were taken using the FTIR set-up described in chapter 1. Only measurements taken using TE polarised light (with the electric field coupled across the SRR gap) are shown in the remainder of this section.

4.4.1 Response of SRRs without the presence of PMMA

Before examining the optical response from SRRs with PMMA, the SRRs without any analyte applied were first measured and simulated. The experimental and simulated reflection spectra for the SRRs over a broad wavelength range and for TE and TM incident polarisations (defined in figure 4.6) are shown in figure 4.8.
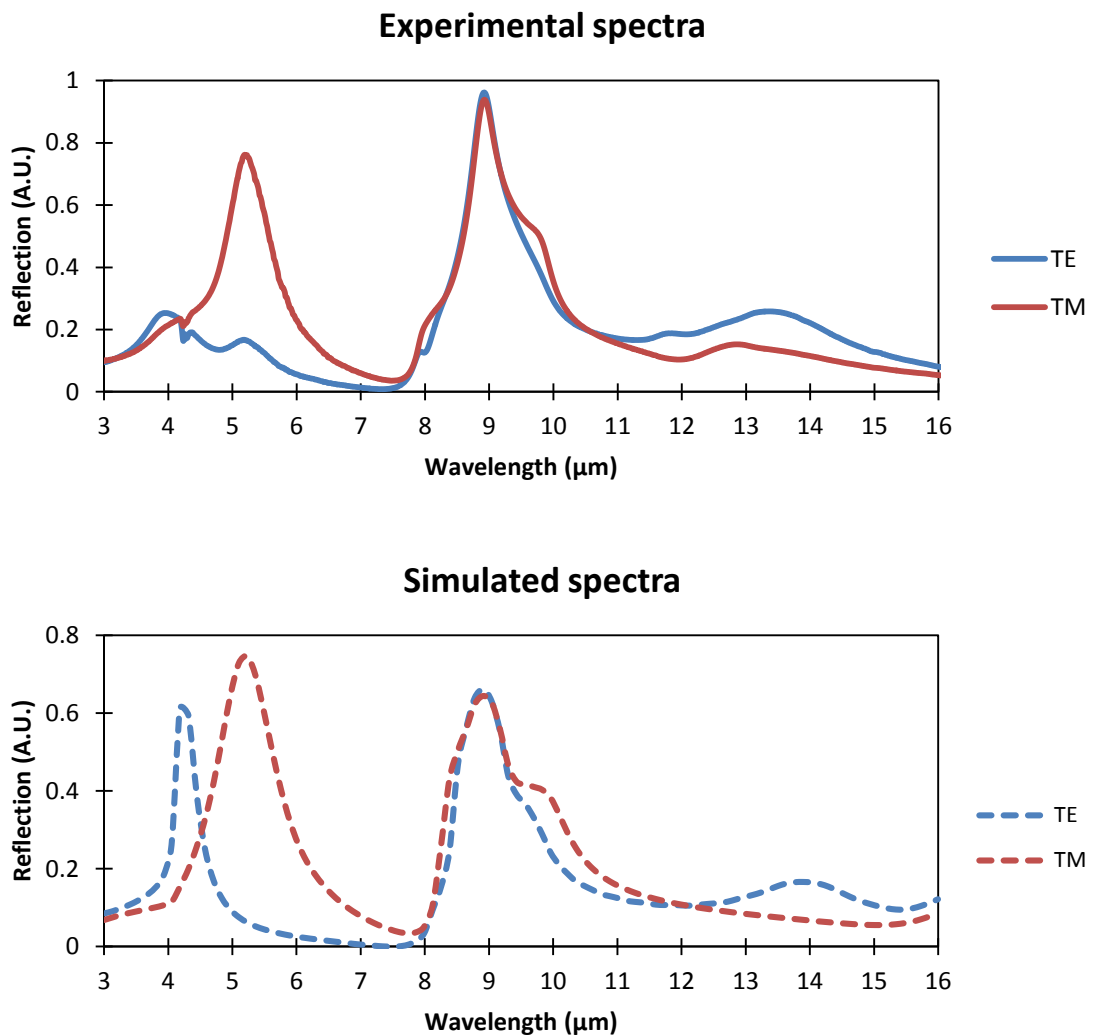
Figure 4.8: Experimental (top) and simulated (bottom) spectra of the SRRs for the E-field both parallel (TE) and perpendicular (TM) to the gap of the SRR.

The presence of atmospheric CO_2 is seen in the experimental measurements at 4.25 μm. Both experimental and simulated spectra show a strong, broad peak at 9 μm for both polarisations. This is attributed to the fused silica substrate [68]. With incident light polarised in TM mode, experimental and simulated spectra both show a strong resonance at approximately 5.25 μm. For TE polarised light, a peak is visible at 4 μm from the experimental measurement and 4.2 μm from the simulated measurement. Although it should be noted that the strength of reflectance in all cases is given using arbitrary units (A.U.), the amplitudes of peaks in the experimental TE spectrum can be directly compared to those of the experimental TM spectrum. Similarly the amplitudes of the simulated spectra can be compared with each other. In order for a comparison between the amplitudes of an experimental and simulated spectrum, normalisation would have to be performed. The amplitude of the experimental peak at 4 μm appears to be lower in relation to the amplitude of the equivalent peak seen at 4.2 μm from the simulations, when comparing with the resonance at 5.25 μm in TM mode. This can jointly be explained by imperfections in fabrication and in characterisation, such as the accuracy of polarisation angle with respect to the array of SRRs. Accuracy of polarisation may also explain why the peak at 5.25 μm can be seen, albeit at a much reduced amplitude, in the experimental TE measurement but not the simulated TE spectrum. The effect of the polarisation angle of the incident electric field on similar (but more asymmetric) single gap SRRs has been studied by Chen et al [69].

A broadband resonance is also visible at longer wavelengths for TE polarisation at 13.6 μm in experimental measurements and 14 μm in the simulated spectrum. To gain an understanding of the behaviour of the SRRs at each of these peaks, field plots were produced from the simulations to show the electric field distribution in the structure. Figure 4.9 shows the electric near-field of the structure at various wavelengths, corresponding to the peaks seen in simulated reflection spectra. The field plot associated with the resonance at 14 μm shows the electric field largely confined to the regions near the gap of the split ring. It suggests, due to this confinement as well as the difference in polarity at the ends of the metal (indicative of a dipole), that this is the fundamental mode, often termed the LC resonance [70]. It is noted that this resonant peak is only present when the electric

field of the incident wave is parallel to the x-axis of the model, i.e. when it couples across the gap of the SRR.
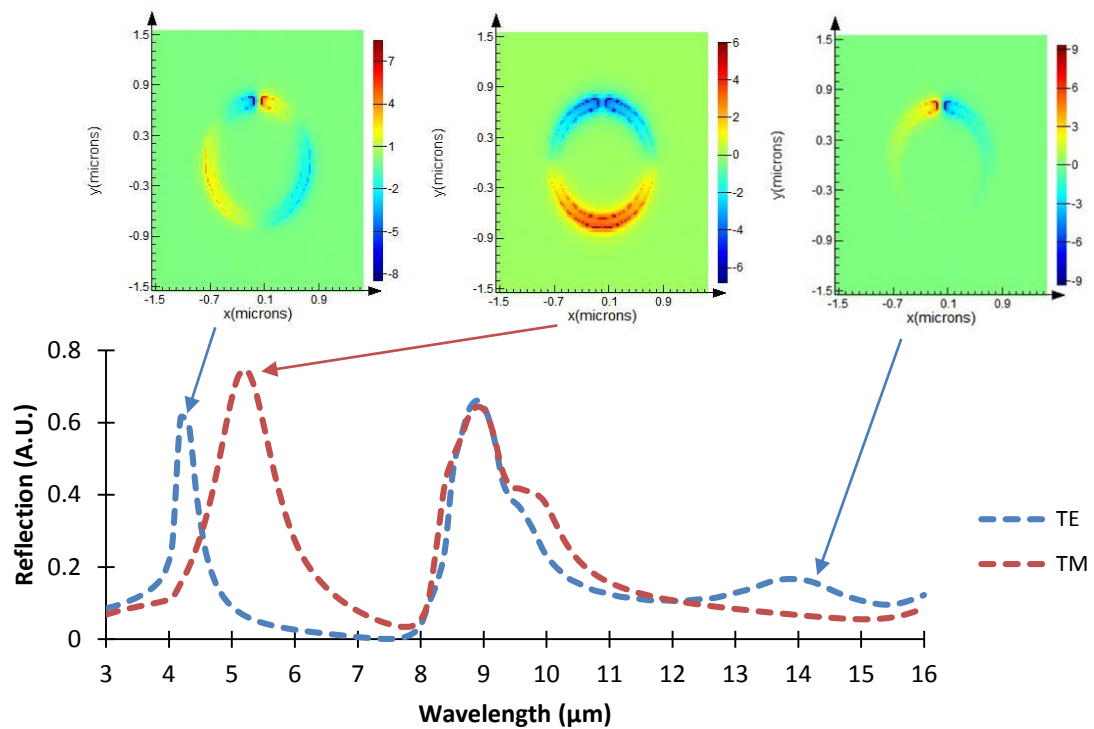
Figure 4.9: Field plots of the electric field distribution at different resonant wavelengths.

A field plot of the structure taken at 4.2 µm under TE conditions shows what appears to be a higher order mode of the one exhibited at 14 µm. As well as the change in polarity of the electric field across the gap, a second similar feature is seen across the arm of the SRR but with a lower field strength. With TM polarisation the electric field distribution changes dramatically and polarity is seen to be the same in sign at both ends of the gap in the SRR. A change in sign is instead exhibited along the y-axis between the metal near the gap and the bottom region of the split-ring structure. Using these field plots the physical areas of greatest sensitivity to an analyte can be predicted. It is noted that a number of distinct "cold spots", areas where the electric field strength is near zero, are present for both polarisations and at each studied resonance.

Because of the presence of the carbonyl bond absorption feature at 5.75 µm, the bulk of the work contained in this chapter will focus on the two resonances at near infra-red wavelengths - 4 µm (experimental) under TE polarised light and 5.25 under a TM polarised incident wave.

4.4.2 Sensitivity of SRRs with 100 nm thick PMMA film

SRRs completely covered in a 100 nm thick layer of PMMA were examined as a precursor to SRRs with localised PMMA. The optical reflection from the SRRs in this instance, shown in figure 4.10, displays a shift in the resonant wavelength, from 5.23 µm without the presence of PMMA to 5.65 µm. This represents a shift in resonant wavelength of 420 nm and is seen in both the experimental and simulated spectra. The carbonyl bond absorption feature is clearly visible at 5.75 µm in the form of a trough. The quantity of PMMA present on the SRR results in significant absorption at 5.75 µm, caused by the electric field circulating the SRR being absorbed by the PMMA and resulting in a sharp spectral trough. This is particularly evident for measurements taken using TM polarisation, in which the strong, broad resonance at 5.25 µm is close to the carbonyl bond absorption wavelength.

It was found that introducing PMMA into the simulation model created unnatural artefacts below 4 µm wavelength that distorted the reflection spectra. For this reason experimental focus is given for the range 3 µm to 7 µm while simulated spectra are shown between 4 µm and 7 µm.
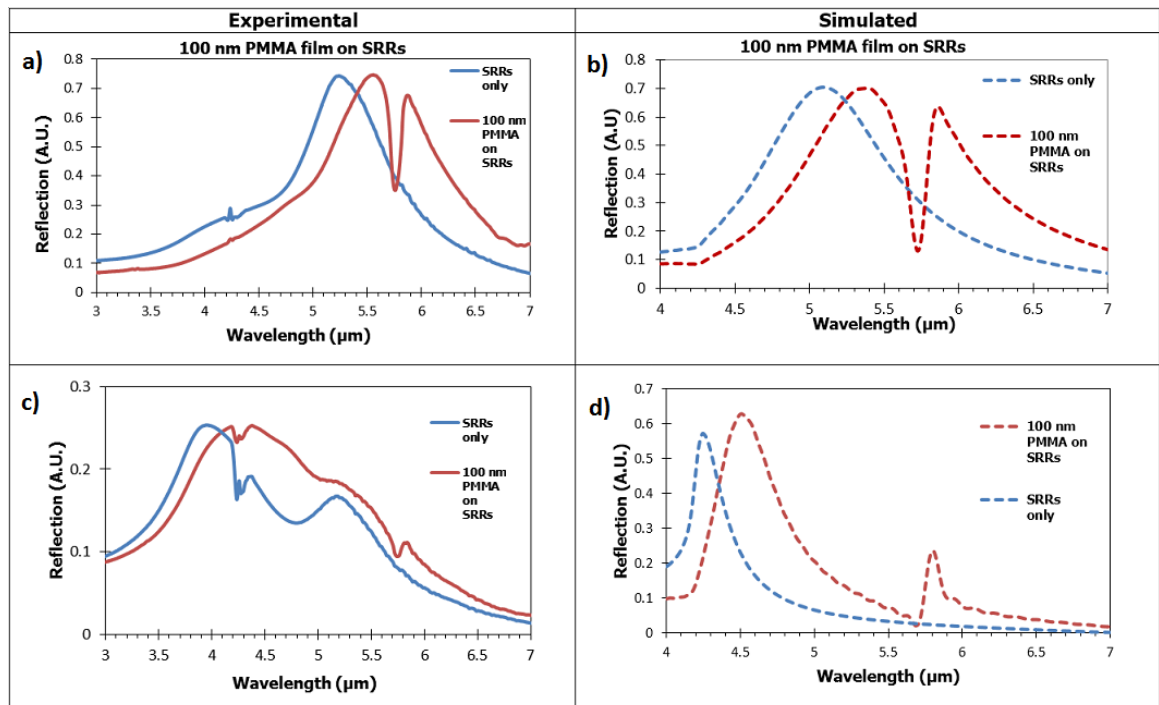
Figure 4.10: Reflection measurements (experimental and simulated) of the SRRs with (a) and (b) TM polarised light and (c) and (d) TE polarised light with a 100 nm film of PMMA on top.

With PMMA spun on top of the SRR array and a subsequent shift in resonance visible by optical measurement, the sensitivity of the SRRs can be calculated for a PMMA thickness of 100 nm. The sensitivity, denoted by s, is defined by the equation

$$s = \frac{\Delta\lambda}{\Delta n} \, nm/RIU$$

where $\Delta\lambda$ is the shift in the resonant wavelength of the SRR and Δn is the change in the refractive index. The sensitivity is quantified in terms of nanometers per Refractive Index Unit (nm/RIU).

The sensitivity of the SRR with a 100 nm film of PMMA spun on top can be quantified from the resonant wavelength shift seen in figure 4.10. For the experimental plasmonic resonance under TM conditions,

$$s = \frac{5560 - 5250}{1.49 - 1}$$

$$s = 632.65 \, nm/RIU$$

With a TE mode incident upon the SRRs, the resonant shift in wavelength is measured as 4330 nm – 3950 nm = 380 nm, giving a sensitivity of 775.51 nm/RIU. This sensitivity value of 775 nm/RIU compares favourably to that of values quoted for photonic crystal resonators used with microfluidics (s = 480 nm/RIU) [71] and polarisation independent, fourfold SRRs arranged in a symmetric pattern (s = 636 nm/RIU) [72]. It should be noted that the photonic crystal resonator cited above uses ethanol as an analyte while the fourfold SRR sensor utilises ZEP electron-beam resist. A-SRRs have been shown to experimentally exhibit sensitivities as high as 1230 nm/RIU using 215 nm thick PMMA as an analyte [60]. This enhancement can be attributed to the strength of the electric field present at the gaps of the asymmetric split ring structure as well as the increased quantity of analyte.

The sensitivity value obtained from the simulated spectra is found to be 612 nm/RIU for an incident TM mode and 551 nm/RIU for a TE incident mode.

With 100 nm of PMMA coating the SRRs, the electric field at near-field can be seen to exhibit a reduced magnitude in comparison to the field strength exhibited by the SRRs without any PMMA present. This is shown in figure 4.11. This decrease in strength is caused by the PMMA layer on top of the SRRs absorbing part of the electric field.
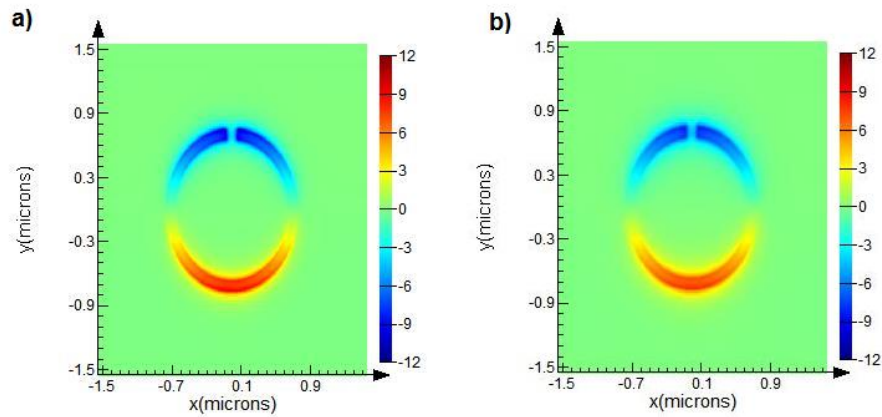
Figure 4.11: Electric field with TM incident mode with (a) just the SRR and (b) the SRR with a 100 nm PMMA film on top.

4.4.2 Localised PMMA (TM polarisation)

The results shown in this section study the SRR with localised PMMA with the electric field of the incident light orientated parallel to the y-axis, giving resonance at 5.25 µm. As the localised PMMA is significantly smaller in quantity, irrespective of its position, the shift in the SRR resonant wavelength will be less than the shift observed with a 100 nm PMMA coating. In all cases discussed henceforth the localised PMMA block is 150 nm by 150 nm with a thickness of 100 nm. Figure 4.12 shows the reflection spectrum obtained both experimentally and by simulation with the localised PMMA block positioned at the gap of the SRR. This will be termed this the primary hot-spot, owing to it being the location of the greatest electric field strength. A micrograph of the PMMA between the ends of the arc is shown inset.

The resonant wavelength of the SRRs is experimentally shown to shift to 5.32 µm with PMMA localised at the gap from the initial wavelength of 5.25 µm. This shift gives the SRR a sensitivity of 142.85 nm/RIU with the PMMA block localised at the gap.

$$s = \frac{5320 - 5250}{1.49 - 1} = 142.85 \; nm/RIU$$
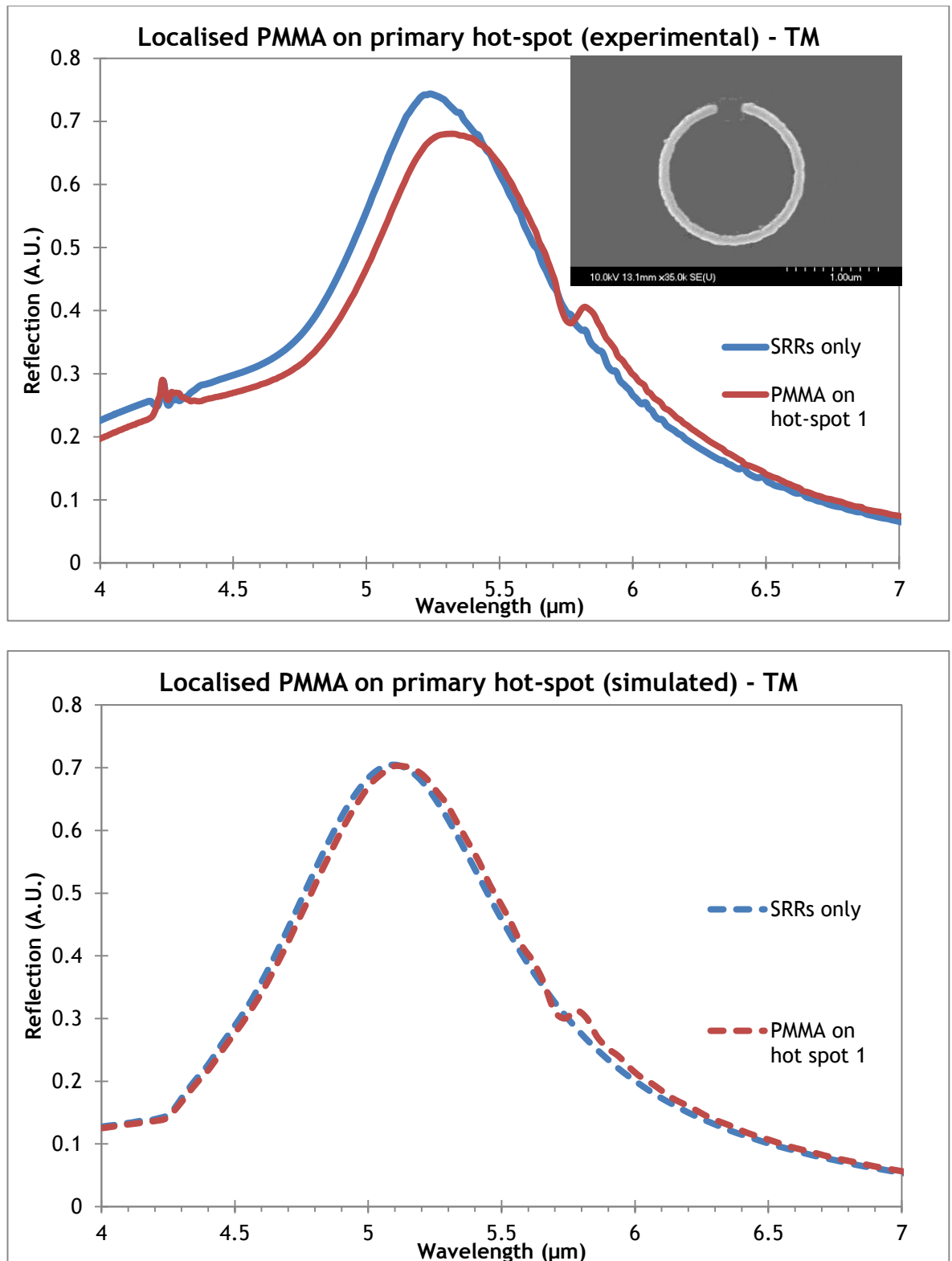
Figure 4.12: Reflection spectrum of the SRRs with PMMA localised at the gap (red) and of the SRRs without PMMA present (blue). Experimental spectra are shown top with simulated beneath. An image of the PMMA localised at the gap is inset.

From the simulation shown in figure 4.12 the shift in resonant wavelength is measured as 25 nm, giving a sensitivity value of 51.02. The absorption trough caused by the carbonyl bond is clearly visible at 5.75 µm in both the experimental and simulated spectra. However it is noted that the additional features of PMMA in the mid infra-red, listed in table 4.1, are not visible on either spectrum. Their presence is faintly visible in the experimental measurement of figure 4.10, in which the entire SRR array is coated with PMMA. This can be attributed to there being a much greater quantity of PMMA present and is why the absorption due to the carbonyl bond is so prominent in comparison to the localised PMMA block.

The calculated sensitivity of the SRRs with the PMMA is shown to substantially reduce with the PMMA localised at the gap of the SRR compared to a 100 nm thin film being deposited across the entire SRR array. This is despite the SRR gap being the optimal region for sensing due to the high electric field strength at both ends of the SRR arc [59].

The simulated electric field plots indicate a secondary hot spot at the bottom of the SRR, shown in figure 4.9. Reflection measurements of PMMA localised at this position (figure 4.13) show enhancement of the carbonyl bond at 5.75 µm, but very little shift in the resonant wavelength. The enhancement of the carbonyl bond is less pronounced as when the PMMA is localised in the gap of the SRR. The shift, $\Delta\lambda$, is found to be merely 10 nm for experimental measurements and 20 nm for simulated measurements. A sensitivity value of 20.41 is calculated for the experimental reflection and 40.81 for the simulated model. These factors indicate that despite there being a strong electric field at the bottom of the SRR arc and enhancement of the carbonyl bond absorption, the secondary hot-spot does not possess the same qualities desired for sensing as the primary hot-spot. This can perhaps be explained by the analyte, in this instance PMMA, having to reside on top of the metal SRR structure whereas it is placed on the substrate between the arc of the structure at the primary hot-spot. It should be remembered that the PMMA in all instances is spun to a thickness of 100 nm and the SRRs are comprised of 10 nm Ti and 100 nm Au.
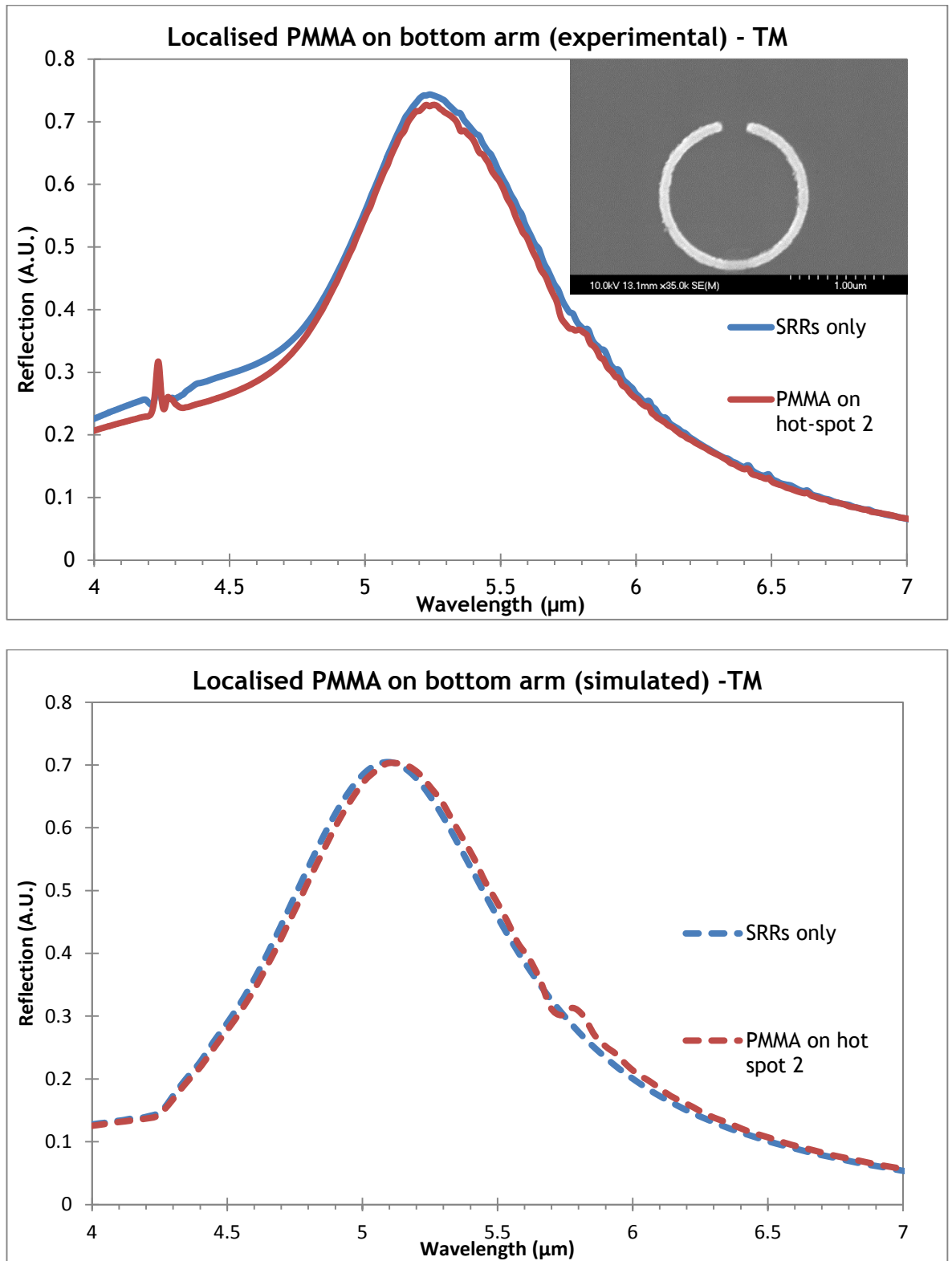
Figure 4.13: Reflection spectrum of the SRRs with PMMA localised on the bottom portion of the arc (red) and of the SRRs without PMMA present (blue). Experimental spectra are shown top with simulated beneath. An image of the localised PMMA is inset.

To help gauge the effect of placing the PMMA at a hot-spot on top of the metal rather than within the SRR gap, a PMMA block was localised on one of the ends of the metal arc. The resultant reflection spectra and SEM micrograph can be seen in figure 4.14. Simulations of this configuration were not performed.
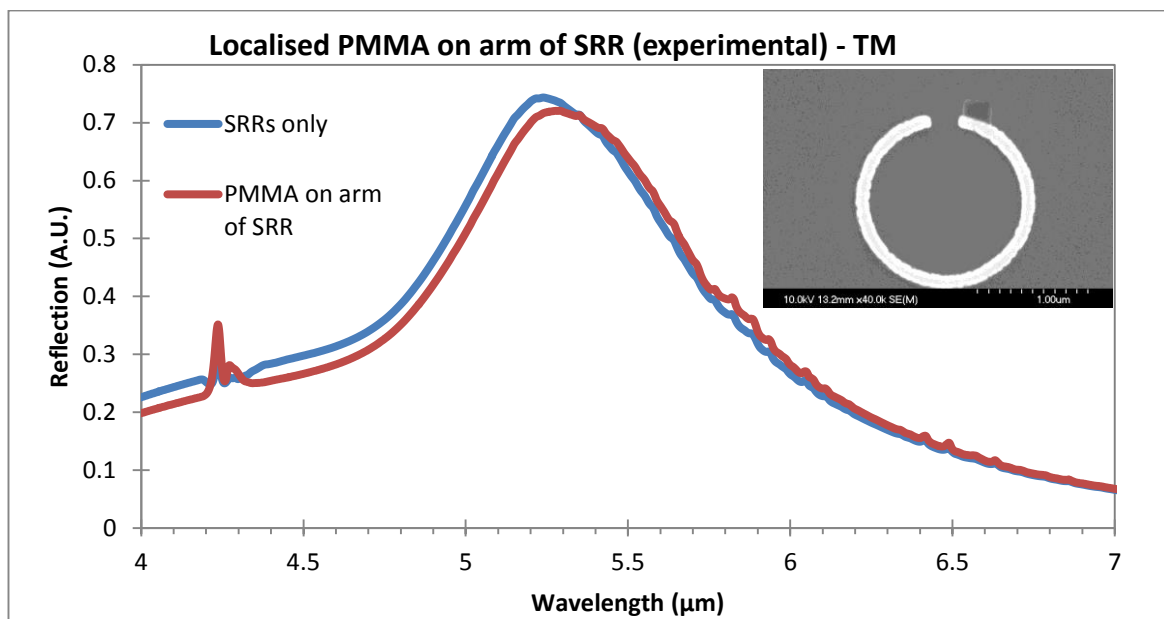
Figure 4.14: Reflection spectrum of the SRRs with PMMA localised on the end of the arc (red) and of the SRRs without PMMA present (blue).

An 80 nm shift in the resonant wavelength is observed experimentally. This gives a sensitivity of 163.27 nm/RIU, higher than observed for the secondary hot-spot but lower than when the PMMA is placed at the gap. The carbonyl bond absorbance at 5.75 µm is barely enhanced in comparison to when placed at the other two hot-spots. It is noted from the image taken by SEM however that approximately 50% of the PMMA block is located off of the metal and is instead on the fused quartz substrate.

Cold-spots, by definition, are areas on or near the SRR in which the electric field activity is at a minimum or even non-existent. At these regions enhancement of the organic compound's spectroscopic features cannot occur as there is no electromagnetic interaction between the SRR and the analyte. Consequently the resultant reflection spectrum fails to detect the small quantity of PMMA present, exhibiting no shift or enhancement of a particular molecule

Figure 4.15 shows the reflection spectra obtained with the PMMA block localised on the right cold-spot of the SRR (at 90° to the "y axis"). In this instance there is no discernible influence on the spectrum from that of the SRRs without PMMA present. As there is neither enhancement of the carbonyl bond feature nor, importantly, any shift in the wavelength of resonance, the sensitivity of the SRR

with PMMA localised to this cold-spot position can be said to be nil. This was found to be the case for both experimental and simulated results.
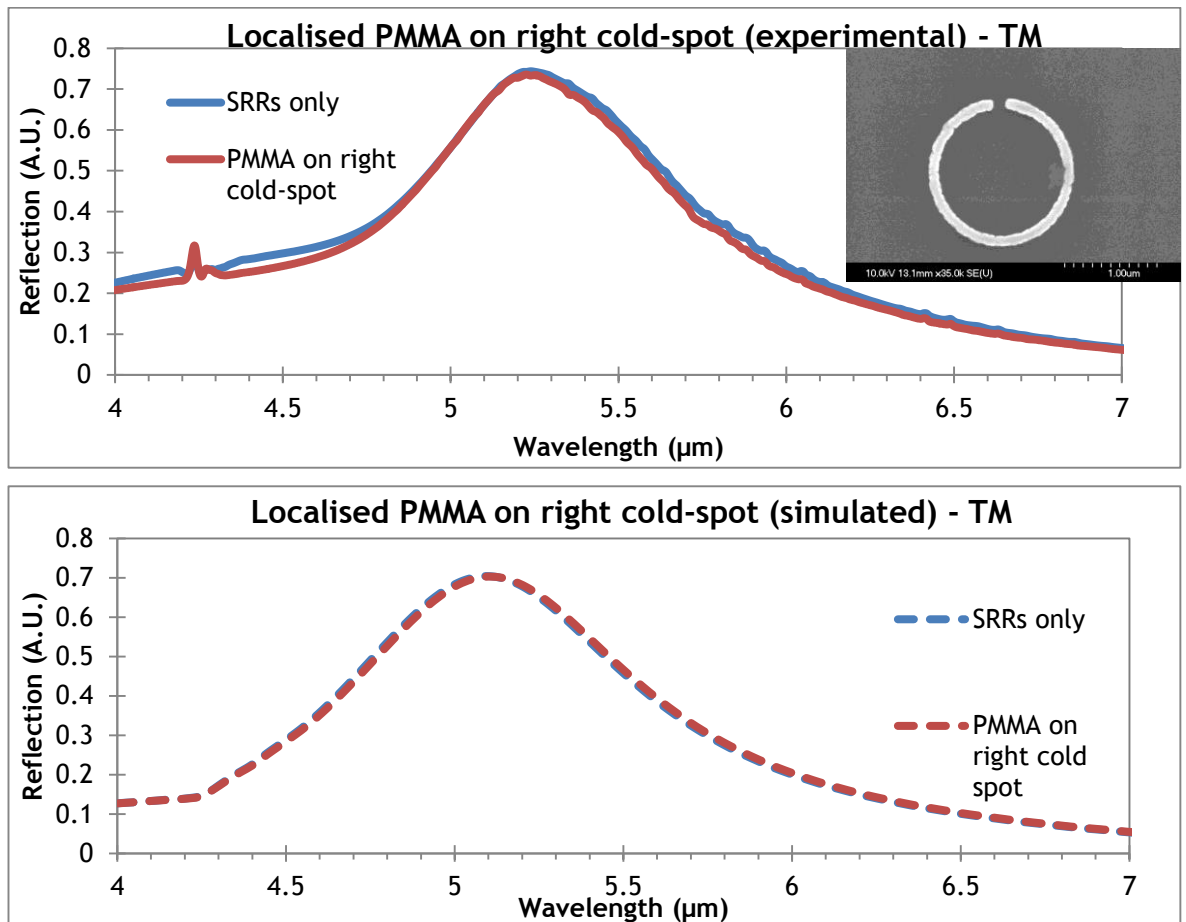
Figure 4.15: Reflection spectrum of the SRRs with PMMA localised on the "on-arc" cold-spot (red). SRRs without PMMA are shown in blue. Experimental spectra are shown top with simulated beneath. An image of the localised PMMA is inset.

Positioning the PMMA in the centre of the SRR, a region identified from field plots as exhibiting a very weak electric field, was found to give a similar reflection spectrum, with no resonance shift and very little enhancement, as displayed in figure 4.16.
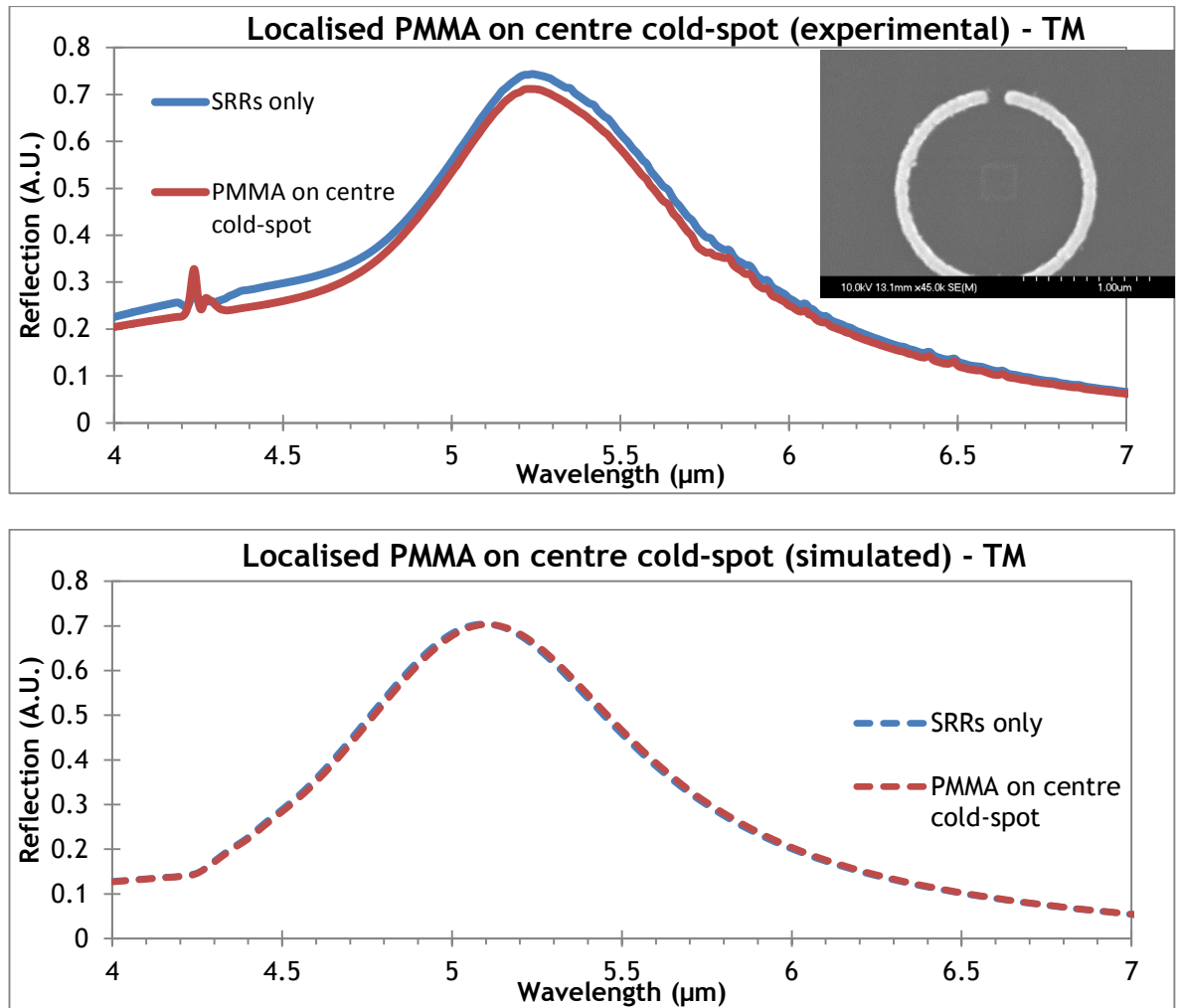
Figure 4.16: Reflection spectrum of the SRRs with PMMA localised in the centre of the SRR (red) and SRRs without PMMA (blue). Experimental spectra are shown top with simulated beneath. An image of the localised PMMA is inset.

4.4.3 Localised PMMA (TE polarisation)

The results shown in this section all show the response of the SRR with localised PMMA when the electric-field is orientated across the gap of the structure, parallel to the x-axis. Field plots of this configuration (figure 4.9) show that the electric field is strongest immediately at the split in the ring resonator.
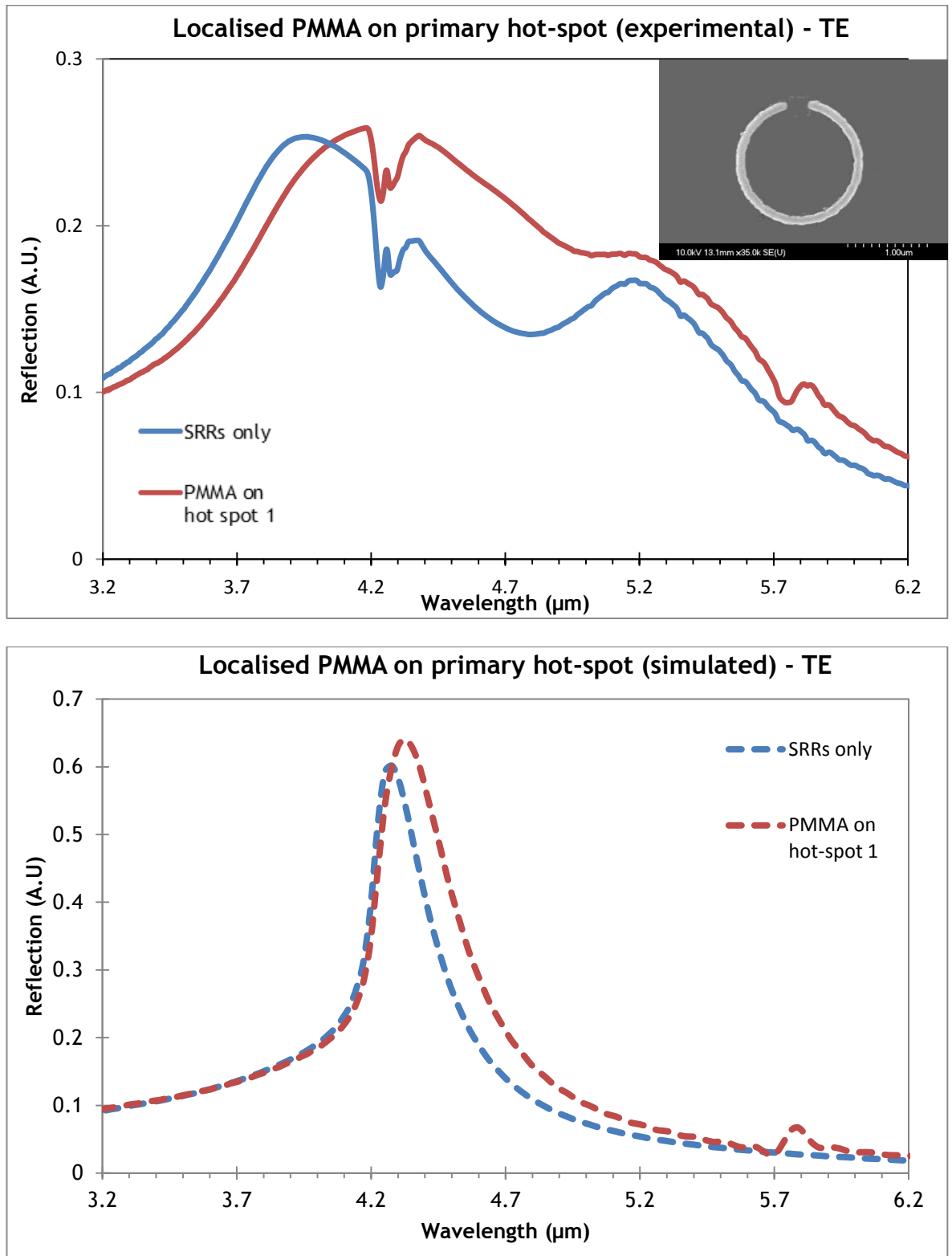
Figure 4.17: Reflection spectra of the SRRs under TE polarisation, with PMMA localised in the gap of the SRR (red) and SRRs without PMMA (blue). An image of the localised PMMA is inset.

With the PMMA block positioned within the gap of the SRR, the sensitivity is experimentally calculated to be 612.24 nm/RIU. This compares to 183.67 nm/RIU for PMMA in the same position but with TM polarised incident light. Measurements of SRRs with PMMA localised on the bottom arm of the structure (six o'clock

position) are shown in figure 4.18. Under this configuration there is no shift in the resonant wavelength or enhancement of the carbonyl bond absorption feature for either experimental or simulated spectra. This was also found to be the case when PMMA was localised in the centre of the SRR, also shown in figure 4.18. The lack of close proximity to an area of high electric field, identified in the field plots, can account for this.
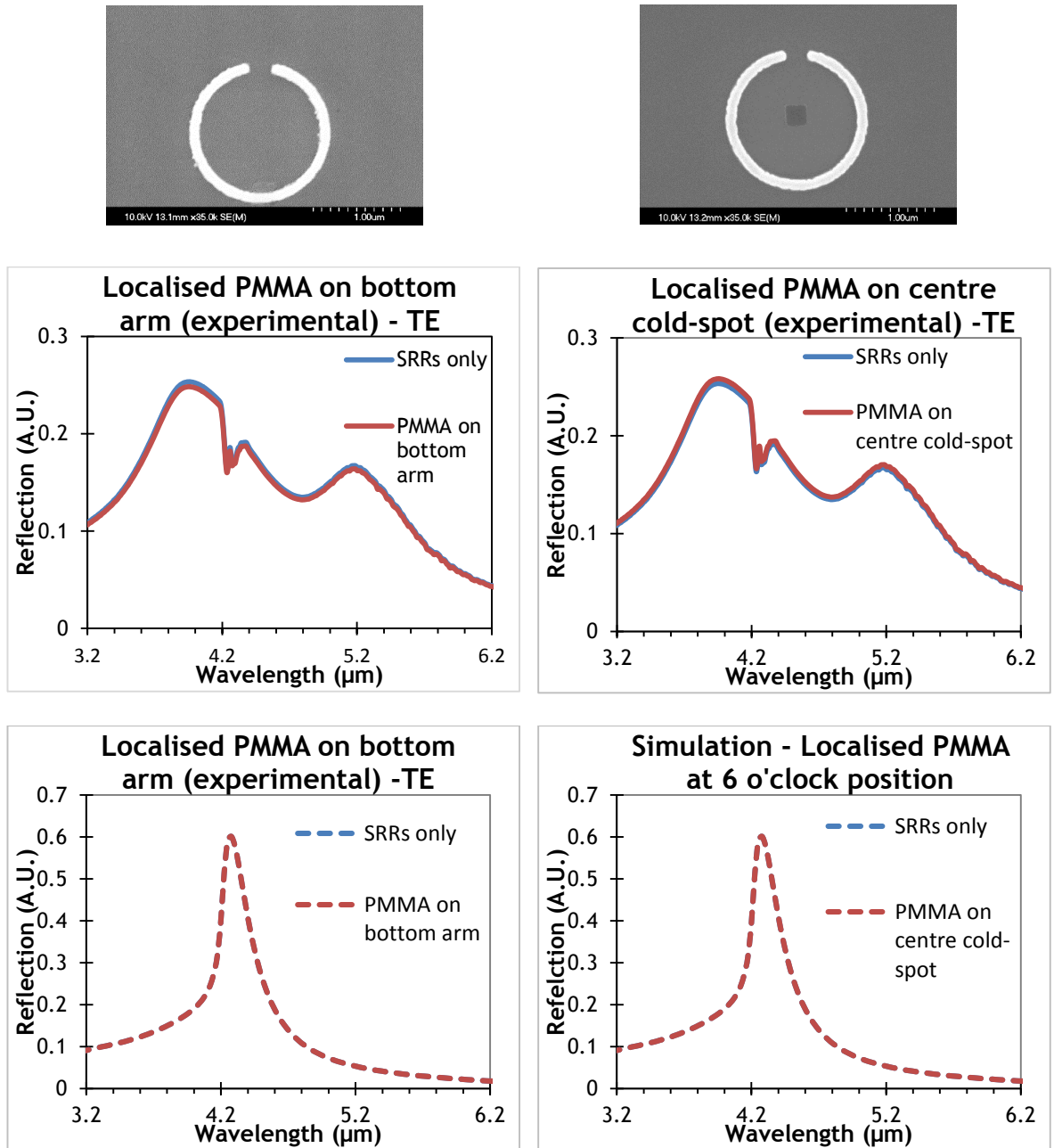
Figure 4.18: Experimental and simulated reflection spectra for PMMA localised at the bottom of the SRR (6 o'clock position)(left) and at the centre cold-spot (right).

Reflection spectra with PMMA localised at the three o'clock position on the SRR are shown in figure 4.19. Unlike the spectra obtained with PMMA positioned in the centre cold-spot and at the bottom of the split-ring, a small shift in the resonant wavelength of 160 nm is exhibited experimentally. An experimental sensitivity of 326.53 nm/RIU is calculated in this instance. This PMMA position has been termed a "hot-spot" at the resonant wavelength shown.
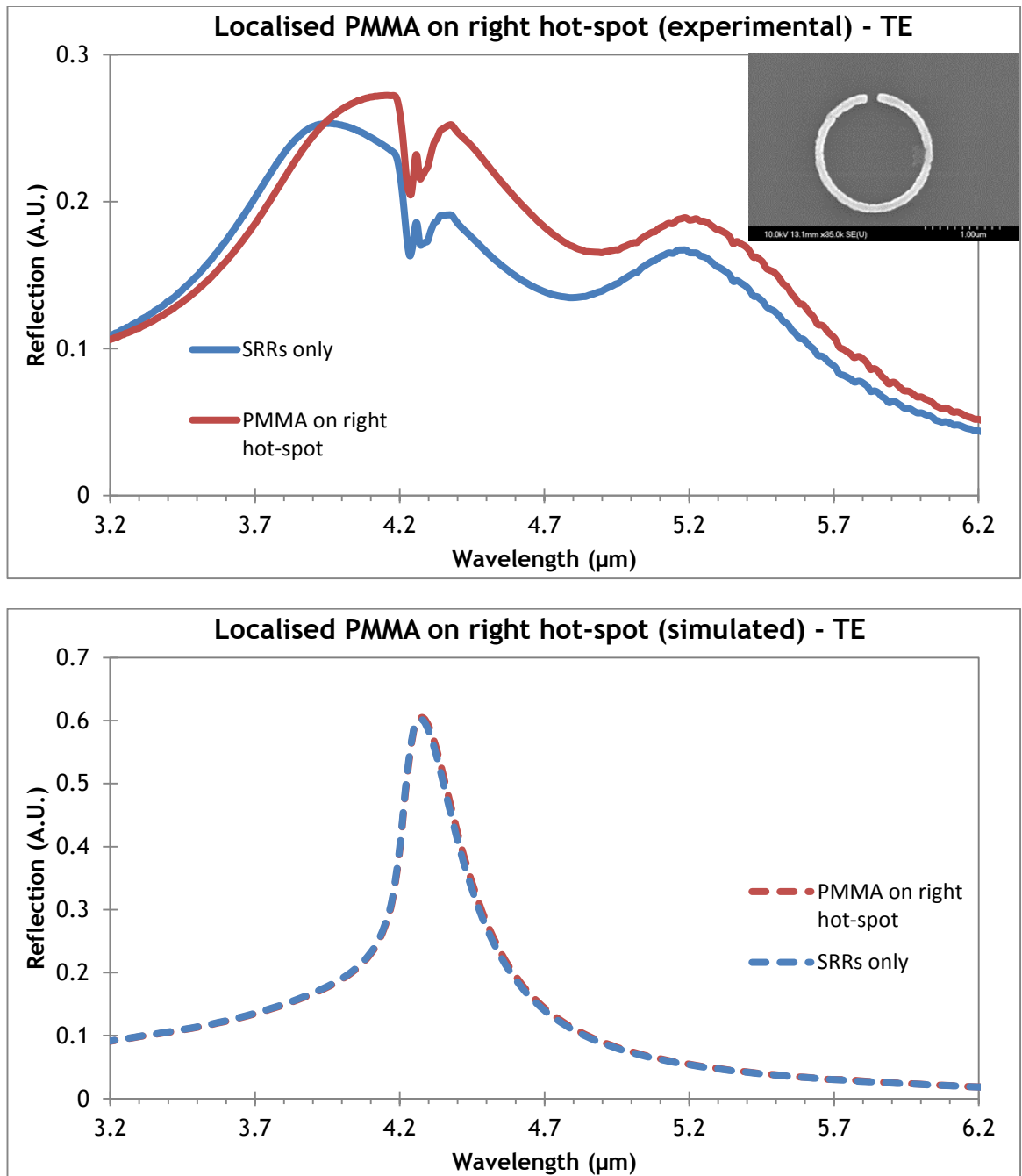
Figure 4.19: Experimental and simulated spectra with PMMA located at the three o'clock position on the SRR with a TE incident mode.

As with measurements taken using TM polarisation, the SRR was found to be sensitive to the presence of PMMA located at the end of the arm of the structure when a TE polarised mode was incident (figure 4.20). As with figure 4.14, simulations were not performed for this configuration.
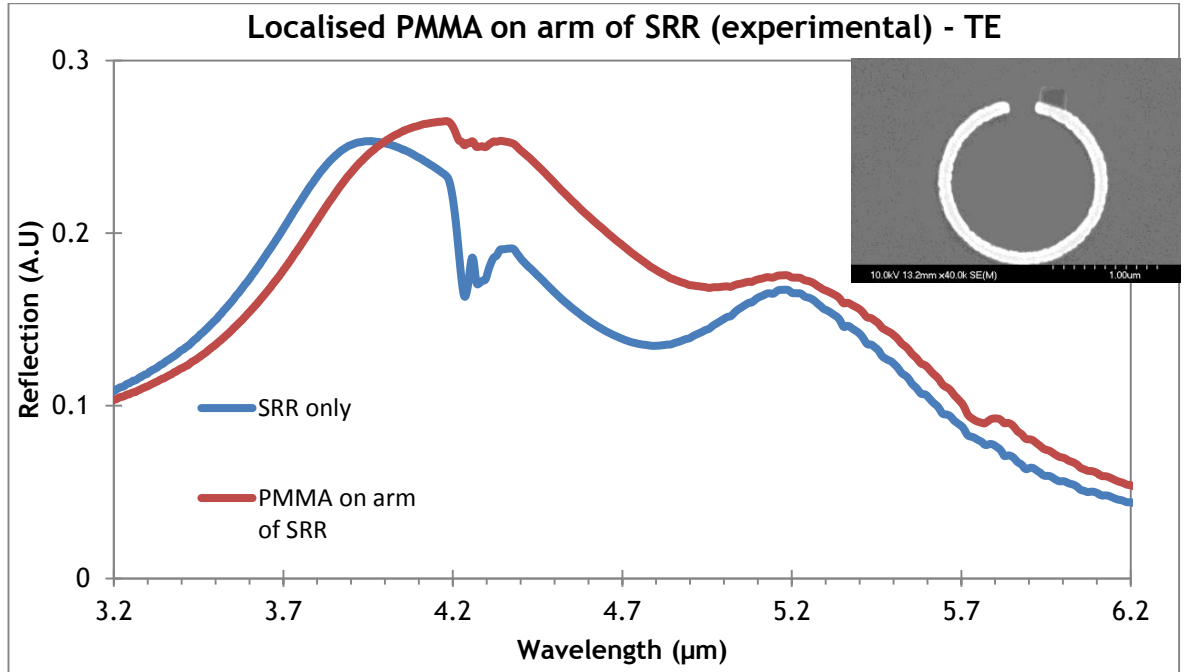
Figure 4.20: Experimental spectrum of SRRs with PMMA positioned at the end of the metal arm, under TE polarisation.
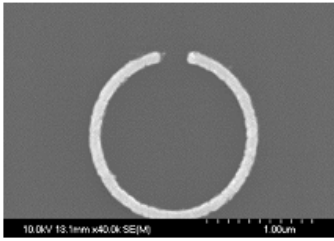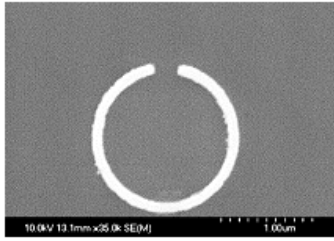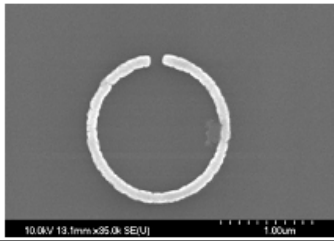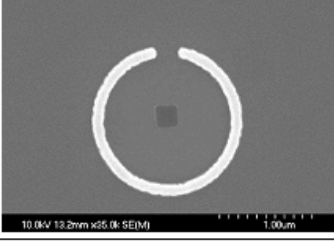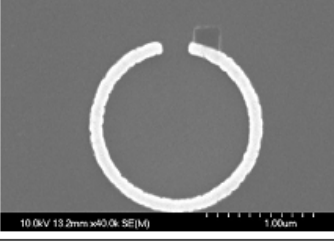
A resonant peak wavelength shift of 190 nm was measured with PMMA present on the arm of the SRR. This produces a sensitivity of 387.76 nm/RIU.

4.4.4 Comparison of regions of sensitivity

The shifts in the resonant wavelength and resultant sensitivity values obtained by experimental and simulated methods are compiled in table 4.2. Unsurprisingly the greatest sensitivity is obtained when the SRR array is covered in a 100 nm thin film of PMMA and the electric field of the incident light is orientated across the gap of the SRR (s = 775.51 nm/RIU). However experimentally determining the areas of the SRR unit cell that offer the greatest sensitivity can only be found by probing confined regions with the PMMA analyte. In doing this, the gap between both ends of the arc is shown to be the most sensitive region of the SRR, with s = 612.24 nm/RIU. This is despite the localised PMMA accounting for approximately 2.34% the volume of the thin PMMA film that coats the SRR array. The secondary hot-spot, positioned on the arc beneath the gap, was found not to

shift the wavelength of resonance, although enhancement of the spectral absorption feature at 5.75 μm is observed under TM conditions. Placing the PMMA on the gold arc at the gap offers a shift in resonance and a maximum sensitivity of 387.78 nm/RIU, below that calculated for PMMA in the gap region.

The values obtained from SRRs covered with a 100 nm film of PMMA can be compared with similar (but not identical) experimental work involving both symmetric and asymmetric double split ring resonators [45,60]. In this work, Lahiri et al fabricate circular, symmetric SRRs with two gaps (and not one, as here) and gradually introduce greater asymmetry in the structures by changing the length of one of the two arcs. A 100 nm thin film of PMMA is then applied. For the symmetrical structure a wavelength shift of 340 nm is reported (s = 694 nm/RIU) while the asymmetric structure exhibits a shift of 510 nm (s = 1041 nm/RIU). In these experiments the electric field was orientated parallel to the y-axis, equivalent to the results obtained in this chapter using TM polarisation in which the sensitivity is calculated as 633 nm/RIU for a 100 nm film of PMMA. This suggests that A-SRRs can offer an enhanced sensitivity to PMMA than single split, symmetrical SRRs.

PMMA position	Sensitivity (s) (nm/RIU)	
	Experimental	Simulated
Coating SRRs	TM - 633 TE - 776	TM - 612 TE - 551
Primary hot-spot (gap)	TM - 143 TE - 612	TM - 51 TE - 163
Bottom arm (6 o'clock)	TM - 20 TE - 0	TM - 41 TE - 0
Right hot/cold spot (3 o'clock)	TM - 0 TE - 327	TM - 0 TE - 20
Centre cold-spot	TM - 0 TE - 0	TM - 0 TE - 0
On arm at gap	TM - 163 TE - 388	TM - N/A TE - N/A

Table 4.2: Calculated sensitivity for each of the hot-spots identified and for SRRs coated in 100 nm PMMA using experimental and simulated measurements.

4.5 Chapter Conclusions

The work in this chapter has experimentally probed single-gap SRRS using localised PMMA and experimentally identified regions at which the electromagnetic sensitivity of the resonator is most prominent; the areas termed "hot-spots". Experimental measurements have been verified with reflection measurements from simulated models, although further work is required in improving the agreement between experimental and simulated characterisation of the plasmonic resonance near 4 μm and sensitivity to PMMA. A change in the geometry of the SRR would enable plasmonic resonances to be shifted to other wavelengths, enabling better "tuning" to the carbonyl absorption feature at 5.75 μm. Enhancement of the carbonyl bond feature exhibited in PMMA was found to be strongest at the gap of the SRR and, to a lesser extent, at the end of the resonator arm. These regions produced the highest sensitivity of the analyte. Conversely, regions of the SRR where there is no enhancement or sensing of the PMMA were also identified. These "cold-spots" reside at areas of the structure where no electric field is present. Measurement and simulation over a broad wavelength range has shown multiple plasmonic resonances exist within the SRR structure. Experimental characterisation has shown that the sensitivity of the SRR is maximised when the incident electric field is orientated parallel to (across) the gap in the structure.

Suggestions for future research and improvements in regard to the work detailed in this chapter can be found in chapter 7.

Acknowledgement

Chapter 5

Nanoimprinted fishnets with nano-pillars
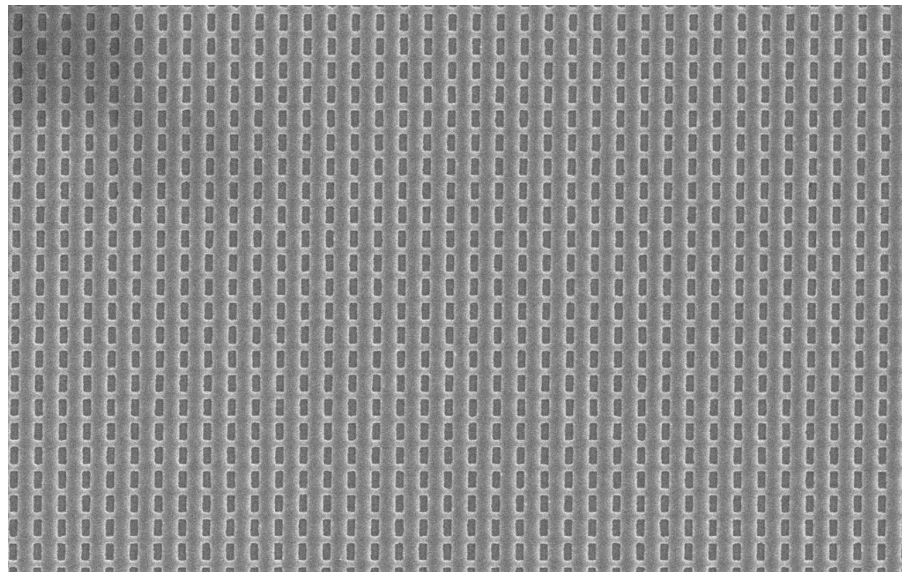
5.1 Introduction

First fully envisaged in 2005 [73] and experimentally realised a year later [74,75,76], the fishnet structure is perhaps the most commonly cited metamaterial exhibiting a negative refractive index. The name fishnet is derived from the structure's resemblance to a fishing net. Much research has gone into improving the optical performance of fishnets, with work undertaken in shifting the resonant wavelength (and negative index wavelength range) to the visible regime [77-79] and increasing the magnitude of the negative index [80-82]. Many applications have been proposed for negative-index metamaterials, such as imaging below the diffraction limit, Pendry's "superlens" and enhanced antennae [83,84], but progress in realising many of these uses has been slow. This is in part because present metamaterials often operate at wavelengths far from where they could be deemed useful for application or may only function at a narrow wavelength range. Further to this, most metamaterials constructed for research purposes are fabricated using EBL which, as established in chapter 1, is a time consuming and costly lithographic technique.

As previously discussed, nanoimprint lithography offers certain advantages over conventional electron-beam lithography. These advantages include large pattern areas, a shortened patterning time and reduced fabrication costs, all of which can contribute to moving metamaterials from a research environment towards practical applications. As well as the commercial benefits outlined above, the work detailed in chapter 3 shows that engineering and fabrication advantages also exist. These can have benefits in terms of the behaviour (optical, electrical or other) of materials.

In continuation of the work in chapter 2 involving nanoimprint lithography to fabricate metamaterials, this chapter will demonstrate the ability to imprint directly into pre-deposited metal and dielectric layers to produce negative-index fishnets. These fishnet structures are estimated to exhibit optical characteristics comparable to those fabricated by conventional means. Furthermore plasmonic responses from nano-pillars, an artefact of the NIL process, are found at visible wavelengths. Comparison of experimental measurements show that the structures are non-reciprocal, resulting in certain features only being detected from either a reflection or a transmission measurement but not both. This potentially useful

feature could be used to enhance resonances of organic materials at different NIR wavelengths using a single metamaterial structure and measure them independently of each other.

5.1.1 The metamaterial fishnet

The metamaterial fishnet can best be physically described as an array of perpendicularly interlocking thin metal wires and tracks that are stacked on top of a dielectric layer that separates them from another set of parallel metal wires and tracks. An illustration is shown in figure 5.1. Typically, the metal tracks are larger in dimension to the narrower metal wires that run perpendicularly to them. The parallel tracks and parallel wires are separated by an array of holes, or apertures. A single active layer fishnet is composed of a tri-layer of metal, dielectric and metal. Additional subsequent layers of dielectric and metal can be stacked onto a single active layer to make it a "3D metamaterial", i.e. one that exhibits multiple resonances in the x, y and z axes.
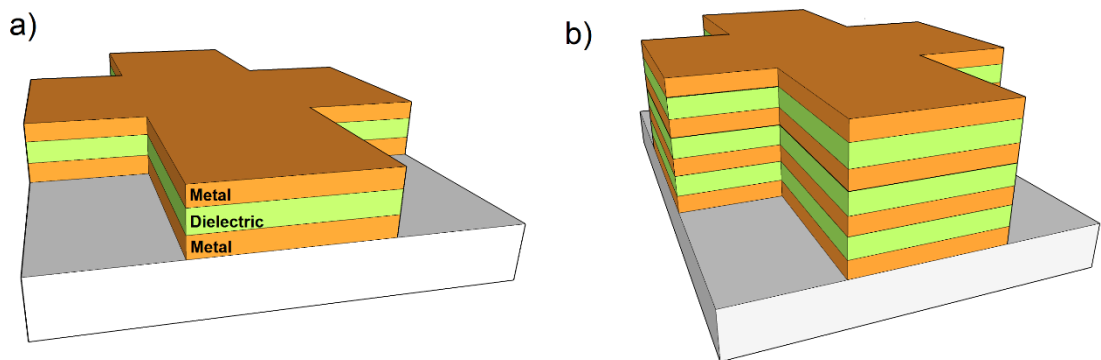
Figure 5.1: The metamaterial fishnet. (a) a single active layer fishnet unit cell and (b) a unit cell of a 3D fishnet with 3 active layers.

For an optimal optical response, the wide tracks of the fishnet are aligned parallel to the magnetic field vector of the incident EM wave and the narrower metal wires are orientated in the same direction as the respective electric field. This configuration allows for the creation of anti-symmetric currents in the metal tracks. The presence of a dielectric layer between the metal layers of the tracks enables the structure to act as an inductor and capacitor resonator, with a current loop flowing around the metal tracks (inductor) and dielectric (capacitor). This concept is shown in figure 5.2. Varying the dimensions of the metal-dielectric-metal tracks, such as their width and the thickness of the dielectric gap, changes

the L and C component of the structure and, consequently, the resonant wavelength. At and near resonance, the magnetic response of these tracks enables a permeability negative in value to be achieved. The thinner metal wires that run parallel to the electric field component of the incident light act as a diluted metal with a comparably lower plasma frequency. This is in part because the free electrons are restricted by the physical dimensions of the metal wires, unlike in a bulk metal. The concept of "effective electron mass" should also be considered when discussing a decrease in the effective plasma frequency. As a consequence of Lenz's law, the inductance of the metal wires acts to counter the rate of change in the current present. This results in the electrons in the metal wire behaving as if they had gained a significant amount of mass. An increase in the effective mass of the electrons reduces the effective plasma frequency, as equation 5.1 demonstrates.

$$\omega_p^2 = \frac{n_e e^2}{\varepsilon_0 m} \qquad\qquad\qquad\qquad (5.1)$$

The plasma frequency is represented by ω_p, n_e is the number density of electrons, e is the electric charge, ε_0 is the permittivity of free space and m is the effective mass of an electron.

With the metal wires of the fishnet structure behaving as a diluted metal with a reduced plasma frequency, the effective permeability can be engineered to have a negative value. As two separate components of the structure are responsible for determining the permeability and permittivity, the values of μ and ε can be varied independently of one another by altering the physical dimensions of either the tracks or wires [81,85]. If both the permeability and permittivity are negative at the same wavelength range, the structure can be considered as a "double negative" metamaterial with a negative refractive index. In this instance a negative refractive index will likely be greater in magnitude than a fishnet with only the permeability or permittivity negative in value. It should be noted from chapter 1 that metals often exhibit a negative permittivity without any specific structural arrangement or classification as a metamaterial.
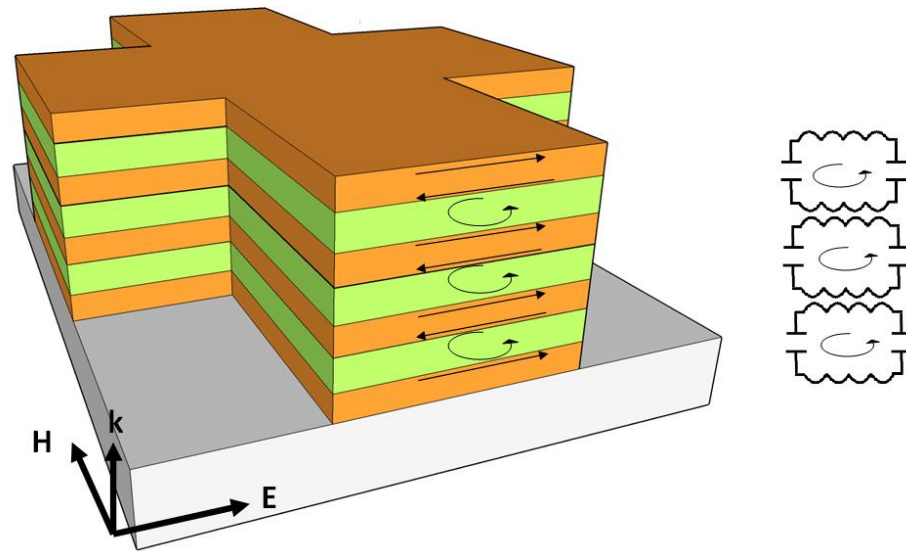
Figure 5.2: A cross sectional profile of a metal-dielectric-metal track showing the current flow induced by an incident EM wave. An equivalent LC circuit of the structure is also shown.

5.1.2 3D bulk fishnets

3D bulk fishnets offer significant advantages over single active layer fishnets. A bulk metamaterial can be considered as one in which the material properties converge to certain bulk properties when the structure is replicated on a given axis [80]. For example stacking multiple layers of metal and dielectric onto a fishnet pattern may result in coupling between each active layer. The extent of the coupling can depend on the gap between each metal layer (i.e. the thickness of the dielectric), the amount of asymmetry in the fishnet structure and of course the constituent material properties [86, 87]. If the dielectric is too thick, the interaction between the metal layers will be weak, resulting in limited enhancement of the material properties. However if the capacitive gap between each metal layer is optimised and sufficiently thin, coupling will be much stronger and produce lower losses, an increase in the magnitude of n and the FOM as well as a larger negative wavelength range [80]. The transmittance of a fishnet can also be increased by means of what is termed "extraordinary optical transmission" (EOT). This concept was first described in Ebbesen's 1998 paper [88] which studied the transmission of light through periodic, sub-wavelength hole arrays in silver – a structure not unlike the metamaterial fishnet [89]. EOT can exhibit an enhancement in transmitted light due to the incident wave coupling to and exciting the surface plasmons present at the interface between a metal and insulator. In the case of the fishnet structures studied in this chapter, these

interfaces are between silver and air, silver and MgF_2 and silver and PMMA. If the metal layer is sufficiently thin with regard to the incident wave, surface plasmons on both interfaces of the metal layer can couple to one another, hereby enabling the transmission of light. The current flow within each active layer of a fishnet can also contribute to an increase in optical transmission. As the current at each successive metal-dielectric interface is anti-symmetric (figure 5.2), it has been demonstrated that the consequent destructive interference reduces the internal losses and enhances overall transmission [80]. All of these factors result in significant advantages in stacking multiple metal-dielectric layers and converting a single-active layer fishnet into a 3D bulk fishnet with enhanced properties.

From a practical perspective fishnets are fabricated on top of a supporting substrate. This substrate, often but in no way limited to silicon or glass [78-80,90,91], can have a profound effect on the properties and response of the metamaterial. The substrate, often with a comparatively high refractive index compared to air, reduces the plasmonic coupling across the dielectric gap and consequently the magnetic resonance and material properties. It has however been shown that increasing the number of active layers in a fishnet can reduce the effect of the substrate [92]. By changing from a single active layer fishnet on a substrate to a substantial 3D bulk fishnet on a substrate the effective index has been shown to broaden from a modest negative trough to a wider negative region with n values greater in magnitude [80]. Furthermore, the negative index region can be seen to shift to shorter wavelengths as the number of active layers increases, up until the point of saturation when additional layers no longer improve the metamaterial properties. This shift and improvement in the magnitude of n can be attributed to the fact that with an increase in active layers, the currents induced by the plasmons at metal-dielectric interfaces are physically far removed from the substrate, reducing its effect. It is worth noting that it is not uncommon for theoretical papers that study fishnets not to consider the presence or influence of a substrate [93,94].

Increased symmetry between each active layer helps produce greater coupling while asymmetry, where layers are physically offset or different to each other, weakens any coupling between active layers. The asymmetry introduced by the presence of a substrate and angled sidewalls can introduce bi-anisotropic effects,

in which different reflectivities are produced when measuring at normal incidence the top and the bottom face of the sample. Furthermore, asymmetry in a fishnet structure can result in the rotation of incident polarisation. In this scenario, localised surface plasmons (LSPs) rotate around the apertures of the structure, generating "spinning" LSP modes [95]. As a result, the magnetic field of the incident wave causes electrical polarisation and the electrical field induces magnetic polarisation, a phenomena known as the magnetoelectric effect. Bi-anisotropic effects can reduce the effective material properties and therefore it is best to consider the structural design and fabrication technique before construction of the fishnet.

5.1.3 Common fabrication techniques

Although a variety of fabrication techniques have been successfully used to create metamaterial fishnets there are perhaps two methods most commonly adopted. The first is EBL of a removable mask with subsequent metal and dielectric deposition and lift-off [78]. The second is focused ion beam (FIB) milling of a material stack [80]. Both have numerous advantages and disadvantages that are detailed in table 5.1. The primary disadvantage for both techniques is that they are slow and generally limit the area of which a pattern can feasibly be produced. FIB milling involves sequentially removing the alternating layers of metal and dielectric to define the fishnet pattern. This is not only a time consuming process but it also has the added disadvantage of producing tapered sidewalls in the metal-dielectric material stack and re-deposition of the milled material. This often sizeable asymmetry can be a source of bi-anisotropy and hamper the fishnets effectiveness.

	Advantages	Disadvantages
Electron-beam lithography	• High structural resolution • Small minimum feature size	• Time consuming • Limited pattern area • Expensive • Material can fail to lift-off and can "flag".
Focused ion beam milling	• Well suited for a stack of multiple materials. • Small minimum feature size • High spacial precision	• Time consuming • Limited pattern area • Angled sidewalls introduce asymmetry. • Re-deposition of milled material

Table 5.1: Advantages and disadvantages of EBL and FIB milling in fabricating fishnet structures.

Other than EBL and FIB, more novel techniques have been shown to be successful in creating fishnets. A number of studies have investigated the use of nano-imprint lithography (NIL) as a technique in fabricating fishnet [90, 95-98] and similar shaped metallic nano-hole arrays [99-101]. An adapted nanoimprint technique, termed "inking", is of particular interest in the production of large area fishnets. With inking, the metal and dielectric layers are deposited on top of a series of protruding tracks and wires on a stamp before being detached for application elsewhere [98]. This latter technique in particular offers numerous benefits such as large pattern areas, re-usable stamps and detachable, movable fishnets that can be applied to another substrate or suspended in air. However, it also has the disadvantage of requiring lengthy cleaning of the stamp before it can be reused.

5.1.4 Potential sensing applications

Despite primarily being cited for their potential as a negative index metamaterial (NIM), work has also been reported on applying the fishnet structure, or similar variants, to sensing. This includes sensing gas molecules or analyte particles by means of absorption in an organic layer of a fishnet, hence changing the dielectric properties and producing an altered transmission spectrum [102-104]. The fabrication of fishnet operating at terahertz frequencies on a flexible polydimethylsiloxane (PDMS) substrate has also been suggested for use in sensing with microfluidics [105].

5.2 Fabrication

The fabrication of the fishnet and nano-pillar structures was achieved using nano-imprint lithography and a graphic illustrating this process is shown in figure 5.3. Previous studies have demonstrated the use of NIL or similar variants in patterning a mask for the subsequent deposition or etching of the metal and dielectric layers [90,98]. However the technique outlined in this chapter offers what can reasonably be described as a simpler and equally effective fabrication method, detailed below.

1. A cleaved silicon carbide (SiC) stamp is cleaned and spun with hydrogen silsequioxane (HSQ).

2. Rectangular pillars are exposed in the HSQ by EBL and developed using tetramethylammonium hydroxide (TMAH).

3. The patterned HSQ is given a post-development hard-bake in a furnace at 650 ºC for 3 hours.

4. The SiC is etched, using the HSQ as a mask, using inductively coupled plasma (ICP). This leaves SiC pillars 1 μm in height. The remaining HSQ is removed using buffered hydrofluoric (HF) acid etch – see figure 5.5 (a).

5. The stamp is treated in a solution of heptane and F_{13}-OTCS ((Tridecafluoro-1,1,2,2-tetrahydrooctyl)-trichlorosilane) for 10 minutes and rinsed in RO water. This creates a non-stick, hydrophobic layer on the surface of the stamp.

6. To prepare the target sample, 1 μm of PMMA is spin coated onto a clean fused silica substrate and baked for 15 minutes at 90 ºC.

7. 30 nm of Ag, 50 nm of MgF_2 and another 30 nm Ag are sequentially deposited on top of the PMMA by thermal evaporation.

8. The SiC stamp is imprinted into the target sample using a Specac hydraulic press at room temperature and an imprint force of 1 tonne for 1 minute.

An idealised model of the imprinted fishnet with pillars, detailing dimensions measured experimentally for structures A and B, can be seen in figure 5.4. In addition to the advantages previously listed regarding NIL, imprinting directly into a metal-dielectric-metal stack was found to create vertical sidewalls in the fishnet apertures. Tapered sidewalls are often a remnant feature of focussed ion beam (FIB) milling of a material stack [80]. The asymmetry caused by the tapering introduces bi-anisotropic effects in the material, typified by exhibiting electric polarisation in response to a magnetic field and vice-versa [86]. As a direct consequence the magnitude of any negative refractive index can be inhibited. For this reason it is important that the etched SiC pillars on the stamp have lateral, non-tapered sidewalls, as tapering would be replicated in the imprinted sample and structural dimensions would be enlarged. With regard to achieving fishnets

with vertical sidewalls to limit bi-anisotropic effects, imprinting directly into the material stack offers a distinct advantage over FIB milling.
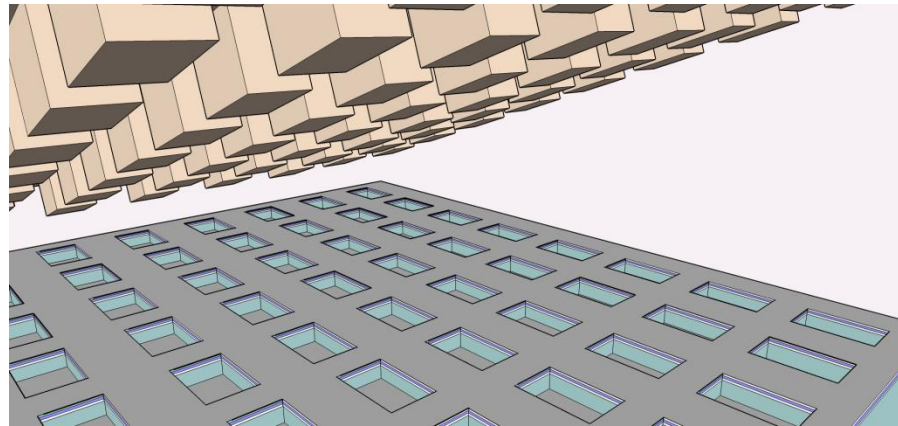
Figure 5.3: Graphic illustrating the direct nanoimprint process (not to scale).

Thermal NIL usually sees the stamp or target sample being heated to reduce the viscosity of the polymer that is to be patterned. However it was found that doing so with this fabrication technique caused aided the flow of the PMMA and caused nano cracks to appear in the metal and dielectric layers. Imprinting into the Ag and MgF$_2$ layers at room temperature prevented deformities of this kind arising.

Silver is used in preference to gold because of its negative permittivity and lower associated optical losses [106]. At optical wavelengths, silver exhibits the lowest damping of all metals [107]. This however introduces a finite lifetime for the structure, as an oxide layer is known to grow on silver when it exposed to normal atmospheric conditions. The imprinted pattern area for each of structures A, B and C is 3 mm^2. This compares well with fishnets exposed by conventional FIB or electron-beam methods, which are confined to much smaller areas, often in the order of hundreds of square microns. In addition to this the imprinting technique offers the ability to produce the structures at a reduced cost and time, with the potential of "step-and-repeat" imprinting conceivably increasing the patterned area further.

a)
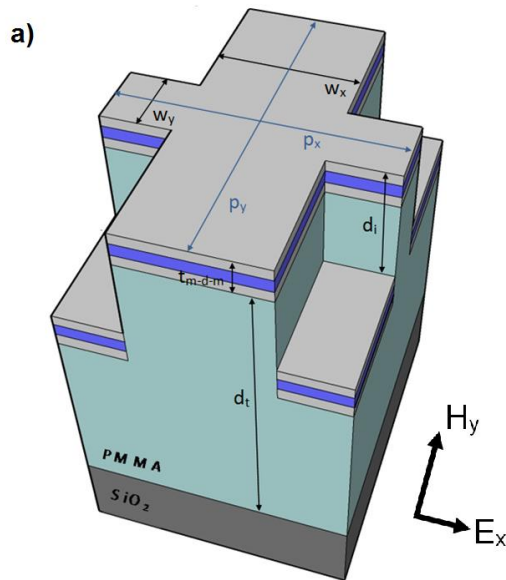
b)

Structure	p_x (nm)	p_y (nm)	w_x (nm)	w_y (nm)
A	640	640	410	220
B	860	870	590	280
C	1800	1750	1100	500

Figure 5.4: (a) Model (not to scale) of an ideal single unit cell of the fishnet with pillar structure after imprinting. Annotations are included for dimensions. The PMMA layer at its thickest, d_t, is 1000 nm. The imprinted depth of the pillars, d_i, is 300 nm for both designs A and B. The metal-dielectric-metal tri-layer of Ag, MgF_2 and Ag (t_{m-d-m}) totals 110 nm in thickness (30 nm Ag, 50 nm MgF_2, 30 nm Ag). Incident light for both reflection and transmission measurements is polarised as shown and denoted as TM (b) Table listing the measured dimensions from the fabricated samples for both structures.
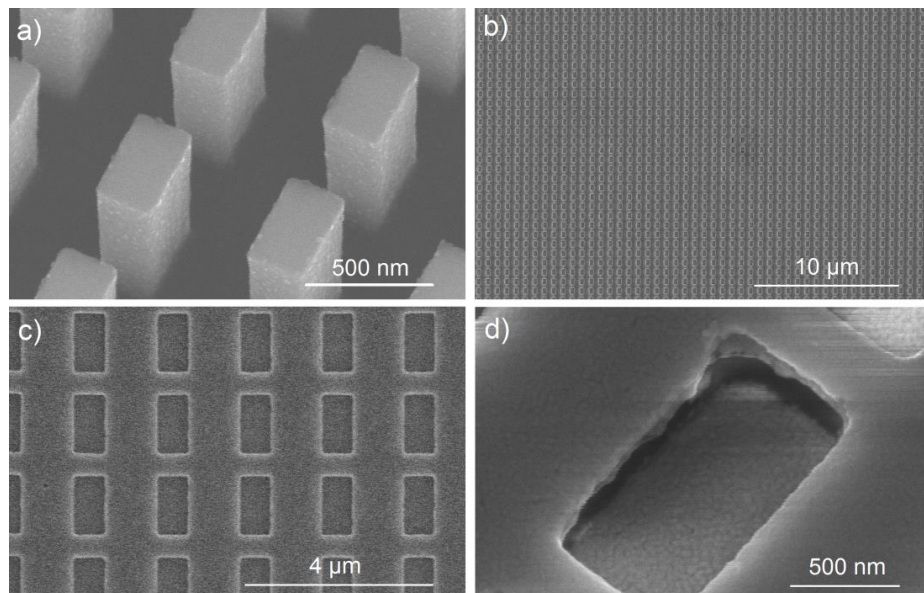
Figure 5.5: Micrographs of the nanoimprint stamp and fabricated structures taken by SEM. (a) Tilted profile of a SiC stamp showing etched pillars, (b) micrograph showing a large area of the fishnet and nano-pillar structure without any significant imperfections, (c) structure C as seen from normal incidence, (d) a tilted profile of a nano-pillar from structure C.

5.3 Results

5.3.1 Measurements at infra-red wavelengths

Optical measurements of the fabricated structures at infra-red frequencies were obtained using a Bruker Vertex Fourier transform infra-red (FTIR) spectrometer with accompanying Hyperion optical microscope and CaF beamsplitter. Reflectance measurements were taken by measuring the reflected light from the top of the fishnet. Transmission measurements were obtained by passing light through the supporting quartz substrate and measuring from above the fishnet. In both reflection and transmission measurements the incident light was polarised using a ZnSe crystal polariser. Reflection measurements were normalised using a 30 nm thick sheet of unpatterned silver on a fused silica substrate as a background while transmission measurements were normalised using 1 mm thick fused silica with 1 μm of PMMA on top. Optical reflectance measurements at visible and near-infrared wavelengths were obtained using the white-light, monochromator and SiGe detector and lock-in amplifier set-up described in chapter 2. As with the FTIR, measurements were normalised using a 30 nm sheet of unpatterned silver and taken at normal incidence above the top of the sample.

Simulated modelling of the structures was undertaken to verify the response of the fishnet and nanopillar structures and estimate values for the refractive index and Q-factor [108]. A 3D, single-unit cell model of the structures was created using the dimensions measured from the fabricated patterns and associated material properties. Reflection and transmission spectra of the structures were obtained using finite difference time domain (FDTD) simulations, using Lumerical FDTD solutions software. The model was illuminated using a plane wave source with a wavelength range of 1000 nm to 4000 nm and the same polarisation as used for the experimental characterisation. A separate model of solely the fishnet structure (without the nano-pillars, PMMA and supporting substrate) was also simulated to help estimate the expected increase in magnitude of n and figure of merit (FOM, defined as *Re(n)/Im(n)*) in when the structure is suspended in air (background n = 1). This also helps further study of the effects the PMMA and nano-pillars has on transmission, reflection and n and FOM. All modelling and simulation work detailed in this chapter was undertaken by Saima I. Khan at the University of Glasgow.

Owing to demands on the processing capability of the modelling, simulations were only performed on structures A and B. Most of the work discussed in this chapter will focus on these two structures. A brief analysis of structure C is included towards the end of this chapter.

Figure 5.6 Shows reflectance measurements from structures A and B taken using TM polarised light (denoted in figure 5.4), TE polarised light (90° rotation of TM orientation) and unpolarised incident light (DOP = 0%). Spectra obtained using unpolarised light are without any polarisation control in the optical beam path and use only the random electric and magnetic field polarisations produced by the light source. The resultant spectrum is a superposition of the two polarised spectra. It should be noted that the reflection is given in arbitrary units in this instance.
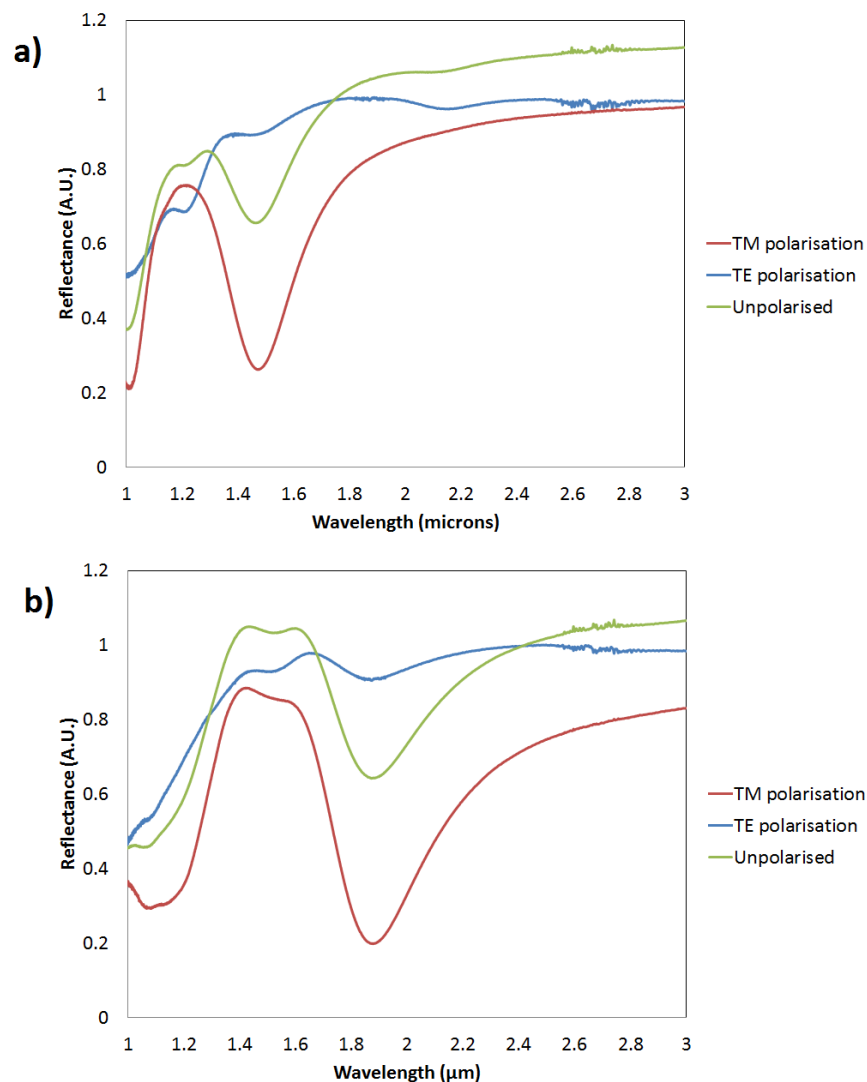
Figure 5.6: Reflection spectra of structure (a) A and (b) for TM polarised, TE polarised and unpolarised incident light. Reflectance values are not normalised and are given in arbitrary units.

The reflectance spectra obtained from structure A exhibit a polarisation dependant trough at 1.45 μm. A similar polarisation dependant trough is observed at 1.88 μm for structure B. These troughs represent the "LC" resonance for each respective structure. With light polarised to produce an incident TM mode, an electric field is induced within the wide metal-dielectric-metal tracks of the fishnet. This results in a strong trough in the reflection measurements of the structure. When incident light is polarised to produce a TE mode and the electric field is aligned parallel to the wider tracks of the fishnet, a current loop cannot easily be induced within the structure. Therefore the capability for the structure to resonate is much reduced and a much weaker trough is exhibited as more of the incident light is simply reflected. Unpolarised light, in which the electric field orientation of incident radiation is not controlled, results in a more prominent trough in reflection measurements than light incident in TE mode but less prominent than light incident in TM mode. This owes to the proportion of unpolarised light that successfully induces a current loop in the structure and, consequently, produces a resonance.

Reflection and transmission spectra obtained both experimentally and by way of simulation for structures A and B are shown in figure 5.7. Resonances are observed experimentally at 1.45 μm and 1.88 μm respectively, as the critical dimensions of the fishnet are increased in scale. A trough can be seen in the experimental transmission spectra at approximately 2.7 μm in both cases. This can be attributed to the excitation of the O-H stretch vibration at 2.7 μm in the fused silica substrate. Figure 5.8 shows the measured transmission spectra of a bare, unpatterned fused silica substrate of type used to support the fishnet and nano-pillar structures. A prominent trough is present at the same wavelength range observed in the experimental transmission measurements of the fabricated structures.
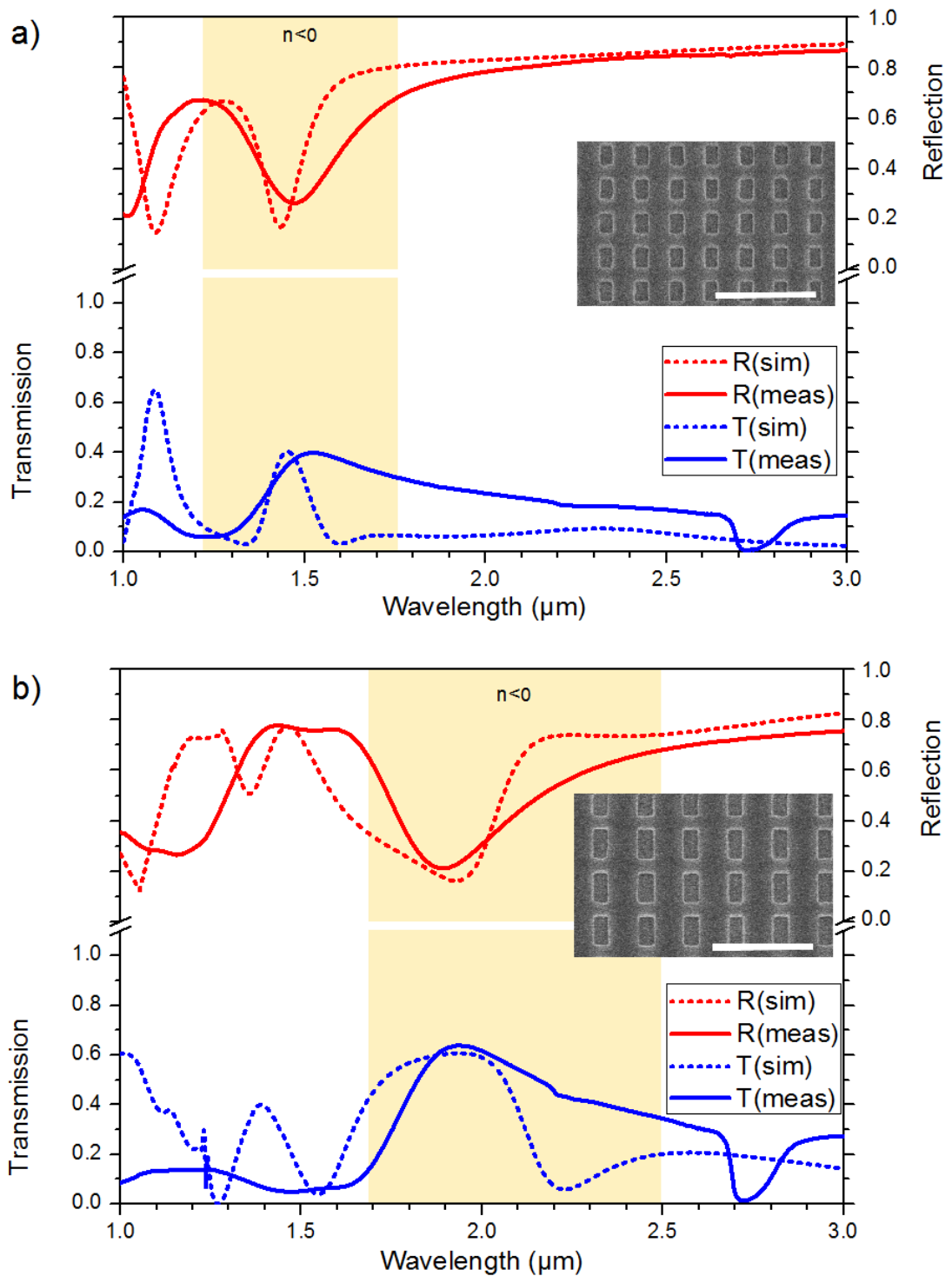
Figure 5.7: Reflection and transmission spectra for both (a) structure A and (b) structure B. Solid lines show experimental measurements while dotted lines represent simulated spectra. Reflection spectra are shown in red and transmission spectra are represented in blue. A discontinuous y-axis is used to separate reflection and transmission spectra for clarity. A micrograph of the respective structure is included inset of the spectra, with a scale bar 2 μm long in both instances. The shaded yellow regions indicate the wavelength range at which the structure has a negative refractive index.
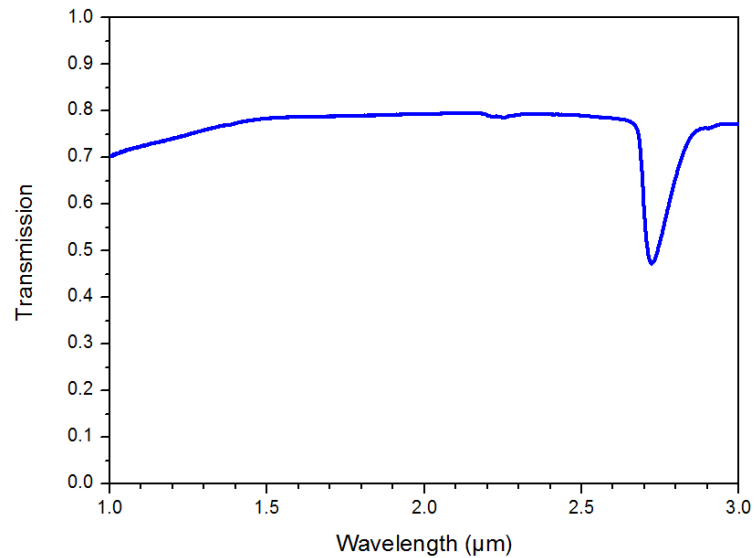
Figure 5.8: Experimental transmission spectra of an unpatterned, 1 mm thick fused quartz substrate without PMMA. It is the same type as used for measurements of the fabricated structures.

The experimental transmission at negative index wavelengths has a maximum magnitude of 40% and 65% for structure A and B respectively. This can be explained by the larger aperture size exhibited in structure B. It should be remembered that the metal-dielectric-metal pillars that are displaced during the imprinting process still fill the area of the fishnet apertures, only they are situated below the fishnet in the PMMA. Therefore from a perspective normal to the fishnet the Ag-MgF$_2$-Ag stack still covers the area of the structure in its entirety. Therefore light can feasibly be transmitted through the structure by two means. Firstly, light can pass through the sidewall of the PMMA between the fishnet and nano-pillars. The imprinted depth of the nano-pillars, i.e. the vertical distance between the top of the pillar and the bottom layer of the fishnet, will have a significant effect on the proportion of light that is able to be transmitted. Light can also be transmitted by extraordinary optical transmission, as described in section 5.1.2.

It is observed from the reflection spectra of both structures A and B that at longer wavelengths the fishnet acts increasingly similar to a mirror, with reflectance tending towards 100% and the transmission decreasing. This can be attributed to the dimensions of the fishnet apertures which will significantly limit or prevent light at longer wavelengths from being transmitted. While there is close agreement between the experimental and simulated reflection and transmission spectra, features in the simulated spectra appear sharper than those measured experimentally. This not uncommon occurrence is largely the result of imperfections present in the fabricated structure, such as potential cracks in the

silver wires and tracks and rounded corners and non-uniform edges of the aperture. While attention is given to modelling the fabricated structures as closely as possible it is not feasible for all defects to be included in the simulations. The material properties, such as refractive index and FOM, of the structures discussed in this chapter are derived using the simulated model and not by experimental means. Therefore consideration should be given to the potential for material properties of the fabricated structures differing slightly from the modelled structures.

Simulations of solely the fishnet portion of the structures, without the nano-pillars, PMMA or supporting substrate were produced to gauge the potential effectiveness of the fabricated fishnet as a negative index metamaterial. The real and imaginary components of n and the respective FOM calculated from these simulations are shown in figure 5.9. Structure A exhibits a negative refractive index of maximum magnitude 4 at 1.48 µm while structure B exhibits an n value of -5 at 2.09 µm. The maximum FOM is calculated as 2.49 and 2.74 for the fishnets of structure A and structure B respectively. This compares closely to the negative index and figure of merit values reported in literature concerning single active layer fishnets (a tri-layer of metal-dielectric-metal) [77,80,98]. The fabrication of the fishnets in these instances is often time consuming and costly. This potentially gives the fishnets patterned by direct nanoimprint an added advantage; similar n and FOM values to comparable structures but created using a faster, cheaper and equally effective fabrication technique. It should however be noted that the values calculated by simulation in figure 5.9 assume that the fishnet is suspended in air (n=1) and are not supported on PMMA on a fused quartz substrate. The imprinted nano-pillars are in this instance not considered either. It should be remembered that this represents an idealised scenario, unless the fishnet has successfully been detached from the supporting substrate [98].
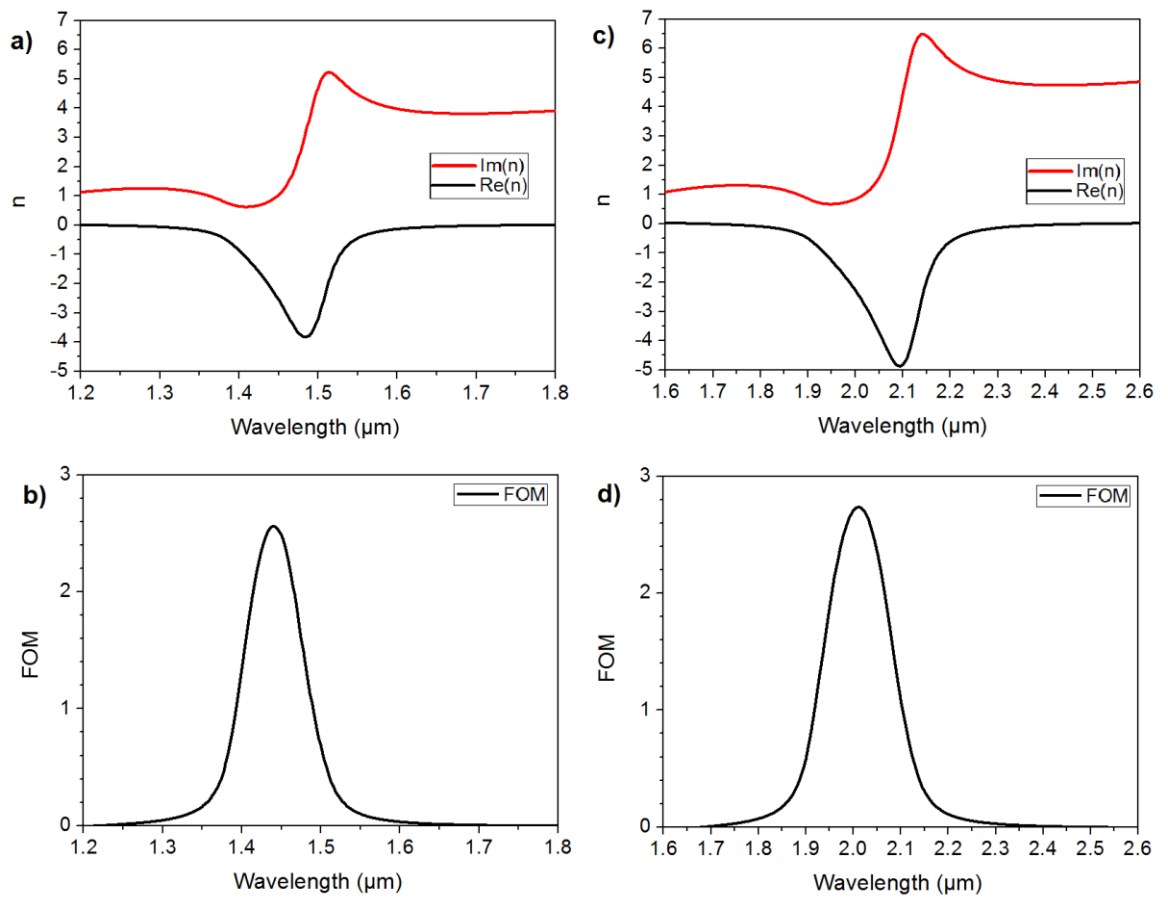
Figure 5.9: Simulated measurements of the refractive index and FOM from the fishnet portion of the structures. (a) shows the real (black line) and imaginary (red line) components of n obtained from the fishnet of structure A and (b) shows the calculated FOM for the same structure. (c) and (d) are the respective results obtained from the fishnet of structure B.

If the fishnet is supported on top of a substrate the respective optical properties, such as reflectance and transmittance and by connection n and FOM, will invariably be different than if the metamaterial were suspended in air. In the case of the structures reported in this chapter, there are a number of components that can contribute to an increase in optical losses and a decrease in the magnitude of n and FOM. Firstly, the fused silica substrate is a source for optical loss. The wavelength dependant refractive index of SiO_2 means that while the material is transparent at visible frequencies, it becomes increasingly opaque towards the infra-red. The fabricated structures use a 1 mm thick fused silica substrate as it was found that thinner silica substrates could not withstand the high imprint forces required for patterning, thus adding to the optical losses. As shown in figure 5.8 even when the bare, unpatterned substrate is measured transmission never rises above a maximum value of 80%. The 1 µm thick PMMA layer is another source for introducing losses to the fabricated structures, introducing physical discontinuities, an increase in n when compared to air (PMMA = 1.49 at NIR) and a refractive index change between the substrate and metamaterial. Although the

transmission of both structures A and B has been shown to be approximately 40% and 65% at resonance, the removal of the metal-dielectric-metal nano-pillars beneath the apertures of the fishnet should improve the transmission of the structures.

Simulations of the entirety of structures A and B (substrate, PMMA, nano-pillars and fishnet) and not just the fishnet pattern help illustrate the effects that added asymmetry produce, as shown in figure 5.10. It is observed that there is a notable reduction in the magnitude of the negative refractive index at near resonant wavelength. The refractive index real part of structure A is computationally measured as -0.24 at 1.53 µm compared to -4 at 1.48 µm when just the fishnet portion of the structure is simulated. Similarly, structure B exhibits a refractive index real part of -0.7 at 2.35 µm as opposed to a value of -5 at 2.1 µm when modelling purely the fishnet.
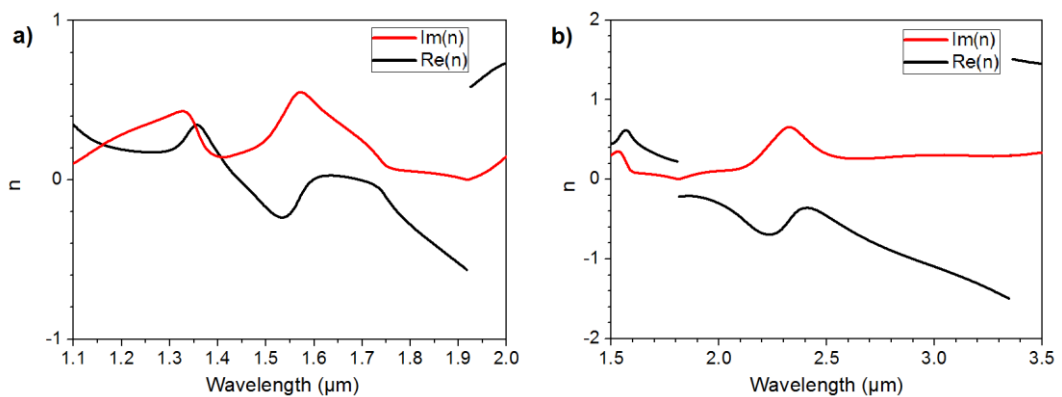
Figure 5.10: Real and imaginary values of n obtained from simulations modelling the entirety of structure B – substrate, PMMA, nano-pillars and fishnet – for structure (a) A and (b) B.

The wavelength dependant values of n in figure 5.10 show a broader negative region than exhibited by just the fishnet in figure 5.9. The negative refractive index can be seen to increase in magnitude from -0.7 at resonance to -1.5 at 3.35 µm. Discontinuities are also observed in the real component of n. These are potentially an artefact of the simulation model, which displays not only physical asymmetry but numerous material refractive indices and a large simulation region that together stretch the capabilities of the modelling software and hardware it runs on. These discontinuities however are not without precedent and are clearly visible in work concerning asymmetric fishnets previously reported by Koschny et al [109], Zhou et al [110] and others [111-113]. Chen et al [113] cites the sensitivity of the impedance (z) and by association the refractive index to small perturbations in the reflection and transmission, particularly when either R or T

are small in magnitude as factors in the appearance of these discontinuities. The volatility of the reflection and transmission coefficients is further increased by increased asymmetry and impedance mismatches [98,110]. The FOM for the as fabricated structure is not presented because discontinuities due to multiple refractive changes in the material make the calculation unreliable. Koschny et al [109] notes the effect of periodicity on these "unphysical" spectral anomalies and their prominence in metamaterials with a reduced translational symmetry in the direction of propagation.

It was established by Shalaev et al in 2005 [114] that a periodic array of metal-dielectric-metal nanorods, not unlike the nano-pillars discussed in this chapter, can exhibit a negative index of refraction. In this work Shalaev reports an n value of -0.3, which is in part achieved by optimising the nanorods dimensions and periodicity. It should be remembered that when using the NIL technique to produce fishnets, any optimisation of the pillar dimensions or periodicity will have a direct effect on the optimisation of the fishnet, as both are defined by the same nanoimprint stamp. Field plots of the structures at resonance (figure 5.11) show electromagnetic coupling between the fishnet and imprinted nano-pillars. It is observed that the electric field strength at the material interfaces at the aperture of the fishnet are stronger for structure A than they are for structure B.
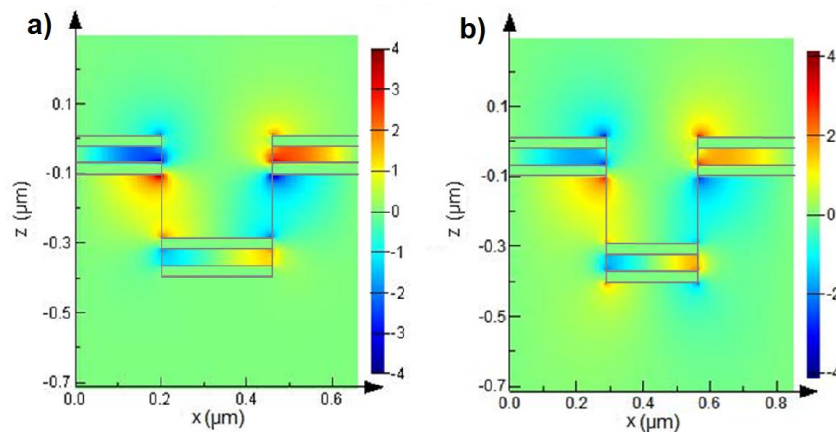
Figure 5.11: Field plots showing the electric field distribution in the fishnet, PMMA and nano-pillars at their resonant wavelength. (a) A cross section of structure A (x-z plane) at 1.45 µm and (b) the respective plot obtained for structure B at 1.88 µm. An outline of the structure has been added to both plots for clarity and axis values are in microns. Light is polarised as indicated in figure 5.4.

It is noted from the cross-sectional field plots that the electric field strength is strongest at the aperture edges of the MgF_2 layer of the fishnet. Considering the LC equivalent model (figure 5.2) and the location of the electric field "hot-spots" for the SRR structures detailed in chapters 2 and 3, this is expected. The electric

field strength is also noted to be moderate in the MgF_2 layer of the imprinted nano-pillar. The field plots also show that current flow on the top and bottom silver layers of the fishnet are out of phase, as illustrated in figure 5.2. It has been shown in the literature that the addition of a substrate, or other forms of increased asymmetry, weakens the plasmonic coupling across the dielectric gap between the metal layers [92]. While the behaviour of the plasmons is largely dependent on the characteristics of the dielectric and surrounding metal, the electromagnetic field can penetrate into a substrate or surrounding material, weakening the plasmonic coupling.

It has been shown that adding more metal-dielectric layers to a fishnet, thus increasing the number of functional layers, reduces the effect of the substrate. This is explained as an increase in the number of functional layers results in the currents in the metal tracks being prevalent further away from the interface with the substrate. As the fishnet structures studied in this chapter contain only one functional layer, the presence of the PMMA and nano-pillars significantly inhibits the plasmonic coupling and the effectiveness of the structure operating as a NIM. The field plot shown in figure 5.12 displays the magnitude of the electric field distribution in a single unit cell of the fishnet of structure A within the top silver layer at the interface with air. This cross section is taken in the x-y plane at the 0 μm position of the z-axis of figure 5.11. The distribution pattern shows a strong electromagnetic field along the wide tracks parallel to the long edge of the fishnet aperture, although it is noted that the variation between the weakest and strongest field strength is low.
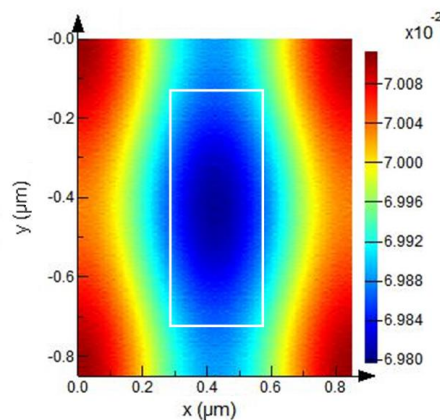
Figure 5.12: Electric field distribution of a single unit cell of the fishnet of structure A from a perspective of normal incidence (x-y plane). The top silver layer is in view with the fishnet aperture in the centre. An outline of the structure has been added to both plots for clarity and axis values are in microns. Light is polarised as shown in figure 5.4.

5.3.2 Measurements at visible wavelengths

Experimental and simulated reflectance measurements at visible and NIR frequencies of both structure A and B were taken between 500 nm and 1000 nm and are shown in figure 5.13. Multiple broad peaks are exhibited in both plots, the most prominent of which are located at 585 nm and 700 nm for the experimental measurements of structure A and B respectively.
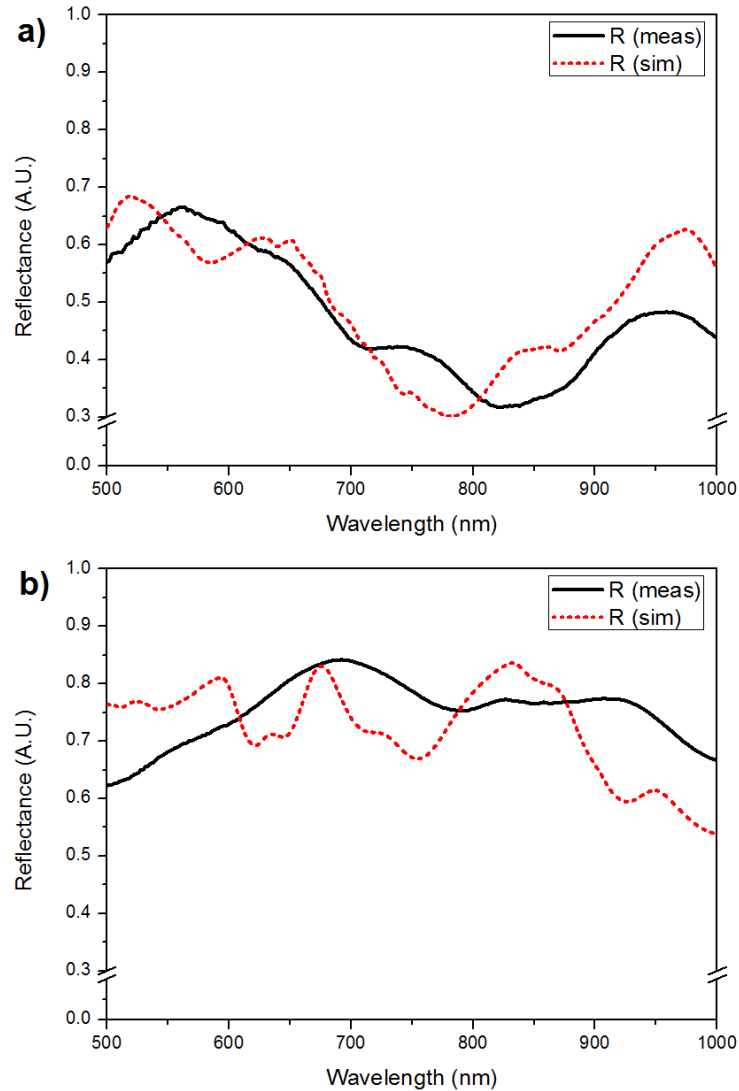
Figure 5.13: Reflectance measurements of (a) structure A and (b) structure B at visible and near-infrared wavelengths, 500 nm to 1000 nm. Experimental measurements are represented using a solid black line and simulated results are shown using a dashed red line. Incident light for the experimental measurements was unpolarised and the TE and TM measurements obtained from the simulation were averaged to give a comparable spectrum.

The difference in the experimental peak positions seen in Figure 5.13 (a) and (b) can be attributed to the physical change in size between the nano-pillars of structure A and B. As previously indicated the nano-pillars of structure A have approximate dimensions 220 nm by 420 nm giving a surface area of 92400 nm^2.

Nano-pillars present on structure B have approximate dimensions 270 nm by 590 nm resulting in a surface area of 159300 nm^2. Brief analysis of the nano-pillar and fishnet dimensions detailed in figure 5.4 shows that structures A and B have approximately the same fill-factor, defined as the ratio of fishnet surface area to the nano-pillar area of a unit cell. This is calculated to be approximately 69% for structure A and 73% for structure B. Although there is agreement between the experimental and simulated results with regard to the peak positions, it is noted that the spectra obtained from the simulated reflectance measurements are generally sharper and more distinct than those obtained experimentally. This feature is not uncommon when comparing experimental measurements with simulated ones. Reasons for the disparity may include physical imperfections present in the fabricated structures and artefacts from the simulated model, such as those resulting from the numerous refractive index changes, impedance mismatches and the highly asymmetric nature of the structure.

5.3.3 Resonant wavelength shift with scaling of dimensions

The experimental reflection and transmission spectra of structure C at infra-red wavelengths are displayed in figure 5.14. This structure has not been simulated as its increased dimensions and continued asymmetry consistently produced large and unstable simulations that were either unreliable or could not be adequately processed. For this reason simulated spectra, electromagnetic field plots and material properties such as refractive index and FOM have not been obtained. It is noted that the structure exhibits very low transmission below the resonant wavelength, as with structures A and B. Multiple features, particularly in the reflection spectrum, are also observed to be more prevalent than the other two structures. The LC resonance peak is present at 3.26 μm. The resonance trough seen in the reflection spectrum is less prominent than the ones observed for structures A and B. This could be attributed to the potential for a reduction in coupling or increased losses brought about by the presence of the PMMA and larger nano-pillars. The fill factor is calculated to be 62%, the lowest of the three fabricated structures. The resonant peak in the transmission spectrum coincides with the wavelength range at which atoms in CH_2 groups exhibit the asymmetric stretching mode of PMMA. Most of the light obtained in acquiring the reflection spectrum is reflected off of the metal of the fishnet and pillars. It is unlikely that any significant amount of light is reflected off of the PMMA. For this reason the

absorption trough between 3.3 μm and 3.5 μm is only seen in the transmission spectrum, where light has directly passed through the fused silica substrate, PMMA and Ag-MgF$_2$-Ag layers of the fishnet and nano-pillars. This brings about the potential for the fishnet and nano-pillar structure to enhance two separate resonances and for them to be measured independently. A material beneath the fishnet may be enhanced and measured by the transmission of light while a material placed on top of the fishnet could conceivably be enhanced by measuring the reflected light off the structure. This would of course be dependent on the separate wavelength positions of any reflection and transmission peak. The trough in transmission at 2.7 μm is due to the O-H stretch vibration in the fused silica substrate. The presence of water in the atmosphere results in the small, narrow-band peaks seen most prominently in the reflection spectrum around 2.6 μm.

Analysis of figure 5.14 suggests that the absorption of light in structure C is higher than structures A and B, particularly at shorter wavelengths.
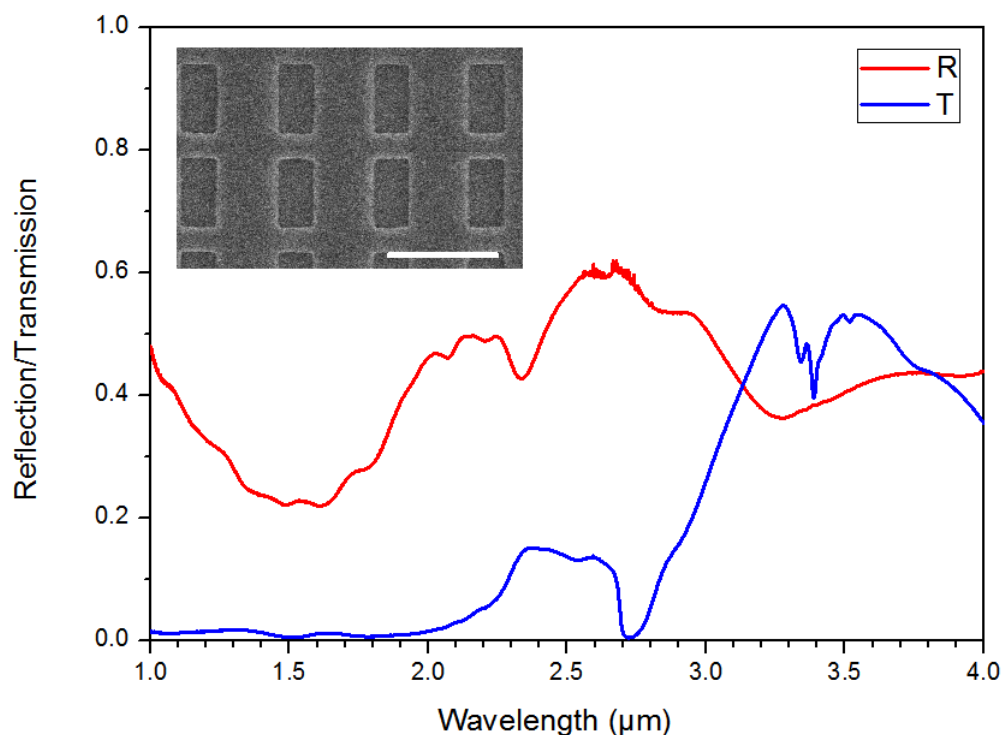
Figure 5.14: Measured reflection and transmission spectra obtained from structure C, with a micrograph of the structure inset. The scale bar represents 2 microns.

A comparison of the experimental reflection and transmission spectrum of all three structures is displayed in figure 5.15 The LC resonant peaks from each structure have been marked on the respective spectrum. Measurements are shown

from 1 μm to 4 μm to account for the longer resonant wavelength of structure C. The reflection and transmission for structures A and B have been re-measured accordingly from the spectra displayed in figure 5.7. Both the resonant peak and the resonant trough can be seen to broaden as the resonant wavelength lengthens, i.e. as the structure is scaled to larger dimensions. With the resonant peak of structure C tuned, albeit unintentionally, to the wavelength of the molecular CH_2 asymmetric stretch vibration the feature is noticeably enhanced when compared to the transmission spectra of structures A and B.
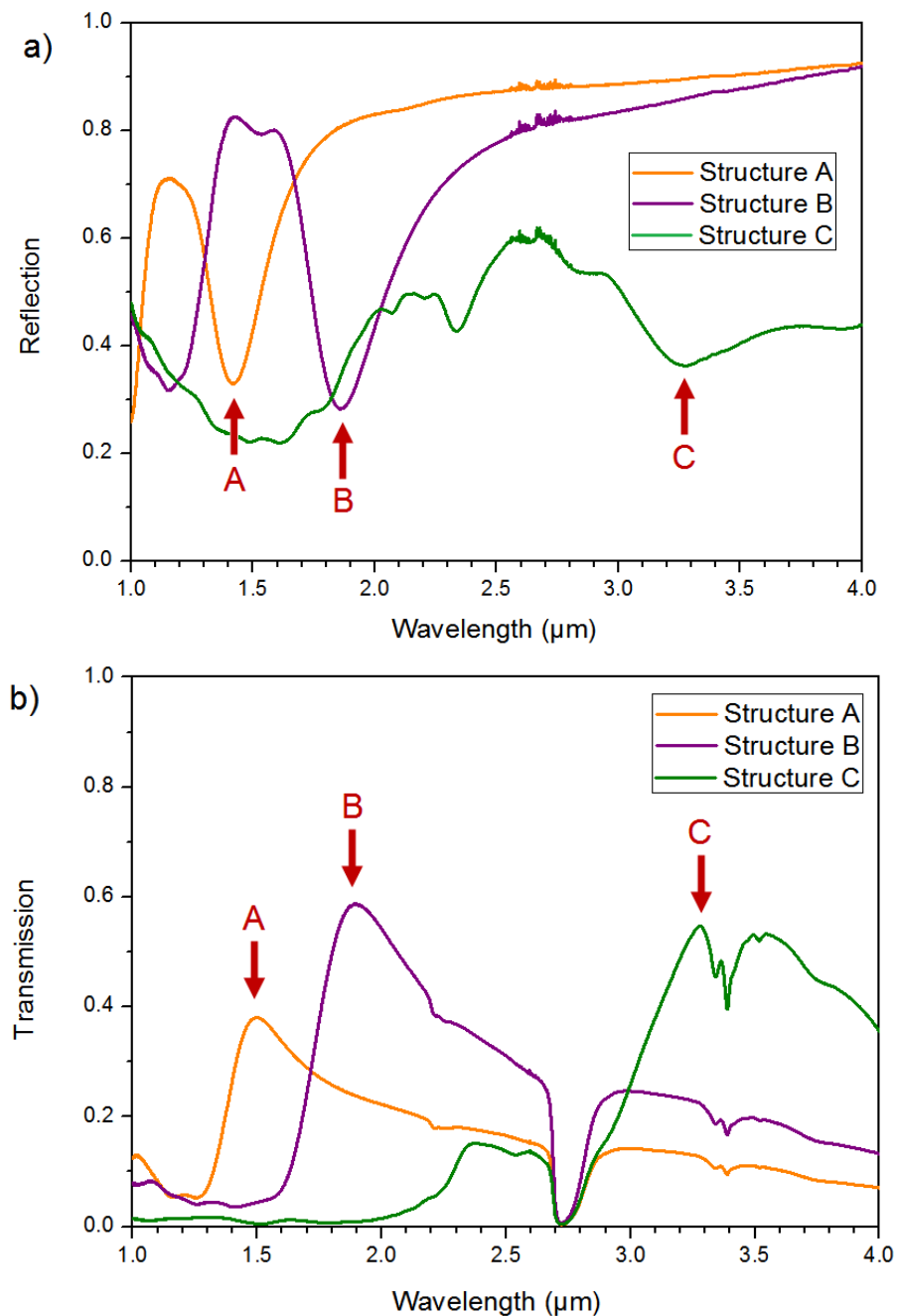
Figure 5.15: Comparison of structures A, B and C for (a) reflectance and (b) transmission spectra.

As the track width of the fishnet, w_x in figure 5.4, can be considered the most important in dictating the resonant wavelength, figure 5.16 demonstrates the scaling relationship between these two values. It should of course be remembered that the window dimensions, constituent materials and surrounding conditions (such as the presence of a substrate or cladding) also contribute to the location of the LC resonance.
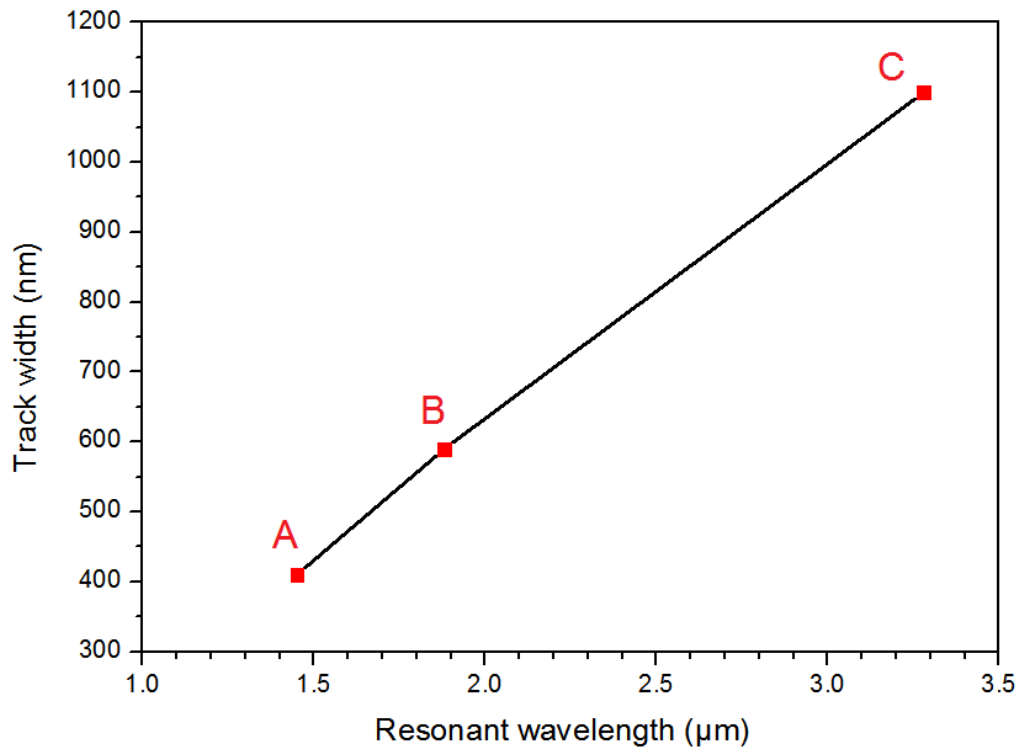
Figure 5.16: The resonant wavelength plotted against the track width of structures A, B and C.

The resonant wavelength can be seen to increase almost linearly with the fishnet track width for the three structures. There is only a very slight divergence, which can reasonably be attributed to fabrication imperfections and the variation in the ratio between the dimensions for the unit cell of each structure. At wavelengths shorter than the range considered in this chapter, the linear relationship between resonant frequency and fishnet dimensions would not be expected to continue. As with SRRs the plasma frequency of the constituent metal would become the dominant feature and prevent the resonance shifting to shorter wavelengths.

5.4 Chapter conclusions

The work contained in this chapter has demonstrated a successful and novel technique in the fabrication of metamaterial fishnets. The nanoimprint technique

employed removes the conventional requirement of etching or depositing multiple metal and dielectric layers with the aid of a mask. This not only simplifies the fabrication process but also enables large area metamaterials to be produced. The structural quality of the fabricated structures is comparable with that of conventional methods such as EBL and FIB milling.

The fabricated structures have been simulated to estimate their material properties. The effect of the nano-pillars, an artefact from the direct NIL process, has also been studied. While the presence of these pillars and the supporting PMMA and substrate has been shown to decrease the n and FOM values of the fishnet, the transmission of light has been measured to a maximum value of 65%, present at resonance for structure B. Modelling of solely the fishnet portion of the structures has suggested that a refractive index of -5 and FOM of 2.74 can be achieved. These values are largely comparable with previously reported single active layer fishnets fabricated by EBL and FIB milling. Enhancement of the molecular CH_2 asymmetric stretch vibration at 3.4 μm has been shown in the transmission spectrum of structure C, originating from the presence of PMMA beneath the fishnet. As this feature was not present in the reflectance spectrum, this introduces the possibility for the fishnet and nano-pillar structure to be used for sensing by means of enhancement. This may enable the molecular or atomic resonances of materials beneath the fishnet to be measured by transmission only, allowing for a separate resonance to be enhanced by placing a material on top of the fishnet and measuring the reflectance.

The NIL technique demonstrated in this chapter can conceivably be adapted to imprint a large area of alternative designs directly into material stacks or, of course, a single metal layer. Additional ideas for future work involving this fabrication technique and improving the capability of the fishnet structures are included in chapter 7.

Acknowledgement

Chapter 6

Nanoimprinted polymer rib waveguides with photonic crystal biosensor
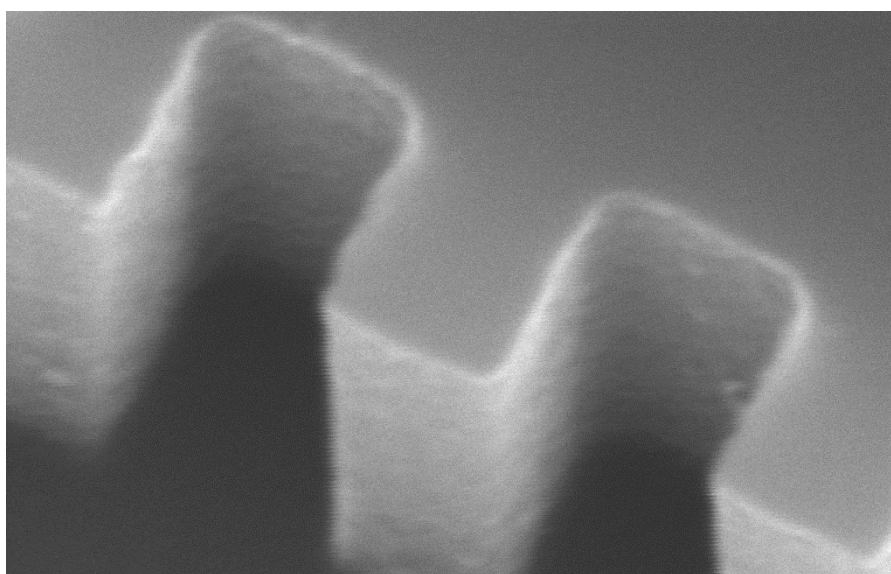
Abstract

This chapter focuses on the fabrication and performance of polymer photonic biosensors that were designed, completed and tested as part of the P3SENS European Consortium funded project. The development of these sensors, designed to be integrated onto a "lab-on-a-chip", was contributed to by a number of project partners across Europe. This chapter will largely confine itself to the work performed in the University of Glasgow in fabricating the polymer sensor component of the chip and enhancing its performance. As part of this work, numerous methods were developed to ensure high quality waveguide and Bragg mirror structures could be produced using a high refractive index polymer. While the sensor studied in this chapter cannot be described as a metamaterial, there are numerous sensing concepts discussed that can be described as interdisciplinary. Nanoimprint lithography is again used as a fabrication technique to create the polymer sensors because of the potential for low manufacturing costs and reproducibility.

6. 1 Introduction

There are numerous requirements a biosensor must have if it is to be used in a healthcare environment. Firstly, and arguably most importantly, it must be reliable in detecting the analyte it is designed to sense. This not only means it should detect a certain concentration of a given analyte in a fluidic solution, but also that substances that are not of interest are not falsely detected. In addition to accuracy, a biosensor should function quickly in detecting analytes, particularly when time is a critical factor in treating a patient. From a practical and commercial perspective, the manufacture of sensors should be cheap, fast and reproducible, meaning each sensing chip functions in the same way irrespective of quantity made.

The photonic biosensor described in this chapter was researched as part of the Polymer Photonic multiparametric biochemical SENSor for Point of car diagnostic (P3SENS) [115] project, which included a number of collaborating academic and commercial partners from across Europe. Each partner contributed a certain skill or capability to the project, with the University of Glasgow leading the design and fabrication of the nanoimprint stamps used to create the polymer sensor. The

main purpose of the project was to create a mass reproducible sensor that could be used in detecting certain analytes (in this instance proteins) that are common indicators of a cerebrovascular event, more commonly known as a stroke. These proteins are in part detected using a molecular binding technique that is a replication of the antigen and antibody binding mechanism found in nature. An antigen, also known as an antibody generator is, simply put, a molecule that is attracted to and binds to a specific antibody, provoking an immune response from the body. These proteins would be sourced from a blood plasma sample that is channelled to the sensor component of the chip using microfluidics. The basic concepts regarding the detection of particular proteins and the "lab-on-a-chip" design are discussed as background information, but the focus of this chapter is given to the operation and fabrication of the polymer biosensor, which is comprised of a waveguide and adjacent Bragg mirror cavity.

6.1.1 Screening for cerebrovascular diseases

Cerebrovascular events, more commonly referred to as strokes, are amongst the most common causes of permanent disability and death in adults worldwide. The likelihood for treatment to be effective is greatly enhanced when diagnosis is delivered as soon as possible after the stroke has occurred [116,117]. The most common type of stroke, an ischemic stroke, occurs when an artery in the brain becomes partially (transient ischemic attack, TIA) or entirely obstructed. This accounts for approximately 80% of strokes [118]. Haemorrhagic strokes are less common and occur when a cranial artery ruptures, which can lead to a build-up of pressure on parts of the brain or other blood vessels and subsequent damage.

Currently strokes are commonly diagnosed by physical response tests of the patient and brain imaging scans. This is not only time consuming but, with regard to computer tomography (CT) and magnetic resonance imaging (MRI) scans, in many cases cost prohibitive. However the occurrence of a stroke produces an increase in the concentration of certain proteins in the bloodstream. No single protein has been demonstrated as a clear indicator for diagnosis of a stroke [119,120]. Rather a panel of specific proteins can yield a more accurate and trustworthy indication of the occurrence of a stroke. A total of six biomarkers – S100b, H-FABP, NSE, Troponinm BNP and CRP – were selected from the literature to be used as biomarkers [119,121-123]. Measuring the concentration of these

biomarkers in a given quantity of blood plasma can therefore give a decisive indication as to whether or not the brain has suffered from a cerebrovascular event and if it has, its severity.

6.1.2 Lab-on-a-chip

Certain single unit devices that can perform a number of functions are sometimes referred to as a "lab-on-a-chip". These multiple functions are usually combined to create a sequential chain of tasks that enable a specific process to be completed. This can include, amongst other functions, the collection and storage of a particular substance, the separation of particular molecules from a fluidic sample or controlling the movement of targeted molecules. In this respect, the single chip performs the functions that would usually be undertaken in a laboratory, hence the name.

The chip designed under the P3SENS project would be required to receive a blood plasma sample and channel it to a photonic sensor region, where the proteins of interest could be detected by spectroscopy. This would require an input and output interface in which laser light from an external source could be coupled to and from the sensor. The light output from the chip would then be analysed and compared to the original source beam for changes indicating the presence of the given proteins. This spectral comparison would be performed by a computer that is external but connected to the chip. To undertake these tasks, the chip can be thought of as three separate component parts, each of which performs a certain function. These three parts include a grating coupler and waveguide pattern for receiving and outputting light as well as controlling its propagation, a Bragg mirror sensor section and a microfluidic layer that channels the analyte over the sensor. This is shown in figure 6.1.

As with many instruments and devices used in the medical profession, contamination and cleanliness are paramount concerns. Therefore the chip would need to be used as a consumable – to be disposed of after operation and never re-used. This adds to the demand for the device to be manufactured en masse and at low cost. For this reason a polymer is selected to form the grating couplers, waveguides and Bragg mirror sensors and nanoimprint lithography used to define

the structures. This polymer layer is then attached to the plastic microfluidic and cladding layer.
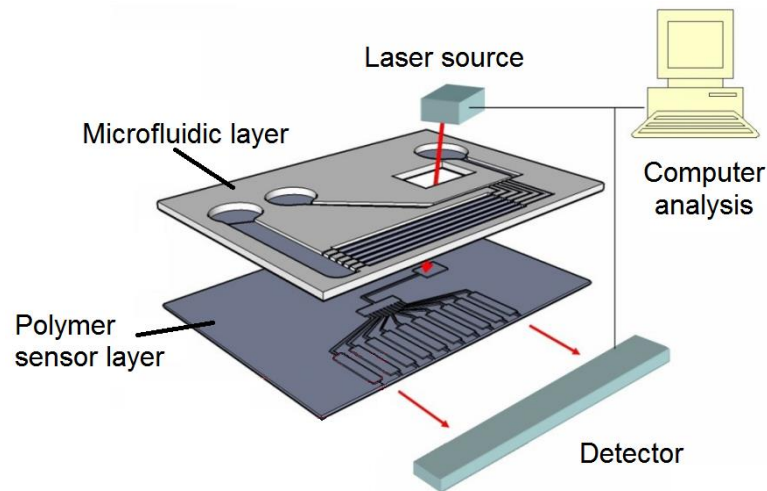
Figure 6.1: Conceptual diagram showing the component parts of the lab-on-a-chip and its operation with an external analysis system.

6.2 Operation principles

There are three components to the polymer sensor layer – grating couplers that enable the input and output of light to and from the device, rib waveguides to control light propagation and Bragg mirror cavities that are used in the sensing of analytes [123]. This section will look at the basic concepts for their functionality in turn. It should be noted that the detailed optical theory for each component is not covered here.

6.2.1 Grating couplers

Grating couplers are a series of periodic structures that are used to couple light into and out of a waveguide [124, 125]. The corrugated structure is used in place of simply focusing light directly into the end facet of a waveguide, also known as end-fire coupling. End-fire coupling requires very precise alignment of the incident light into the waveguide. Failure to adequately focus the light onto the waveguide facet, which in this instance has dimensions less than 1 micron in size, decreases the coupling efficiency, η, and reduces the likelihood of both light coupling to adjacent cavities or successfully propagating the length of the waveguide. The coupling efficiency can, in simple terms, be considered as the ratio of light coupled into the waveguide against the light incident on the facet.

$$\eta = \frac{Pw}{Pin} \qquad\qquad\qquad\qquad (6.1)$$

Where P_w is the optical power of light coupled into the waveguide and P_{in} is the power of the light incident on the facet or grating coupler. This can be displayed in terms of loss in decibels (dB).

$$L = 10log\frac{Pin}{Pw} \qquad\qquad\qquad\qquad (6.2)$$

The grating structures used for the biosensing chip are positioned directly on top of the guiding layer for propagation into the waveguides. This and the coupling concept are demonstrated in figure 6.2. The periodic grating can be considered as a periodic alteration of the permittivity with a spatial grating periodicity of Λ. Light, incident upon the gratings at an angle θ_{inc}, can either be reflected or transmitted by the grating coupler. Depending on the wavelength of the incident light, λ, and the periodicity, Λ, multiple modes will be diffracted at numerous angles. Assuming that the grating couplers are situated on top of the waveguide surface (which itself is exposed to air), these parameters are related in the following grating equation [126],

$$n_{eff} = n_{air}sin\theta + m\left[\frac{\lambda}{\Lambda}\right] \qquad\qquad\qquad (6.3)$$

where n_{eff} is the effective index of the gratings and waveguide, θ is the coupling angle, m is the mode diffraction order, λ is the wavelength of incident light and Λ is the grating periodicity. While the refractive index, n, is used in relation to light that is unguided and not propagating in a single direction, the effective refractive index is used as a parameter for waves that are guided along a given plane.
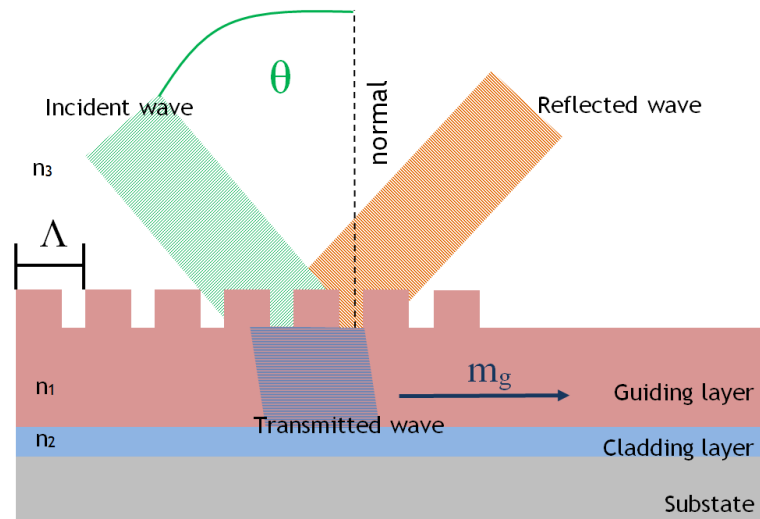
Figure 6.2: Schematic showing the structure and main parameters of a grating coupler structure used to couple light into a waveguide. The guided mode is donated by m_g.

With the incident light illuminating the grating coupler one of the consequent diffraction orders excites the modes, enabling propagation along the waveguide. Fabrication imperfections can both reduce the coupling efficiency and change the effective index of the structure.

6.2.2 Rib waveguides

A waveguide can be considered, in simple terms, to be a structure that physically guides or controls the propagation of an electromagnetic wave in a given direction. Waveguides can come in a variety of forms, such as strip-loaded waveguides, ridge waveguides and diffused waveguides amongst others. Due to the use of NIL as a fabrication technique, the waveguide used as part of the photonic sensor is a rib type waveguide. Rib waveguides exhibit a ridge structure that resides on top of a slab of the same material (and therefore the same refractive index, ignoring compression). A schematic is shown in figure 6.3. By spinning the polymer on a substrate and then imprinting into it the rib waveguide profile can be defined, with the residual polymer layer forming the "slab" beneath the ridge-like structure on top [127,128].
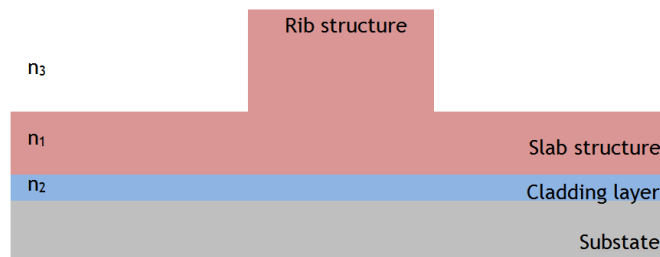
Figure 6.3: A rib waveguide structure, highlighting the differences in materials and their refractive indices.

For light to successfully propagate along the path of the waveguide, the refractive index of the polymer must be higher than that of the surrounding materials. A high refractive index contrast between the guiding material and cladding materials helps reduce losses and ensure light is guided the length of the waveguide. For this reason P84 polyimide with a refractive index of 1.64 at 1310 nm wavelength was selected for use. While other polymers with higher refractive indices exist, consideration must also be given to the viscosity of the polymer and its compatibility with deep imprinting. With regard to reducing losses, it is also important that the residual slab layer (shown in figure 6.3) is sufficiently thin to confine the propagating mode laterally in the rib waveguide.

Losses associated with rib waveguides are often attributed to imperfections (such as rounding and increased roughness) in the sidewall of the rib structure. This type of waveguide is often fabricated using a silicon on insulator (SOI) substrate and etching the rib pattern in the Si. The linearity and roughness of the sidewalls following etching is of primary concern regarding losses and, although the structures studied here are made by NIL, these imperfections still remain. For the light to remain confined to the waveguide, it is also important that the "trenches" that run either side of the rib are sufficiently deep that the propagating waves do not leak. The depth of the trenches that define the rib is in a large part dependant on the viscosity of the polymer, the total PI thickness and consequently the ease at which the stamp can be imprinted.

Figure 6.4 shows a rib waveguide and the geometrical components that define the structure. Using the difference in the effective index of the rib and slab portions of the structure, which is dependent on both the structure and the propagating mode, boundary conditions can be defined.
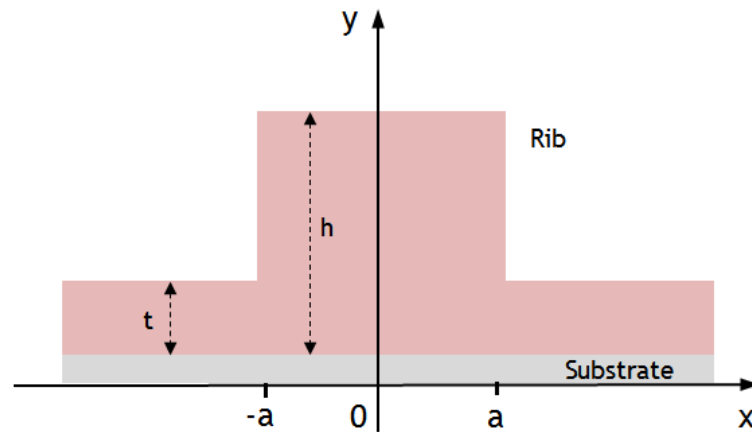
Figure 6.4: A cross section of a rib waveguide indicating physical parameters.

From figure 6.4, the width of the rib is from –a to a, h is the thickness of the rib from the material interface and t is the thickness of the slab from the material interface. The height of the rib waveguide is defined as the difference between h and t. The effective index of the rib and slab are notated as $n_{eff(h)}$ and $n_{eff(t)}$ respectively. The effective index can be expressed as [129]

$$n_{eff} = \frac{\beta}{k} \qquad (6.4)$$

where ß is the propagation constant in the direction of the waveguide and k is the wavenumber, defined as k = 2π/λ. A wavenumber can be thought, in simple terms, as the spatial frequency of a given wave or, alternatively, the number of radians for a certain distance (wavelength). The propagation constant ß can be expressed by [129],

$$\beta = kn_1 \cos \phi \qquad (6.5)$$

where φ is the inclination angle of the wave propagating along the waveguide.

The boundary condition is continuous for E_z at x = ±a. For these boundary conditions, the effective indices $n_{eff(h)}$ and $n_{eff(t)}$ can be used in the following dispersion equation [130]:

$$u \tan(u) = \frac{n_{eff}^2(h)}{n_{eff}^2(t)} w \qquad (6.6)$$

In this equation both u and w are transverse wavenumbers defined as

$$u = \frac{kW}{2}\sqrt{N_{eff(h)}^2 - \left(\frac{\beta}{k}\right)^2} \qquad\qquad (6.7)$$

and

$$w = \frac{kW}{2}\sqrt{\left(\frac{\beta}{k}\right)^2 - n_{eff(t)}^2} \qquad\qquad (6.8)$$

At an interface between two media with different refractive indices, near-field waves called evanescent waves can occur. These waves are produced when a propagating wave is internally reflected at an angle greater than the critical angle at the material interface. As the refractive index of the waveguide is higher than the surrounding air and cladding, conditions are created for total internal reflection to occur, enabling light to successfully propagate the length of the waveguide. When a wave propagates due to TIR, a certain amount of energy from the mode penetrates and decays into the lower refractive index medium. The components of the mode are complex in nature and the amplitude of the evanescent wave decays exponentially as the physical distance from the material boundary increases. The evanescent wave propagates in the same direction as the rays propagating inside the waveguide (i.e. parallel to the material boundary). The presence and behaviour of evanescent waves is shown conceptually in figure 6.5.
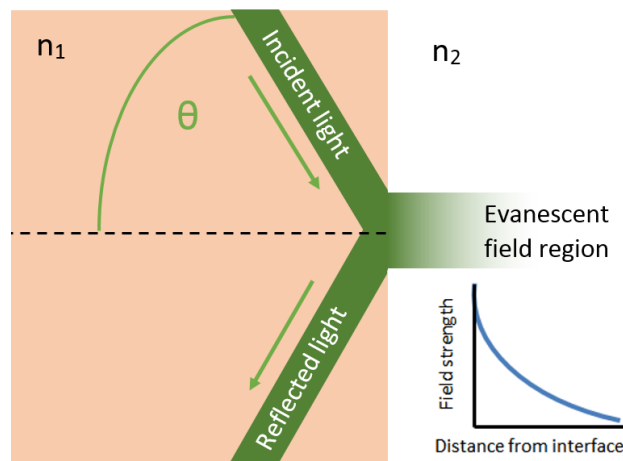
Figure 6.5: A diagram showing the exponential decay of evanescent waves at a material interface, where $n_1 > n_2$.

The waveguides used in the photonic chip described in this chapter have the primary function of guiding light within close proximity to the Bragg mirror cavities. It is this structure that enables the sensing of biological analytes.

6.2.3 Bragg mirror cavities

A Bragg mirror typically takes the form of a one-dimensional array of contrasting high and low index gratings. This refractive index contrast can be provided by two separate physical materials or, as is often the case, one high index material and air acting as the low index medium. A diagram showing a Bragg grating arrangement is shown in figure 6.6. The refractive index of the low and high material is denoted by n_l and n_h respectively while the width of a single grating of low and high refractive index is w_l and w_h respectively. The structural periodicity is given as Λ. The contrasting refractive index boundaries each create a partial reflection of an optical wave. The wavelength of this reflected wave is dependent on the refractive index and width of the Bragg grating. If the wavelength of the light propagating through or near to the Bragg grating is approximately four times the optical path difference, the multiple reflections are enhanced by means of constructive interference. As light at a certain wavelength is reflected, transmission spectra obtained at the output of the Bragg gratings show a trough, or stop-band, due to a reduction in the wave power. The wavelength at which light is reflected, the Bragg wavelength is denoted by, λ_B.
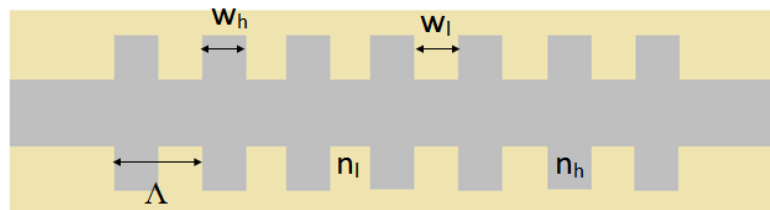
Figure 6.6: Diagram of a typical Bragg grating structure.

The Bragg wavelength, grating period and effective index, n_{eff}, are related by [131]

$$\lambda_B = 2n_{eff}\Lambda \tag{6.9}$$

A higher contrast between the refractive index of n_l and n_h results in a broadening of the stop-band, i.e. a wider range of wavelengths are reflected and not transmitted. The number of individual Bragg mirrors, if one grating is considered as equal to the period, Λ, is also significant in determining the output transmission spectrum. Increasing the number of Bragg mirrors increases the reflection of light at the stop-band wavelength (reduces transmission) and improves the cavity's

effectiveness as a stop band filter. The bandwidth of the stop-band, Δλ, can be quantified using the following equation [132]:

$$\Delta\lambda_0 = \frac{4\lambda_B}{\pi} \, arcsin\left(\frac{n_h - n_l}{n_h + n_l}\right) \qquad\qquad (6.10)$$

Bragg mirror gratings positioned within the field of the evanescent waves reflect the light at the Bragg wavelength, reducing the energy of the evanescent wave at this frequency. In turn the energy from the waves propagating in the waveguide is also reduced at this frequency, resulting in a trough in the transmission spectrum.

In much the same way that the sensitivity of SRRs to localised PMMA was measured in chapter 3, biological samples can be sensed by detecting a shift in the resonant wavelength. With a Fabry-Perot sensing cavity consisting of Bragg gratings, a certain shift in the resonant trough viewed in the transmission spectrum can suggest the presence of an analyte in an applied fluidic sample. For this analyte to be detected, the fluidic sample must be passed across the surface of the sensory cavity. By way of molecular binding the analyte, in this instance the protein biomarkers would attach to the surface of the imprinted structure with the aid of a biological adlayer, such as a grafted antibody sample that can bind with the proteins of interest [133,134]. This selection mechanism prevents proteins that are not of interest in determining the occurrence of a stroke from binding onto the sensor surface, yielding a different transmission spectrum than would be obtained if protein binding were successful. With molecular binding of proteins to the surface of the sensor, the surface sensitivity (as opposed to the bulk sensitivity) of the device is of particular importance. This is largely determined by the refractive index contrast between the core and cladding layers as well as the thickness of the core (rib waveguide).

As with the grating couplers and waveguides, the performance of the Bragg mirror cavities is largely dependent on the quality of fabrication. Rounding of the grating structures reduces their capability in acting as a stop-band filter. Equally, deviation between the dimensions of the Bragg grating design and the fabricated structure, particularly with respect to width, can shift the stop-band wavelength away from the desired frequency.

6.3 Fabrication

Fabrication includes the production of a stamp by EBL and etching followed by its imprinting into polyimide (PI) [135]. In addition to the principal component parts of the sensor outlined, modifications were included in the stamp in an attempt to aid the imprinting process. Air flow gaps were added intermittently along the cavity on the stamp used to define the waveguide. During imprinting, these gaps allow air trapped within the etched cavities to escape, enabling the polyimide to infiltrate the deeper regions of the stamp. Furthermore, all patterns were fabricated on top of a single, 10 µm high etched mesa. The purpose of the mesa is to ensure contact between the stamp and the PI is confined to the patterned regions that define the structures. Without the mesa it is conceivable that displaced PI could come into contact with the surface of the substrate and either adhere to the stamp or, due to the increased contact area, reduce the effective imprinting force. A cross sectional profile of the stamp showing the multiple etches required and a plan view of the imprinted waveguide and Bragg mirror cavity is displayed in figure 6.7.
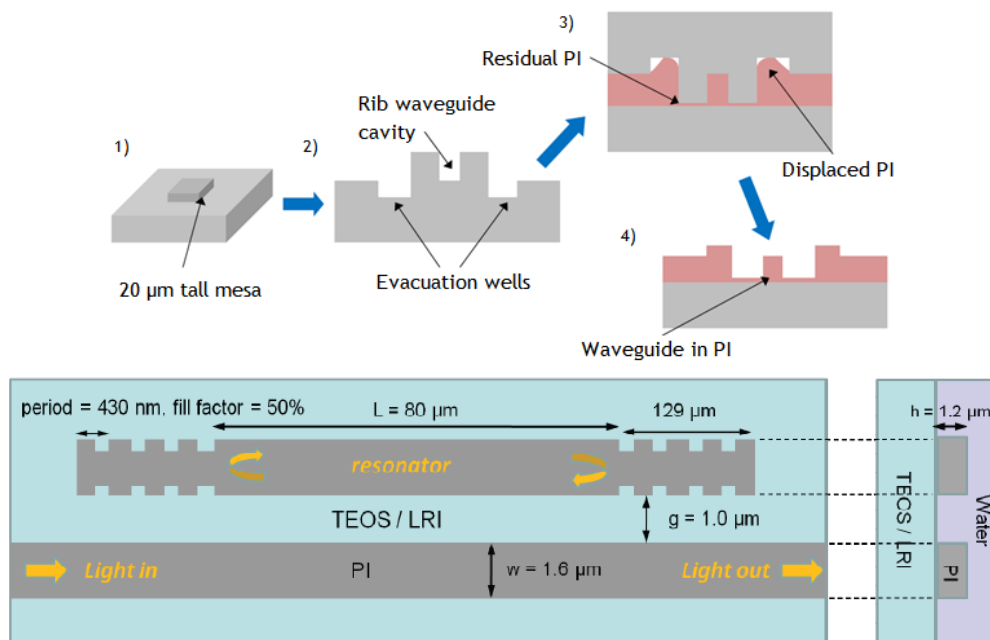
Figure 6.7: A cross-sectional diagram of the stamp and a corresponding schematic of a desired imprinted sensor [135].

Fabrication of the stamps and polymer devices was undertaken jointly with Dr Ali Z. Khokhar, University of Southampton but formerly the University of Glasgow.

6.3.1 Fabrication of stamps

Fabrication of the nanoimprint stamp was performed using EBL. Neat HSQ was spin-coated onto a silicon substrate at a thickness of 300 nm and hard-baked. The sample was exposed by electron-beam and developed in TMAH for 30 seconds at 23 ℃. Silicon etching was performed using SF_6 (sulphur hexafluoride) and O_2 plasma ICP (inductively coupled plasma), with the patterned HSQ resist acting as a mask for the grating couplers, waveguides and Bragg mirrors. As multiple exposures and etches were required to produce the three different height profiles of the stamp (three levels, excluding the substrate level), alignment markers such as those seen in chapter 3 were added to the pattern in an area far removed from the waveguides and Bragg mirror cavities. After etching the HSQ mask is removed in a buffered HF (hydrofluoric) acid solution (ratio 1:5 HF/water) for a time of 10 minutes. The completed etched Si stamps are treated in in a solution of heptane and F_{13}-OTCS for 10 minutes to create a non-stick layer, thus aiding detachment after imprinting. Micrographs of the stamp taken by SEM are shown in figure 6.8.
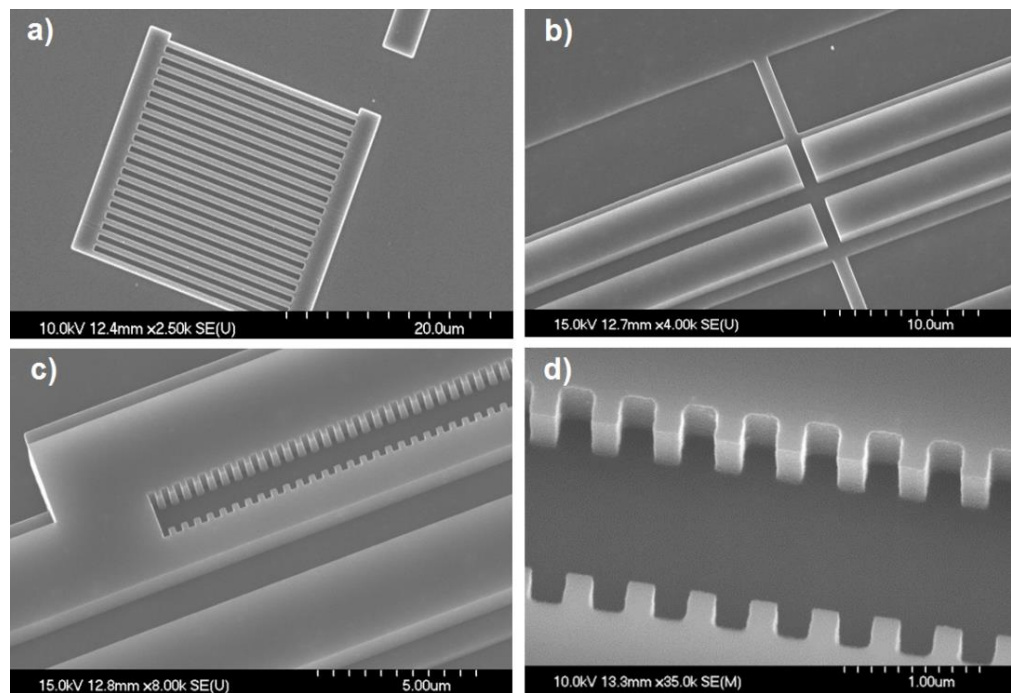
Figure 6.8: Images of the Si stamps taken by SEM. a) The grating coupler, b) section of the stamp used to define the rib waveguide, with sidewall gaps to improve the flow of the PI, c) The Bragg mirror cavity adjacent to the waveguide, d) Close-up image of the Bragg gratings.

6.3.2 Imprinted sample

The parameters used to successfully imprint a photonic sensor and the subsequent treatment of the device were discovered using a systematic fabrication approach. This involved planning for potential problems, particularly relating to the high viscosity of the P84, and introducing features that could reduce their effects, such as including air flow gaps and creating a mesa on the stamp. The fabrication recipe was produced after numerous stamps and imprints were made, in which parameters (such as imprint time, oven baking temperature etc) were changed individually as part of a set. In this way the effect of each variable condition on the sample, good or bad, can be compared systematically with other samples to ascertain the optimum parameters. Unfortunately, despite this approach no reliable and repeatable fabrication process was found. Attempts to replicate a single functional sample were unsuccessful, with the high viscosity of the polyimide and deep imprint depth required proving to be significant challenges.

This section and the remainder of the chapter will primarily focus on the photonic chip that displayed the best fabrication quality and yielded the best results of those produced. Comparisons with less successful imprints are also made.

For the target sample, 1.5 µm of P84 polyimide (PI) was spun onto silicon substrates coated with tetraethyl orthosilicate (TEOS). TEOS is used as a low index (n = 1.45) cladding material onto which the PI structures will be imprinted. It is required to have a minimum thickness of 3 µm to ensure the electromagnetic field from waves propagating along the waveguide are properly isolated from the high refractive index Si substrate. P84 is a high refractive index and highly viscous polymer. It exhibits a RI of 1.64 at 1300 nm, which can, if required, be increased to 1.74 by doping it with TiO_2 nanoparticles to increase the refractive index contrast with the surrounding materials[136-138]. In this latter case, the doped P84 must be doctor-bladed onto the TEOS rather than spun on. Doctor-blading involves physically casting (or scraping) the polyimide across the surface of the substrate. However it was found by partners at Bayer that doctor-blading this highly viscous polymer produced films of limited uniformity, making them unattractive for NIL. Doped PI is likely to introduce new challenges with regard to imprinting, such as decreased uniformity in the PI thickness and an increase in viscosity. All imprints detailed in this chapter were performed using non-doped

P84 spin coated on TEOS. The P84 PI was diluted in N-Ethyl-2-Pyrrolidone (NEP) solvent to aid the spinning and imprinting process. Following spinning the P84 polymer was lightly baked for 15 minutes at 90 ℃. The stamp was imprinted into the PI using an Obducat Nanoimprinter for 20 minutes at a pressure of 30 bar and temperature of 120 ℃. After separating the two samples the stamp could be cleaned in warm acetone for re-use. SEM images of the imprinted structures can be seen in Figure 6.9.

It was discovered that baking the P84 polymer for longer than 15 minutes at 90 ℃ caused the material to increase significantly in viscosity, making imprinting to the required depths difficult. However FTIR measurement of the P84 after the imprinting process showed that a significant quantity of NEP remained in the polymer. For reduced losses in the waveguide the solvent must be removed leaving the imprinted features in P84. This was achieved by curing the samples in a vacuum oven at 90 ℃ for 3 hours. When baked under vacuum, the PI retained its imprinted shape while the remaining solvent was evaporated from the polymer device.
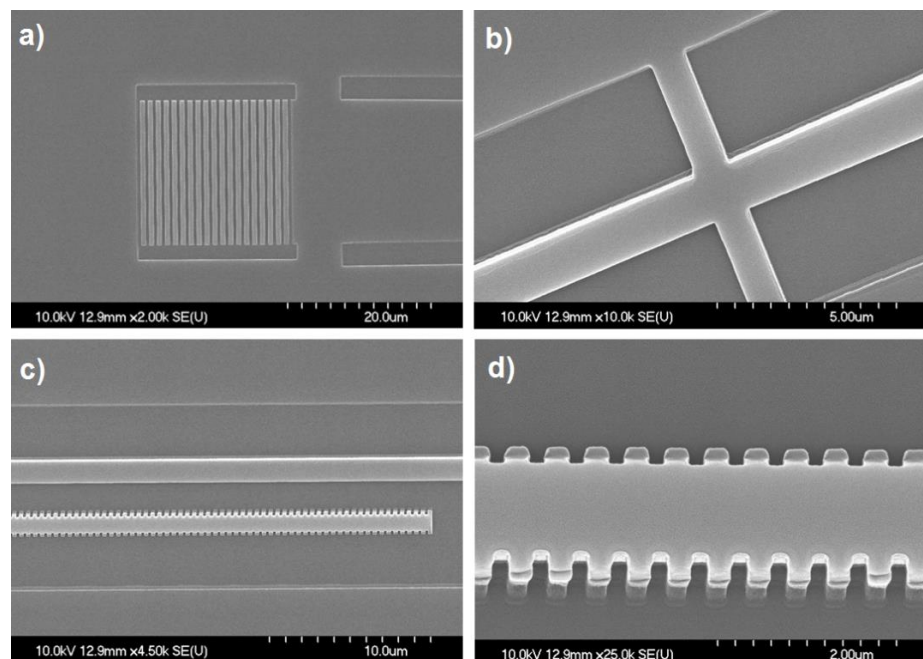
Figure 6.9: Micrographs of the imprinted structures in PI. a) An imprinted grating coupler and start of the waveguide, before tapering, b) polymer waveguide with polymer crossing due to flow gaps in the stamp. The defining trenches are seen either side of the waveguide and denote the residual PI, c) A waveguide and adjacent Fabry-Perot cavity, d) Magnified image of the Bragg gratings.

The ease at which the stamp could be imprinted into the P84 polyimide was found to be greatly dependant on the ratio of P84 to NEP. A weight ratio of 1:4 (1 part P84 to 4 parts NEP) was found to yield the best structural quality for the imprinted

patterns. Polyimide layers with a greater proportion of P84 became increasingly viscous and difficult to imprint into. This often led to waveguides with a non-uniform height and poorly defined Bragg gratings. Conversely, polyimide with an increased proportion of NEP solvent produced high quality structures but these often failed to adhere to the PI beneath and were commonly pulled off of the target sample upon release of the stamp. Micrographs of imprints performed using different ratios of P84 and NEP are shown in Figure 6.10. Although the waveguide and Bragg gratings in Figure 6.10 (a) have been imprinted using PI with 25% P84, the grating quality is poor and the imprint depth is only approximately 300 nm – insufficient for guiding light. Part (b) shows an imprint into a PI film containing 15% P84. Poor adhesion between the imprinted PI and the residual PI results in patterns being torn from the substrate and rendered useless. However it is noted that with a reduced percentage of P84 in the polymer film, the imprinted structures such as Bragg gratings and grating couplers (although detached from the substrate) more closely resemble the desired design.
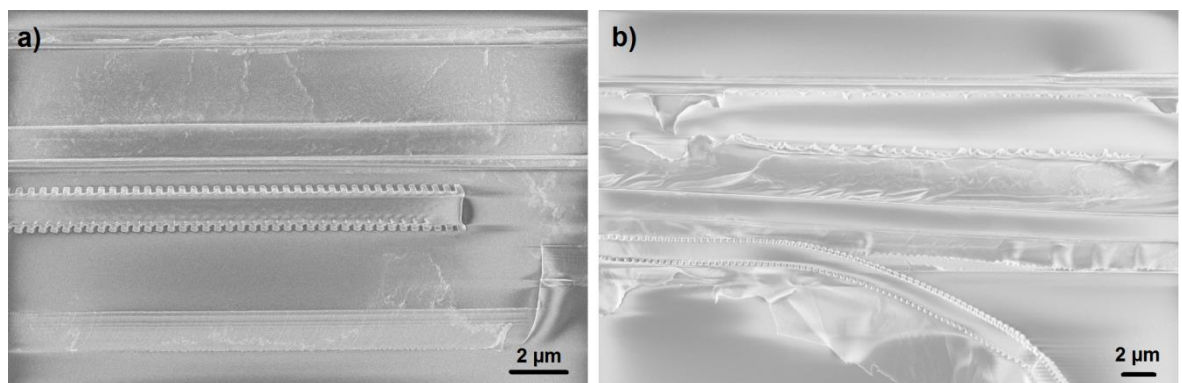
Figure 6.10: Images taken by SEM showing imprints performed using different ratios of P84 PI and NEP solvent. Bragg gratings imprinted into polyimide with a) 25% P84 and b) 15% P84 PI.

As mentioned in section 6.2, it is important that the defects in the waveguide, grating couplers and Bragg mirrors are kept to a minimum to preserve functionality and reduce losses. Because of the high viscosity of the P84 polyimide and the difficulties this can present with NIL and the post-imprint baking under vacuum, atomic force microscopy (AFM) images were taken of the structures. This was performed at the Institute for Technical Physics and Materials Science in Hungary. The AFM images are shown in figure 6.11.
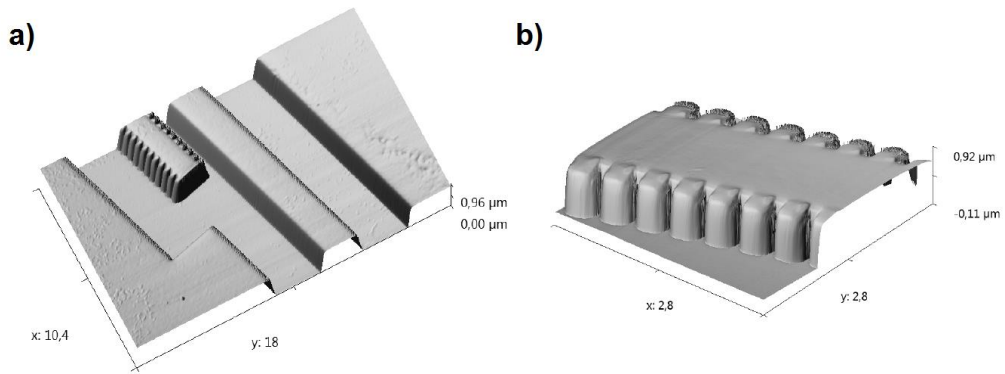
Figure 6.11: AFM images of a) an imprinted waveguide and Bragg grating and b) a Bragg grating section in closer detail. Values are given in microns.

The images in the above figure offer greater insight to the 3D shape of the imprinted structures than can be obtained using scanning electron microscopy. It is noted that the height of the waveguide and Bragg mirror cavity, ignoring the residual PI thickness, is just under 1 μm. Both the waveguide and Bragg gratings exhibit sloped sidewalls, with the imprinted PI tapering to a narrower width at the top – the area defined by the deeply etched regions on the stamp. This can chiefly be attributed to the high viscosity of the PI. It is also noted that the fill factor of Bragg mirrors (i.e. the ratio between polymer and air for a single grating period) is greater than seen on the stamp. This suggests that there is an expansion of the Bragg gratings after the nanoimprint stamp has been released from the polymer.

6.4 Results

The imprinted photonic device was characterised at Multitel, Belgium. All simulations referred to in this section were also performed at Multitel. A wavelength tunable laser source in the range 1260 nm to 1360 nm was projected at angular incidence to the photonic grating couplers. The light is output from the device at a cleaved facet of the waveguide and detected using the end-fire method. The output light is aligned to a x10 microscope objective that itself is aligned to a NIR camera. This camera is used to image the light output from the waveguide and ascertain its mode. By replacing the NIR camera with a NIR photodiode connected to an amplifier and data acquisition device, the transmitted spectrum from the waveguide can be measured. A diagram of the measurement

setup and an image of a light guided mode output from a waveguide is shown in figure 6.12.
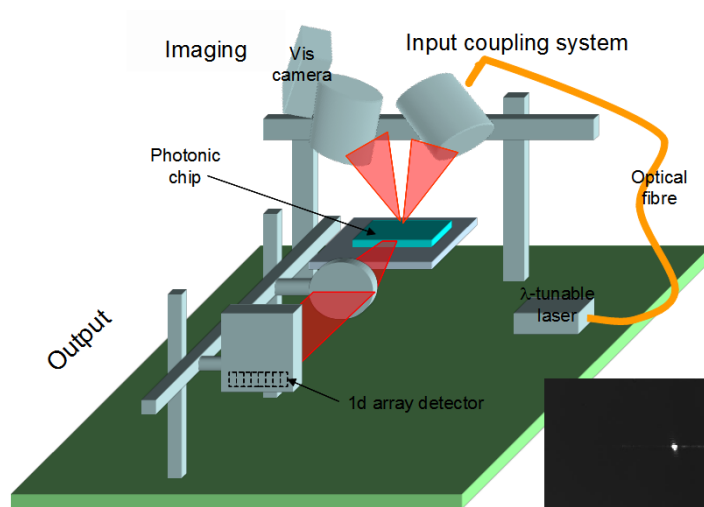
Figure 6.12: Diagram showing the experimental setup used in measuring the photonic chip. Inset, an image taken by a NIR camera showing the guided mode output from the waveguide.

The results shown in this section relate only to the functionality of one single photonic chip and its ability to couple light to the waveguide, successfully guide the light to the output end and exhibit a resonance (seen as a trough in transmission) resulting from the evanescent wave's interaction with the Bragg mirror cavity. In these measurements the sensor is not subjected to a fluidic sample or any test analytes for optical detection. If a grating coupler, waveguide and Bragg mirror cavity is defined as one single sensor, the photonic chip has seven sensors that can be measured. Sensors 1 to 4 were designed to resonate at 1310 nm and sensors 5 to 7 were designed to resonate at 1323 nm. Sensor 1 had a waveguide with width 1.36 μm, for sensors 2 to 4 this width was 1.2 μm and for sensors 5 to 7 it was 1.6 μm. Two waveguides with grating couplers but without Bragg mirror cavities were also included on the photonic chip. These devices, termed waveguide 1 and waveguide 2, enable the effects from the Bragg mirror cavities to be isolated from the grating couplers and waveguide. In this way, the losses attributed to the waveguide and grating coupler and the Bragg mirror cavity can each be quantified. The widths of waveguides 1 and 2 were measured at 1.2 μm and 1.6 μm respectively.

The transmission spectra obtained from waveguides 1 and 2, both of which are without an adjacent Bragg mirror cavity, are shown in figure 6.13.
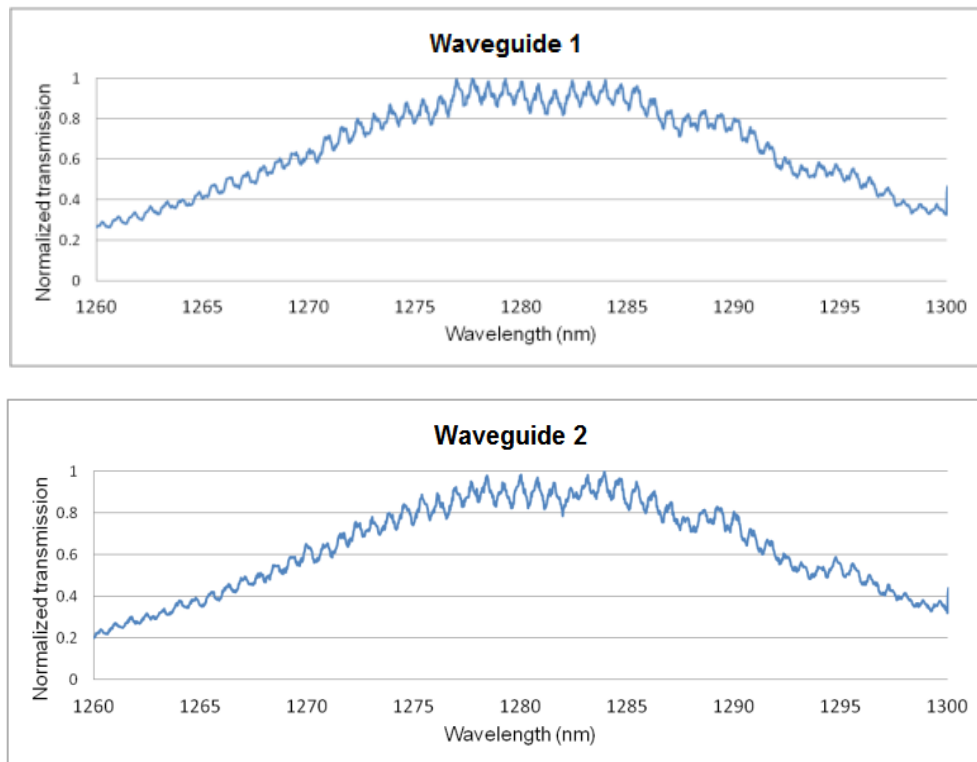
Figure 6.13: Transmission spectra from waveguides 1 and 2.

The transmission spectra from waveguides 1 and 2 enable troughs present on spectra obtained from the photonic sensors to be identified as resonances from the Bragg mirror cavity. As well as having two separate Bragg mirror designs to produce two Bragg wavelengths, the distance between the waveguide and the Bragg cavity was also varied.

Transmission spectra from the photonic sensors designed to exhibit resonance at 1310 nm and 1323 nm is shown in figure 6.14 and figure 6.15 respectively. Resonances are highlighted by an arrow on each spectrum and the measured resonant wavelength is stated inset. The distance between the fabricated waveguide and Bragg mirror cavity (gap length) is also given. It is noted that the measured resonances are in all cases typically 35 – 40 nm shorter than the Bragg wavelength expected from the design. This suggests either a change in the periodicity between the fabricated Bragg gratings and the original design or the refractive index of the P84 polyimide being lower than 1.64.

Sensor 1 λ_{Bragg} = 1270 nm Q = 16 00 Gap = 1.4 µm	
Sensor 2 λ_{Bragg} = 1272 nm Q = 1600 Gap = 1.3 µm	
Sensor 3 λ_{Bragg} = 1271 nm Q = 1600 Gap = 1.0 µm	
Sensor 4 λ_{Bragg} = 1270 nm Q = 1300 Gap = 0.7 µm	
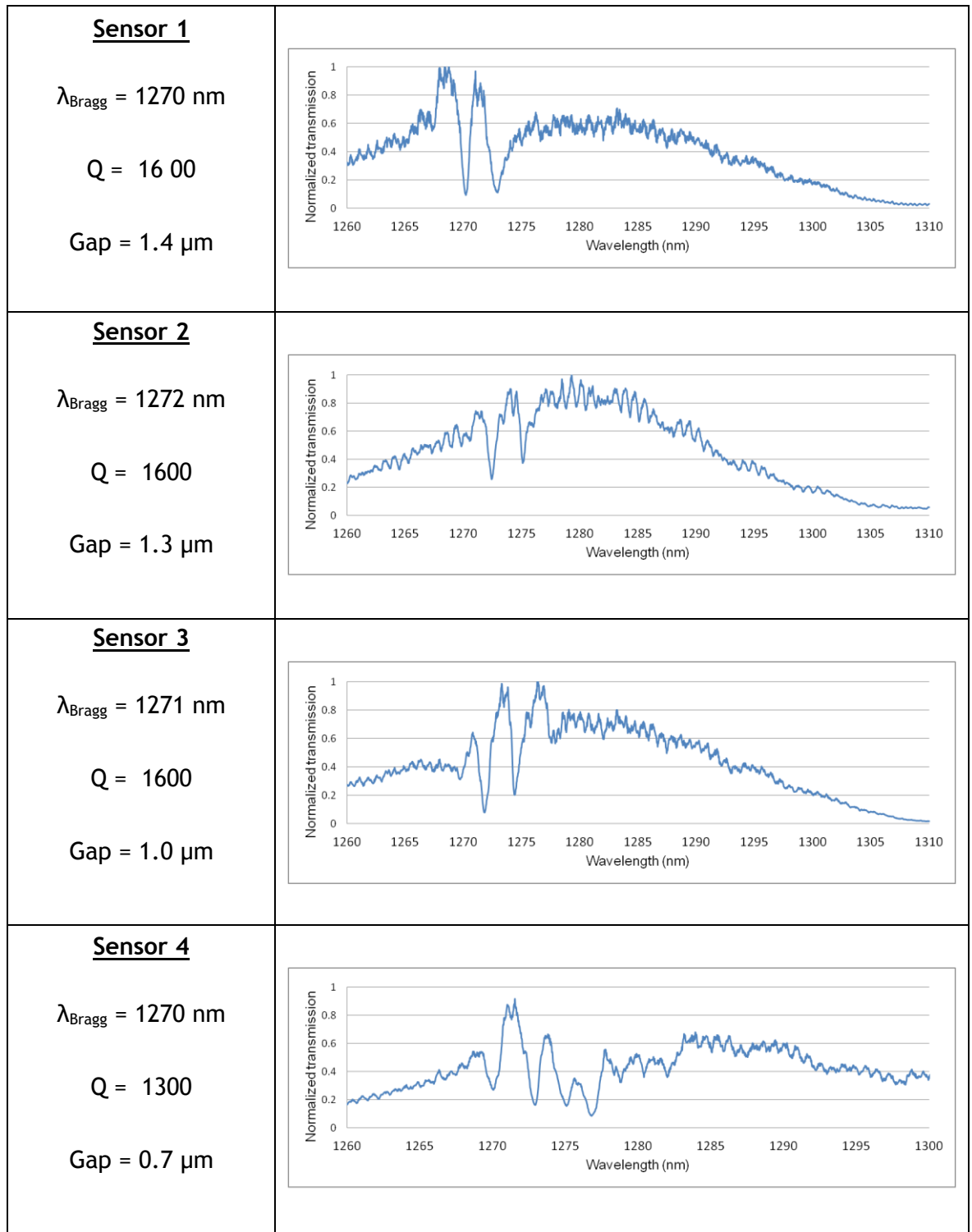
Figure 6.14: Transmission spectra from sensors designed to exhibit a resonance at 1310 nm. The primary resonant wavelength of each sensor is given alongside the gap distance between the waveguide and cavity and the calculated Q-factor.

In addition to the resonant wavelengths from the Bragg cavity red-shifting, multiple troughs are exhibited on most transmission spectra, indicating that light at more than one wavelength is reflected by the cavity. This is due to Fabry-Perot resonances from the Bragg mirror cavity. The strength and quantity of these additional resonances is seen to increase as the distance between the cavity and

the waveguide is reduced, i.e. as a greater quantity of evanescent waves are coupled to the cavity. The highest Q-factor obtained is calculated to be 4200 and is exhibited by sensor 5.

Sensor 5 λ_{Bragg} = 1287 nm Q = 4200 Gap = 1.3 μm	
Sensor 6 λ_{Bragg} = 1286 nm Q = 2600 Gap = 1.0 μm	
Sensor 7 λ_{Bragg} = 1286 nm Q = 1400 Gap = 0.7 μm	
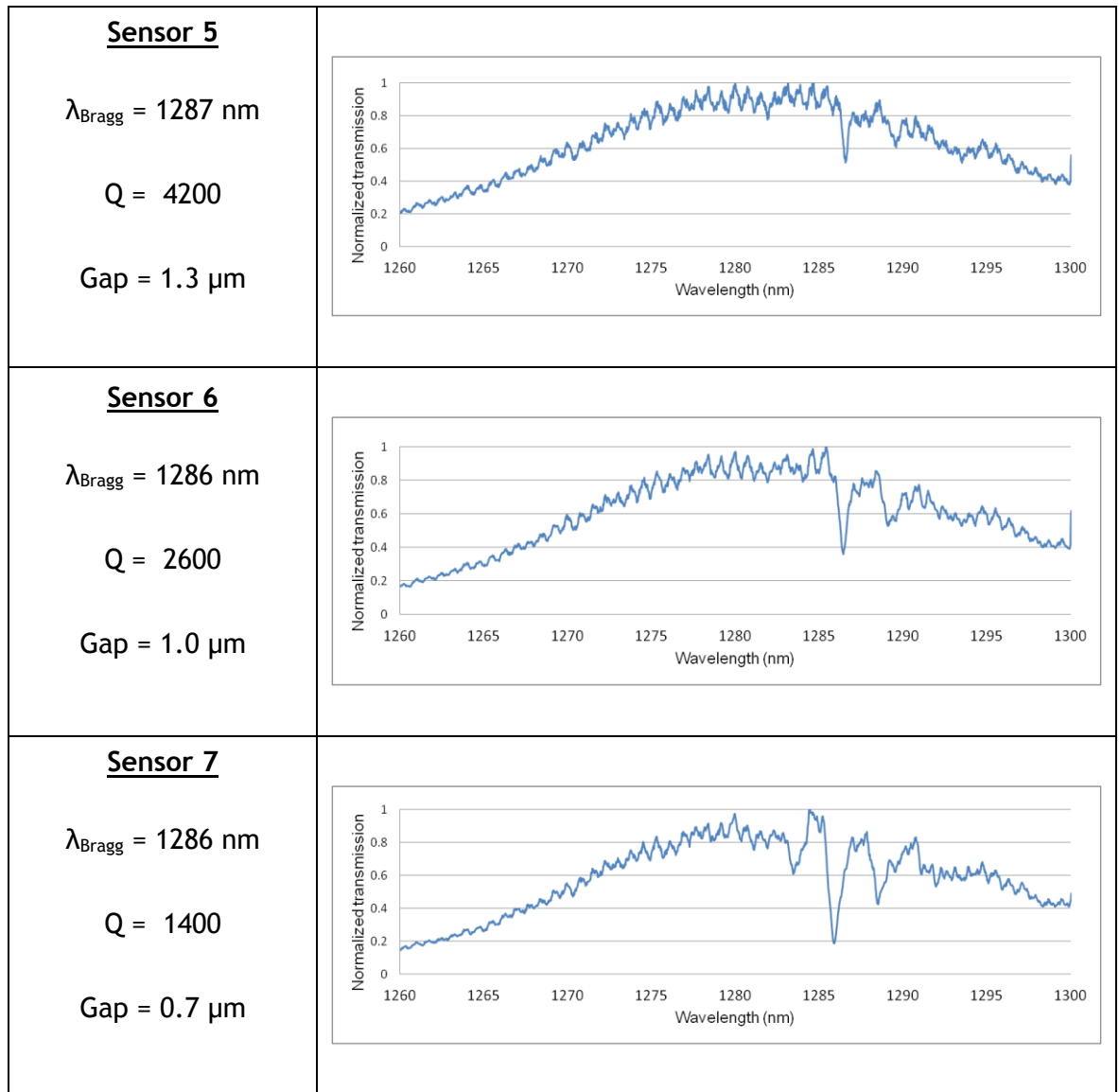
Figure 6.15: Transmission spectra from sensors designed to exhibit a resonance at 1323 nm.

A comprehensive comparison of all seven sensors is shown in table 6.1. Simulations performed at Multitel, Belgium are used in estimating losses. The total loss for each sensor varies between 31 and 33 dB, with approximately 17 dB of this being attributed to coupling light to and from the photonic chip. The losses resulting from the waveguide are calculated as 28 dB.cm^{-1}. Systematic losses include attenuation from the beam-splitter (3 dB) It should be noted that these values are obtained without any top cladding layer residing above the waveguide.

The high Q-factor exhibited by sensor 5 can be attributed to the fact that this pattern has the widest waveguide and the largest gap between the cavity and waveguide, resulting in a reduced proportion of evanescent waves coupling to the Fabry-Perot resonator. As well as using the Q-factor to gauge the effectiveness of each sensor the transmission at resonance, which can be thought of as the amount of light at the resonant wavelength that is not coupled to and reflected within the Fabry-Perot cavity, can also be considered. This value, denoted as "normalised resonance transmission" in table 6.1, gives a percentage figure of the light transmitted at the resonant wavelength.

Sensor number	Design λ (nm)	Measured λ (nm)	Design gap (μm)	Loss (dB)	Q factor	FWHM (pm)	Bus waveguide width (μm)	Normalised resonance transmission
1	1310	1270	1.4	33	1600	800	1.36	0.11
2	1310	1272	1.3	32	1600	800	1.2	0.35
3	1310	1271	1.0	33	1600	800	1.2	0.17
4	1310	1270	0.7	32	1300	1000	1.2	0.28
5	1323	1287	1.3	31	4200	300	1.6	0.625
6	1323	1286	1.0	31	2600	500	1.6	0.475
7	1323	1286	0.7	33	1400	900	1.6	0.235

Table 6.1: A comparison of the main parameters for sensors 1 to 7, indicating measured resonant wavelengths and calculated Q-factors for each.

6.5 Discussion

6.5.1 Analysis of fabricated sensors

The results obtained show seven functional sensors, with both similarities and differences between each of them. Images of the fabricated photonic chip taken by SEM and AFM show small, albeit numerous, imperfections in the sensor structures. These imperfections include a "rounding" of the waveguide sidewalls and a change in the dimensions of the Bragg gratings. In all seven sensors these defects were consistent throughout the structure and not sporadic. Although

fabrication imperfections are unavoidable, in this instance they are likely contributing factors to a shift in the Bragg wavelength, losses within the waveguide and a limited Q-factor. In all cases the measured wavelength of resonance was approximately 35 to 40 nm shorter than expected from the design. This leads to the conclusion that the shift is caused by either the change in the periodicity of the gratings or the P84 PI having a refractive index less than 1.64. Ideally, further refinement of the imprinting process would reduce the extent of the defects and improve the performance of the device. However if the polyimide were to prove too viscous in attempts to reduce the rounding and change in size of structural features, this deviance could be considered during the design stage and the nanoimprint stamp altered accordingly.

It is noted that the normalised resonance transmission decreases as the cavity and waveguide are moved closer together. This is particularly evident in sensors 5, 6 and 7 which have a waveguide width of 1.6 μm. Wider waveguides are used to support the propagation of light at longer wavelengths. As the evanescent waves decay exponentially as the distance from the waveguide boundary increases, fewer waves will couple to the Bragg gratings. With reduced coupling, the normalised transmission at resonance for sensor 5 is measured at 62.5% compared to 23.5% for sensor 7, in which the waveguide and cavity are 600 nm closer. With the cavity in close proximity to the waveguide boundary a greater proportion of evanescent waves are coupled to and reflected within the resonator, making the sensor more efficient at reducing transmission at resonant wavelengths. This reduction in transmission is also evident when comparing sensors 2 and 4, which have a waveguide width of 1.2 μm and a resonance transmission of 35% and 28% respectively. As with sensors 5 and 7 the change in distance between the waveguide and cavity is 600 nm.

The prevalence of additional resonances is also increased as the distance between the Fabry-Perot cavity and waveguide is reduced. Again, this can be attributed to a greater proportion of the evanescent waves of light (at more than one wavelength) being reflected within the adjacent cavity. Four troughs are seen in the transmission spectrum obtained from sensor 4, compared to three from sensor 3 and two from sensor 2. Equally for the three sensors with a primary resonance

at 1323 nm, additional resonances are more prominent in the transmission spectrum from sensor 7 than sensors 5 and 6.

While the FWHM and Q-factor remains constant for sensors 2, 3 and 4, it is seen to change significantly for sensors 5, 6 and 7. The sensor with the lowest amount of coupling between waveguide and cavity, sensor 5, exhibits the narrowest FWHM at 300 pm. This results in a Q-factor of 4200. As this coupling increases, signified by a decrease in distance between the waveguide and cavity, the Q-factor is seen to decrease. This is shown in figure 6.16, in which the Q-factor is plotted against the gap length.
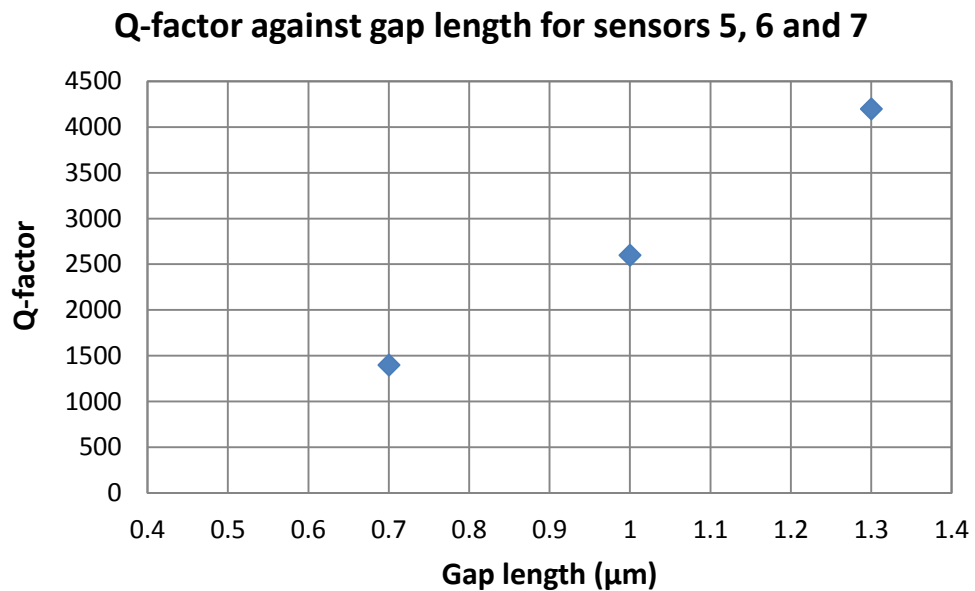
Figure 6.16: Q-factor against gap length for sensors 5, 6 and 7.

Losses for the sensors varied between 31 dB and 33 dB. Simulations suggest coupling tight to and from the photonic chip and systematic attenuation account for 17 dB of the total losses. For the waveguide, a loss per unit distance value of 28 dB.cm^{-1} is obtained. AFM scans of the imprinted waveguides and cavities show that their thickness falls approximately 200 nm below the designed value of 1200 nm. As a consequence the polymer slab beneath the rib waveguide is thicker than what would be considered optimum. Imprinting the stamp deeper into the polymer would correct this deficiency in the waveguide thickness and reduce the losses obtained from them.

6.5.2 Comparison with other existing sensors

The capability of the photonic polymer sensors cannot truly be gauged until it is characterised by sensing a fluidic sample. However simulations of sensor 7, which yielded the highest Q-factor, suggest a bulk sensitivity of 37 nm/RIU. This is obtained from simulations modelled using dimensions obtained from the fabricated structure by SEM and AFM, not the idealised design. The surface sensitivity, distinguishable from the bulk sensitivity, is also found by way of simulation to be 0.05 pm/pg mm^{-2}. Defining the figure of merit as the ratio of the sensitivity to the limit of detection:

$$FOM = s/FWHM \qquad\qquad\qquad\qquad (6.11)$$

$$FOM = s\left(\frac{Q}{\lambda}\right) \qquad\qquad\qquad\qquad (6.12)$$

For sensor 7, the bulk FOM = 37(4200/1310) = 118 nm/RIU and the surface FOM = 5x10^{-5}(4200/1310) = 1.6x10^{-4} (pg/mm^2)$^{-1}$. These estimations apply a resonant wavelength of 1310 nm and do not consider any change in the Q-factor when the sensor is brought into contact with water. With water applied to the surface of the polymer the scattering of waves will differ than in air, potentially lowering the Q-factor.

Cattoni et al [139] reported Localised surface plasmon resonance (LSPR) sensors, fabricated using NIL, exhibiting a sensitivity of 405 nm/RIU. Slot waveguide resonators used as a comparable biochemical sensor have been shown (with fluidic analyte) to exhibit a sensitivity of 212 nm/RIU and a Q-factors of 1800 [140].

6.6 Chapter conclusions

The results obtained show that a functioning grating coupler, waveguide and Bragg mirror based Fabry-perot cavity can be fabricated in a high index polymer using nanoimprint lithography as a production technique. However the reliability of the NIL process proved problematic. Despite numerous attempts it was found that the fabrication of functioning polymer sensors was not easily reproducible and imprinted structures were often not thick enough or lacked well-formed Bragg gratings. From the most successful photonic chip, resonances measured

experimentally were seen at wavelengths approximately 40 nm shorter than predicted by simulations. This is due to imperfections in the fabricated structures, namely a change in critical dimensions, which effect the operation of the device. The highest Q-factor obtained was 4200 from sensor 7. The characterisation performed involved only dry characterisation. In order for the sensor to be characterised fully it must be tested with a fluidic sample for the detection of analytes. Water absorption of the polymer and delamination of the micro-fluidic channel from the substrate proved problematical. A possible solution is the coating of the polymer in a thin atomic layer deposited film of TiO_2. Further work in improving the imprint depth of the stamp and minimising structural defects would reduce bulk losses. For this to be achieved alternative polyimides that exhibit a lower viscosity could be considered. With a likely change in the refractive index, use of a different polymer would require changes to the sensor design and NIL stamp.

Acknowledgements

Chapter 7

Future work, summary and conclusions
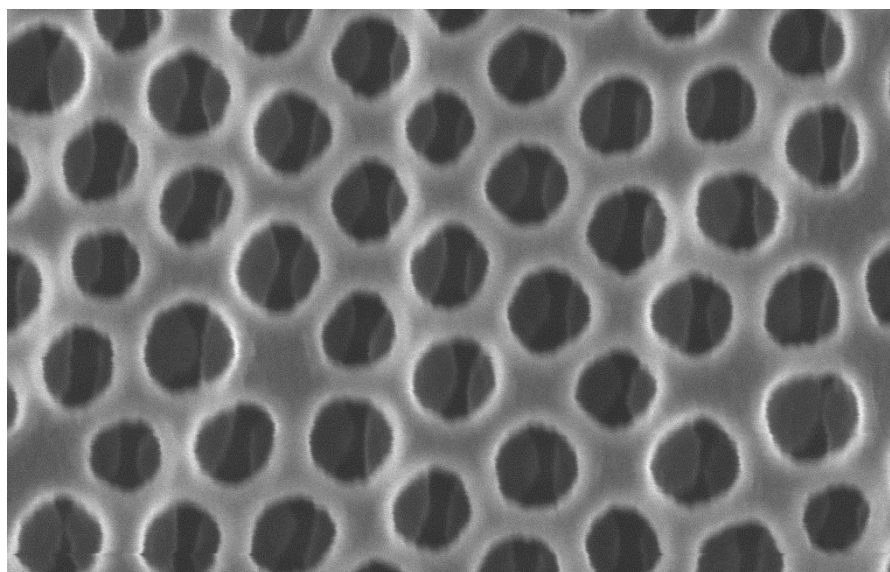
7.1 Introduction

This chapter covers incomplete and ongoing work pertaining to that discussed in previous chapters, meaning it cannot be comprehensively analysed to the same extent. Nonetheless this section aims to provide additional insight into the techniques and concepts covered as well as demonstrating their potential benefits. Conclusions regarding all of the work discussed in this thesis are also made. The outcomes are compared and contrasted with the aims and objectives specified in the thesis introduction.

7.2 Future work

7.2.1 Improved resonance coupling between PMMA and SRRs

In order to fully understand the limitations of the SRR sensors with localised PMMA detailed in chapter 4, additional work can be undertaken. Firstly, a redesign of the SRR geometry can be performed to better match a plasmonic or LC resonance to that of the carbonyl absorbance feature seen at 5.75 μm. This may improve the resonance coupling between the two components. A study using a number of different geometries, such as a variation in the ring diameter, would also provide insight into the relationship between resonance coupling and sensitivity. In a similar vein, variation in the symmetry of the SRR by changing the width of the split would provide additional experimental information regarding the dependence of symmetry on the sensitivity.

7.2.2 Pattern transfer of nanoimprinted fishnets

It has been shown that the presence of a substrate beneath a fishnet metamaterial has significant repercussions on the optical performance of the structure during characterisation [141]. A substrate, usually only used as a means to support the fishnet during fabrication, introduces bianisotropic effects that hamper the metamaterial's ability to function as a negative index material as well as reducing optical transmission. The ability to physically separate a fabricated structure from its substrate and move it to another, occasionally refered to as "pattern transfer", can lead to an improvement in material performance as well as providing new opportunities with regard to their potential application. It can also be the case that the separated pattern is simply removed from the supporting substrate and

then used on its own, without transferring it to another substrate. This has previously been demonstrated using a fishnet metamaterial, which is removed from the substrate and can be suspended in air [98].

Using the nanoimprint technique demonstrated in Chapter 5, work has been undertaken in attempting to detach the imprinted fishnet from the substrate and polymer it sits on. Upon detachment, the metamaterial could then be placed on a second, separate substrate or suspended in air for characterisation. The motivation for this is twofold. Firstly, the fused quartz substrate and PMMA used in the experiment are only required during fabrication and contribute to optical losses, a reduced magnitude of the refractive index real part and a narrower negative index wavelength range. Removal of the fishnet from the polymer beneath will also negate the effect of the nano-pillars that are pushed downwards during imprinting. Secondly, the transferring the fishnet to an alternative substrate, or none at all, can create new possibilities with regard to any characterisation or application of the fishnet. For example, flexible fishnets on a polydimethylsiloxane (PDMS) substrate have been proposed for operation at terahertz frequencies [105]. Other metamaterials have also been demonstrated to function on flexible substrates, such as Metaflex [142]. Furthermore, a metamaterial fishnet sheet has the potential to be applied to substrates or structures that are rounded or uneven.

As a means to detach the metal-dielectric-metal fishnet so that it can be handled on its own and transferred to another substrate the combined fishnet, polymer and nano-pillar structure was gently submerged in a petri dish of acetone. Although this dissolved the PMMA layer, it was found that the fishnet structure regularly broke into smaller fragments and failed to remain intact. This is likely the result of the rapid removal of the PMMA, causing the thin metal and dielectric layers on top to crack when unsupported, in a similar fashion to the metal "lift-off" process. Unrelated work into fabricating metamaterials using the self-assembly features of colloidal lithography have demonstrated the transfer of thin metal layers using a sacrificial film of polyacrylic acid (PAA) [143]. As PAA is soluble in water, depositing a metal film on top of a PAA layer means that it can float free of the substrate when gently submerged in water. Therefore, a 1 µm thick layer of PAA diluted in water rather than PMMA can be spun onto the

substrate and the Ag, MgF$_2$, Ag layers deposited and sample imprinted as before. In order to aid the infiltration of the water into the PAA layer, an unpatterned corner of the metal layer can be carefully scratched away. By gently dipping the sample in and out of the water the imprinted fishnet separates from the substrate at floats on the surface of the water. Placing a new substrate beneath it and then lifting it out so that the imprinted pattern is positioned on top completes the pattern transfer process. This is shown in figure 7.1. Similar work that involves the physical transfer or movement of thin metal films shows that they can be distorted and bent in a range of different positions before breaking [142]. This can include tuneable-metamaterials, in which the optical characteristics of the metamaterial can be varied by, for example, exerting stress on the substrate [144]. This typically involves changing certain dimensions of the fabricated structures, namely the gap length between separate metal features.
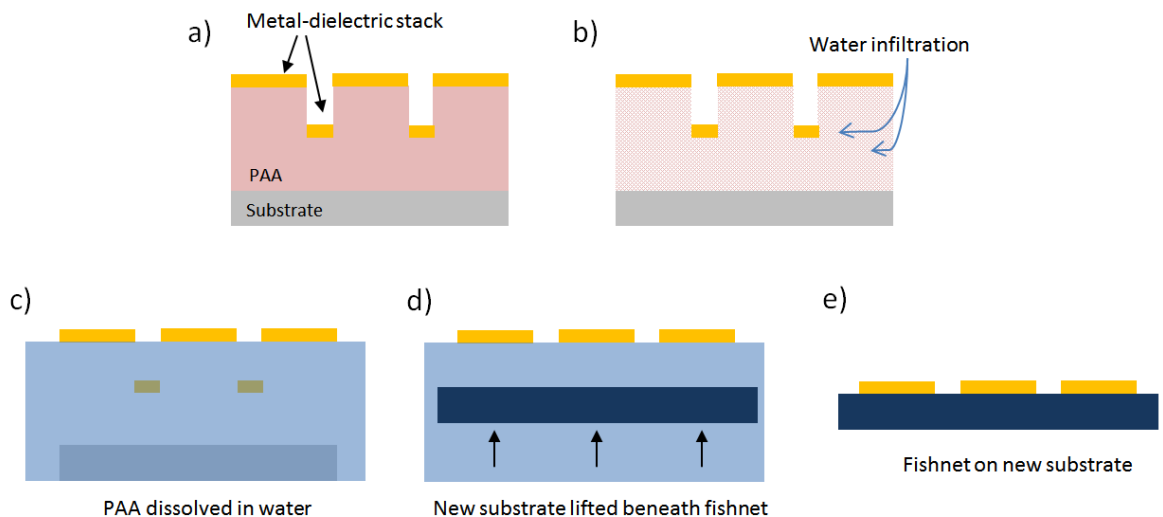
Figure 7.1: Potential process for the transfer of an imprinted fishnet onto another substrate. (a) The fishnet is imprinted on top of a PAA layer, (b) the sample is submerged in water which (c) dissolves the PAA, (d) a new substrate is lifted from beneath the now floating or suspended fishnet to (e) complete the pattern transfer.

For the purposes of experimentally characterising the fishnet in air, it is feasible that the structure be transferred onto a substrate with single or multiple holes, allowing it to be suspended in air. This enables the fishnet to be characterised without a conjoining substrate (for comparison with a substrate). This is of particular benefit in performing angular resolved reflection and transmission measurements with the aim of experimentally determining the refractive index [145,80].

Further experimentation regarding the number of active layers that can be imprinted into is also advantageous. While increasing the number of metal and dielectric layers in a fishnet can increase the magnitude of the real part of negative refractive index, an increase in the total thickness of metal and dielectric is likely to be more difficult to imprint into. This could perhaps be overcome by using an increased imprint force, but this itself may introduce problems with regard to the lifetime of the nanoimprint stamp and the durability of the target substrate, as well as a reduction in pattern quality. Experimentation with an increase in the number of active layers could provide information relating to the limitations of the fabrication technique. Optimising the thickness of each metal and dielectric layer could aid this process.

7.3 Chapter summaries

Chapter 1

A general introduction to fundamental aspects of electromagnetic wave theory, optics and photonics is given in chapter 1. This gives background information relating to the operation of devices described in subsequent chapters. The aims and objectives of the thesis are stated.

Chapter 2

This chapter details the fabrication lithographies and measurement techniques used in producing and characterising the structures and devices presented. While specific fabrication recipes are included in each relevant chapter, the background theory and operating principles of electron-beam lithography and nanoimprint lithography are given here. This includes the advantages and disadvantages of both lithographies and their potential effect on the small-scale structures similar to those included in this thesis. Information relating to the dry etching of materials is also given. Additionally, the FTIR and monochromator scanning spectroscopy measurement setups used to characterise the fabricated structures are detailed in this chapter.

Chapter 3

Small-scale SRRs, with a total structure width ranging from 70 nm to 110 nm, are fabricated using a novel NIL technique that involves an "etch-free" stamp

production process. This enables high-resolution metamaterial structures, with a minimum feature size of 20 nm, to be fabricated over a large area in a short period of time. The SRRs, fabricated on a silicon substrate, were found to give a LC resonance at near-infrared frequencies. The limitations of scaling and the effect of the conductor (metal) thickness are studied. This includes a reduced Q-factor owing to a metal thickness of 15 nm compared to a 50 nm thickness for SRRs patterned by EBL. While high quality, small-scale features can be imprinted and metalised, the inability to create an undercut profile in the resist and hence deposit thicker layers of metal can be viewed as a limiting factor of the process. A Q-factor of 11.1 is calculated from the experimental measurements obtained from the SRRs fabricated by NIL. However a reduced resonant peak amplitude significantly limits the SRRs usefulness in optical sensing.

Chapter 4

In this chapter the sensitivity of various physical regions of a SRR are studied using PMMA as an organic probe. With a square block of PMMA localised at a number of locations on or near SRRs, the regions of the metamaterial most sensitive to detecting an analyte (where the electric field strength is strongest) can be ascertained experimentally. Simulations validate the experimental findings and the sensitivity of the SRR for each PMMA location is calculated. The SRRs sensitivity to the localised PMMA was found to be greatest when it was positioned at the gap with the incident electric field creating a current loop in the structure. This resulted in a sensitivity value of 612 nm/RIU. PMMA positioned on the end of the SRR arm with an unchanged polarisation resulted in a sensitivity of 388 nm/RIU being calculated. A 100 nm thin film covering the entire SRR unit cell gave a sensitivity value of 776 nm/RIU. While a thin film of PMMA cannot be used to determine the sensitivity "hot-spots" of the SRR, it does however demonstrate that, for the purposes of sensing, there are significant advantages to completely covering the metamaterial in an analyte. As well as that the comparative ease at which a film can be applied to the sample, the increased quantity of analyte (compared to a localised analyte) produces a greater spectral shift in wavelength and stronger molecular features.

Chapter 5

Nanoimprint lithography is utilised to quickly produce fishnet metamaterials by "cutting" into stacked thin films of metal and dielectric. This technique negates some of the fabrication difficulties and defects presented by more commonly used focused-ion beam etching and EBL methods. The presence of nanopillars resulting from the imprinting of the metal and dielectric thin film stack are investigated and found to produce a plasmonic response at visible frequencies. Optical transmission through the structure (substrate, PMMA layer, nanopillars and fishnet) was experimentally found to range between 40% and 60% at resonance, depending on the physical dimensions of the pattern. The phenomenon of extraordinary optical transmission is thought to enhance the transmission of light through the subwavelength apertures of the fishnet. The optical transmission and reflection are studied experimentally and the wavelength dependant refractive index of the structure is estimated using simulations that complement the experimental measurements. Of the imprinted designs, structure A is estimated to exhibit a negative refractive index real part with a maximum magnitude of 0.57, compared to 1.5 for structure B. Simulations of just the fishnet, without the supporting materials beneath, suggest these values can increase in magnitude to -4 and -5 respectively. The estimated FOM for a detached fishnet is 2.49 for fishnet A and 2.74 for fishnet B. With a layer of PMMA beneath the fishnet and nanopillars residing below the apertures, the metamaterial was found to be non-reciprocal when measuring transmission and reflection. This is best exhibited in the experimental measurements of structure C, which shows strong enhancement of the CH2 asymmetric stretch vibration at 3.3 μm. The imprint technique is proposed as having potential for use in transfer patterns onto different substrates.

Chapter 6

This chapter studies the fabrication of polymer photonic sensors using nanoimprint lithography, as part of the P3SENS project. Concentration is given to the work completed at the University of Glasgow in imprinting into a high-index, highly viscous polymer. Difficulties in the work are highlighted and techniques to overcome them suggested and considered. A comparison is made between the sensing capabilities of the Bragg mirror type sensor fabricated and that of other sensors. Results from experimental transmission measurements give Q-factors of

between 1400 and 4200, depending on the sensor dimensions, and typical waveguide losses of 28 dB per cm. Imprinting into a lower viscosity polymer may improve the achievable imprint depth and pattern quality, but would likely suffer from a lower refractive index resulting in a reduced refractive index contrast with the cladding layers.

7.4 Conclusions from Thesis

The work contained within this thesis aimed to study optical sensors operating at visible and near-infrared frequencies. An emphasis is given to the experimental fabrication and characterisation of these sensors, specifically the use of nanoimprint lithography as a means of production. Sensors studied include metamaterial resonators (split-rings and fishnets) and a photonic Bragg mirror and waveguide configuration. The optical behaviour of the structures is modelled using computer simulation and, where the electric field distribution is of interest, field plots are generated from these.

The work presented in this thesis shows that nanoimprint lithography can be a valuable technique in the fabrication of optical sensors, both metamaterial and otherwise. The optical characteristics of the structures fabricated are compared with similar structures produced using alternative techniques. In addition to this the sensitivity of specific locations of a split ring resonator were experimentally established by probing using localised PMMA (by means of EBL). This demonstrated numerous "hot-spots" and "cold-spots" and suggests that multiple regions of the structure can, to varying amounts, be used to sense the analyte.

For metamaterials and other optical sensors to make the transition from a research environment to a functional application, their production must be cheap, quick and reliable while maintaining desirable sensing capabilities. Nanoimprint lithography can be considered as a process with the potential to fulfil these criteria.

References

1. R.A. Shelby, D. R. Smith, S. Schultz. "Experimental verification of a negative index of refraction," Science, 292, 5514, 77-79 (2001).

2. J. B. Pendry, "Negative refraction makes a perfect lens." Phys. Rev. Lett., 85(18) 3966 (2000).

3. D. Schurig, J. J. Mock, B. J. Justice, S. A. Cummer, J. B. Pendry, A. F. Starr, D. R. Smith, "Metamaterial electromagnetic cloak at microwave frequencies", Science 314, 5801, 977-980 (2006).

4. N. I. Landy, S. Sajuyigbe, J. J. Mock, D. R. Smith, W. J. Padilla, "Perfect metamaterial absorber", Phys. Rev. Lett. 100(20) 207402 (2008).

5. V. M. Shalaev, "Optical negative-index metamaterials", Nature Photonics, 1(1) 41-48 (2007).

6. F. J. Levi, "Applied Quantum Mechanics", Cambridge University Press (2006).

7. V.G. Veselago, "The electrodynamics of substances with simultaneously negative values of ϵ and μ", Physics-Uspekhi, 10(4), 509-514 (1968).

8. G. V. Naik, V. M. Shalaev, A. Boltasseva, "Alternative Plasmonic Materials: Beyond Gold and Silver", Advanced Materials, 25(24), 3264–3294 (2013).

9. V. Kildishev, A. Boltasseva, V. M. Shalaev, "Planar Photonics with Metasurfaces", Science 339, 6125 (2013).

10. C. F. Bohren, D. Huffman, "Absorption and Scattering of Light by Small Particles", John Wiley & Sons (1983).

11. K. L. Kaiser, "Electromagnetic Shielding", CRC Press (2005).

12. V. M. Rotello, "Nanoparticles: Building Blocks for Nanotechnology", Springer (2004).

13. J. L. Santos, F. Farahi, "Handbook of Optical Sensors", CRC Press (2014).

14. F. Capolino, "Applications of Metamaterials", CRC Press (2009).

15. Q. Gong, X. Hu, "Photonic Crystals: Principles and Applications", CRC Press (2014).

16. J. M. Lopez-Higuera, "Optical Sensors", Universidad de Cantabria (1998).

17. Z. Cui, "Nanofabrication: Principles, Capabilities and Limites", Springer (2009).

18. W. Menz, J. Mohr, O. Paul, "Microsystem Technology", John Wiley & Sons (2008).

19. Y. Nishi, R. Doering, "Handbook of Semiconductor Manufacturing Technology", CRC Press (2007).

20. S. Y. Chou, P. R. Krauss, P. J. Renstrom. "Nanoimprint lithography", Journal of Vacuum Science & Technology B, 14(6), 4129-4133 (1996).

21. L. J. Guo, "Nanoimprint lithography: methods and material requirements", Advanced Materials 19(4), 495-513 (2007).

22. H. Schift, "Nanoimprint lithography: an old story in modern times? A review ", Journal of Vacuum Science & Technology B 26(2), 458-480 (2008).

23. M. Beck, M. Graczyk, I. Maximov, E. L. Sarwe, T. G. I. Ling, M. Keil, L. Montelius, "Improving stamps for 10 nm level wafer scale nanoimprint lithography", Microelectronic Engineering, 61, 441-448 (2002).

24. S. H. Ahn, L. J. Guo. "High-Speed Roll-to-Roll Nanoimprint Lithography on Flexible Plastic Substrates." Advanced materials 20(11) 2044-2049 (2008).

25. D. W. Sun, "Infrared Spectroscopy for Food Quality Analysis and Control", Academic Press (2009).

26. Z. M. Wang, "One-Dimensional Nanostructures", Springer (2008).

27. I. Wolff, "Microstrip bandpass filter using degenerate modes of a microstrip ring resonator", Electronics Lett. 8 (12), 302-303 (1972).

28. W. N. Hardy, L. A. Whitehead, "Split-ring resonator for use in magnetic resonance from 200-2000 MHz", Rev. Sci. Instrum. 52, 213 (1981).

29. D. R. Smith, Willie J. Padilla, D. C. Vier, S. C. Nemat-Nasser, S. Schultz, "Composite Medium with Simultaneously Negative Permeability and Permittivity", Phys. Rev. Lett. 84, 4184 (2000).

30. J. B. Pendry, A. J. Holden, D. J. Robbins, and W. J. Stewart, "Magnetism from Conductors and Enhanced Nonlinear Phenomena", IEEE Trans. Microwave Theory Tech. 47, 2075 (1999).

31. R. A. Shelby, D. R. Smith, S. Schultz, "Experimental Verification of a Negative Index of Refraction", Science 292, 77-79 (2001).

32. S. Linden, C. Enrich, M. Wegener, J. Zhou, T. Koschny, C. M. Soukoulis, "Magnetic Response of Metamaterials at 100 Terahertz", Science 306, 1351-1353 (2004).

33. S. Tretyakov, "On geometrical scaling of split-ring and double-bar resonators at optical frequencies", Metamaterials 1, 40-43 (2007).

34. M. W. Klein, C. Enrich, M. Wegener, C. M. Soukoulis, S. Linden, "Single-slit split-ring resonators at optical frequencies: limits of size scaling", Opt. Lett. 31, 1259-1261 (2006).

35. C. Rockstuhl, F. Lederer, C. Etrich, T. Zentgraf, J. Kuhl, and H. Giessen, "On the reinterpretation of resonances in split-ring-resonators at normal incidence", Opt. Exp. 14 (19), 8827–8836 (2006).

36. B. Lahiri, S. G. McMeekin, A. Z. Khokhar, R. M. De La Rue, N. P. Johnson, "Magnetic response of split ring resonators (SRRs) at visible frequencies", Opt. Exp. 18 , 3210-3218, (2010).

37. J. Zhou, T. Koschny, M. Kafesaki, E. N. Economou, J. B. Pendry, C. M. Soukoulis, "Saturation of the Magnetic Response of Split-Ring Resonators at Optical Frequencies", Phys. Rev. Lett., 95, 223902 (2005).

38. D. E. Apnes, A. A. Studna, "Dielectric functions and optical parameters of Si, Ge, GaP, GaAs, GaSb, InP, InAs, InSb from 1.5 to 6.0 eV", Phys. Rev. B. 27, 985-1009 (1983).

39. Z. Sheng, V.V, Varadan, "Tuning the effective properties of metamaterials by changing the substrate properties", J. Appl. Physics. 101, 014909 4-7 (2007).

40. L. Gao, L. Lin, J. Hao, W. Wang, R. Ma, H. Xu, J. Yu, N. Lu, W. Wang, L. Chi, "Fabrication of split-ring resonators by tilted nanoimprint lithography", J Colloid Interface Sci. 360, 320-323 (2011).

41. T. Tomioka, S. Kubo, M. Nakagawa, M. Hoga, T. Tanaka, "Split-ring resonators interacting with a magnetic field at visible frequencies", Appl. Phys. Lett. 103, 071104 (2013).

42. E. D. Palik, ed. "Handbook of optical constants of solids". Vol. 3, Academic Press (1998).

43. Y. Liu, X. Zhang, "Metamaterials: a new frontier of science and technology", Chem. Soc. Rev. 40, 2494-2507 (2011).

44. L. Zhao, K. L. Kelly, G. C. Schatz, "The Extinction Spectra of Silver Nanoparticle Arrays: Influence of Array Structure on Plasmon Resonance Wavelength and Width", J. Phys. Chem. B. 107(30) 7343-7350 (2003).

45. J. O'Hara, R. Singh, I. Brener, E. Smirnova, J. Han, A. Taylor, W. Zhang, "Thin-film sensing with planar terahertz metamaterials: sensitivity and limitations", Opt. Express, 16, 1786-1795 (2008).

46. B. Lahiri, A. Z. Khokhar, R. M. De La Rue, S. G. McMeekin, N. P. Johnson, "Asymmetric split ring resonators for optical sensing of organic materials", Opt. Express, 17, 1107-1115 (2009).

47. I. M. Pryce, Y. A. Kelaita, K. Aydin, H. A. Atwater, "Compliant Metamaterials for Resonantly Enhanced Infrared Absorption Spectroscopy and Refractive Index Sensing", ACS Nano, 5 (10), 8167–8174 (2011).

48. X. Xu, B. Peng, D. Li, J. Zhang, L. M. Wong, Q. Zhang, S. Wang, Q. Xiong, "Flexible Visible–Infrared Metamaterials and Their Applications in Highly Sensitive Chemical and Biological Sensing", Nano Lett. 11 (8), 3232-3238 (2011).

49. H. J. Lee, J. H. Lee, H. S. Moon, I. S. Jang, J. S. Choi, J. G. Yook, H. I. Jung, "A planar split-ring resonator-based microwave biosensor for label-free detection of biomolecules", Sensors and Actuators B: Chemical, 169, 26-31 (2012).

50. A. V. Kabashin, P. Evans, S. Pastkovsky, W. Hendren, G. A. Wurtz, R. Atkinson, R. Pollard, V. A. Podolskiy, A. V. Zayats, "Plasmonic nanorod metamaterials for biosensing", Nature Materials, 8, 867 - 871 (2009).

51. B. Lahiri, G. Holland, V. Aksyuk, A. Centrone, "Nanoscale Imaging of Plasmonic Hot Spots and Dark Modes with the Photothermal-Induced Resonance Technique", Nano Lett. 13 (7), 3218-3224 (2013)

52. C. Rockstuhl, F. Lederer, C. Etrich, T. Zentgraf, J. Kuhl, H. Giessen, "On the reinterpretation of resonances in split-ring-resonators at normal incidence", Opt. Express 14, 8827-8836 (2006).

53. T. Corrigan, P. Kolb, A. Sushkov, H. Drew, D. Schmadel, R. Phaneuf, "Optical plasmonic resonances in split-ring resonator structures: an improved LC model", Opt. Express 16, 19850-19864 (2008).

54. K. Aydin, I. Pryce, H. Atwater, "Symmetry breaking and strong coupling in planar optical metamaterials", Opt. Express 18, 13407-13417 (2010).

55. K. Haupt, K. Mosbach. "Molecularly imprinted polymers and their use in biomimetic sensors", Chemical Reviews, 100, 2495-2504 (2000).

56. D. Lin-Vien, N. B. Colthup, W. G. Fateley, J. G. Grasselli, "The handbook of infrared and Raman characteristic frequencies of organic molecules", Elsevier, (1991).

57. R. A. Nyquist, R. O. Kagel, "Handbook of infrared and raman spectra of inorganic compounds and organic salts: infrared spectra of inorganic compounds. Vol. 4", Academic press, (1972).

58. V. A. Fedetov, M. Rose, S. L. Prosvirnin, N. Papasimakis, N. I. Zheludev, "Sharp Trapped-Mode Resonances in Planar Metamaterials with a Broken Structural Symmetry", Phys. Rev. Lett. 99, 147401 (2007).

59. E. Cubukcu, S. Zhang, Y. S. Park, G. Bartal, and X. Zhang, "Split ring resonator sensors for infrared detection of single molecular monolayers," Appl. Phys. Lett. 95(4), 043113 (2009).

60. B. Lahiri, S. G. McMeekin, R. M. De La Rue, N. P. Johnson, "Enhanced Fano resonance of organic material films deposited on arrays of asymmetric split-ring resonators (A-SRRs)", Opt. Express 21, 9343-9352 (2013).

61. A. Balamurugan, S. Kannan, V. Selvaraj, and S. Rajeswari, "Development and spectral characterization of Poly(Methyl Methacrylate) /Hydroxyapatite composite for biomedical applications", Trends Biomaterials Artif. Organs. 18, 41–45 (2004).

62. I. Zailer, J. E. F. Frost, V. Chabasseur-Molyneux, C. J. B. Ford, M. Pepper, "Crosslinked PMMA as a high-resolution negative resist for electron beam lithography and applications for physics of low-dimensional structures", Semiconductor science and technology, 11(8), 1235 (1996).

63. C. Wochnowski, S. Metev, G. Sepold. "UV–laser-assisted modification of the optical properties of polymethylmethacrylate", Applied surface science, 154, 706-711 (2000).

64. B, Lahiri, "Split Ring Resonator (SRR) Based Metamaterials", (Doctoral dissertation, Faculty of Engineering, University of Glasgow) (2010).

65. G. Tan, M. Lemon, D. Jones, R. French, "Optical properties and London dispersion interaction of amorphous and crystalline {SiO2} determined by vacuum ultraviolet spectroscopy and spectroscopic ellipsometry". Physical Review B 72, 205117 (2005).

66. D. F. Edwards, E. Ochoa. "Infrared refractive index of silicon", Applied optics 19(24) 4130-4131 (1980).

67. E. D. Palik, "Handbook of Optical Constants of Solids, Volume 3", Academic Press (1998).

68. R. Kitamura, L. Pilon, M. Jonasz, "Optical constants of silica glass from extreme ultraviolet to far infrared at near room temperature", Applied Optics, 46(33), 8118-8133 (2007).

69. C. Y. Chen, T. J. Yen, "Control of polarization-dependent permittivity in split-ring resonators under electric excitation", Journal of Physics D: Applied Physics, 42(18), 185402 (2009).

70. S. Linden, C. Enrich, M. Wegener, J. Zhou, T. Koschny, C. M. Soukoulis, "Magnetic Response of Metamaterials at 100 Terahertz", Science, 306 (5700), 1351-1353 (2004).

71. P. Nunes, N. Mortensen, J. Kutter, K. Mogensen, "Photonic crystal resonator integrated in a microfluidic system", Opt. Lett. 33, 1623-1625 (2008).

72. L. Y. Tobing, L. Tjahjana, D. H. Zhang, Q. Zhang, Q. Xiong, "Deep subwavelength fourfold rotationally symmetric split-ring-resonator metamaterials for highly sensitive and robust biosensing platform", Scientific reports 3, 2437 (2013).

73. S. Zhang, W. Fan, N. C. Panoiu, K. J. Malloy, R. M. Osgood and S. R. J. Brueck, "Near-infrared double negative metamaterials", Opt. Express 13, 4922-4930 (2005).

74. S. Zhang, W. Fan, K. J. Malloy, S. R. J. Brueck, N. C. Panoiu and R. M. Osgood, J. Opt. Soc. Am. B. 23, 434-438 (2006).

75. G. Dolling, C. Enrich, M. Wegener, C.M. Soukoulis and S. Linden, Opt. Lett. 31, 1800-1802 (2006).

76. S. Zhang, W. Fan, K. J. Malloy, S. R. J. Brueck, N. C. Panoiu, R. M. Osgood, JOSA B, 23 (3), 434-438 (2006).

77. C. Garcia-Meca, J. Hurtado, J. Marti, A. Martinez, W. Dickson and A. V. Zayats, "Low-loss multilayered metamaterial exhibiting a negative index of refraction at visible wavelengths", Phys. Rev. Lett. 106, 067402 (2011).

78. S. Xiao, U. K. Chettiar, A. V. Kildishev, V. P. Drachev and V. M. Shalaev, "Yellow-light negative-index metamaterials", Opt. Lett. 34, 3478-3480 (2009).

79. Dolling, G., Wegener, M., Soukoulis, C. M. & Linden, S. Negative-index metamaterial at 780 nm wavelength. Opt. Lett. 32, 53–55 (2007).

80. J. Valentine, S. Zhang, T. Zentgraf, E. Ulin-Avila, D. A. Genov, G. Bartal and X. Zhang, "Three-dimensional optical metamaterial with a negative refractive index", Nature 455, 376-379 (2008).

81. G. Dolling, M. Wegener, C. M. Soukoulis, S. Linden, "Design-related losses of double-fishnet negative-index photonic metamaterials", Optics Express, 15, 11536-11541 (2007).

82. J. Zhou, T. Koschny, M. Kafesaki, C. M. Soukoulis, "Negative refractive index response of weakly and strongly coupled optical metamaterials", Phys. Rev. B., 80, 035109 (2009).

83. S. Enoch, G. Tayeb, P. Sabouroux, N. Guérin, and P. Vincent, "A Metamaterial for Directive Emission", Phys. Rev. Lett. 89, 213902. (2002).

84. R. W. Ziolkowski, A. D. Kipple, "Application of double negative materials to increase the power radiated by electrically small antennas", Antennas and Propagation, IEEE Transactions on, 51 (10), 2626-2640, (2003).

85. M. Kafesaki, I. Tsiapa, N. Katsarakis, T. Koschny, C. M. Soukoulis and E. N. Economou, "Left-handed metamaterials: The fishnet structure and its variations", Phys. Rev. B. 75, 235114 (2007).

86. Z. Ku, J. Zhang, S. R. J. Brueck, "Bi-anisotropy of multiple-layer fishnet negative-index metamaterials due to angled sidewalls", Opt. Express 17, 6782-6789 (2009).

87. U. K. Chettiar, A. V. Kildishev, H.-K. Yuan, W. Cai, S. Xiao, V. P. Drachev, V. M. Shalaev, "Dual-Band Negative Index Metamaterial: Double-Negative at 813 nm and Single-Negative at 772 nm," Opt. Lett, 32, 1671-1673 (2007).

88. T. W. Ebbesen, H. J. Lezec, H. F. Ghaemi, T. Thio, P. A. Wolff, "Extraordinary optical transmission through sub-wavelength hole arrays", Nature 391, 667-669 (1998).

89. C. Garcia-Meca, R. Ortuno, F. J. Rodriguez-Fortuno, J. Marti and A. Martinez, "Negative refractive index metamaterials aided by extraordinary optical transmission", Opt. Express 17, 6026-6031 (2009).

90. I. Bergmair, B. Dastmalchi, M. Mergmair, A. Saeed, W. Hilber, G. Hesser, C. Helgert, E. Pshenay-Severin, T. Pertsch, E. B. Kley, U. Hubner, N. H. Shen, R. Penciu, M. Kafesaki, C. M. Soukoulis, K. Hingerl, M. Muehlberger and R. Schoeftner, "Single and multilayer metamaterials fabricated by nanoimprint lithography", Nanotechnology 22, 325301 (2011).

91. A. Minovich, D.N. Neshev, D.A. Powell, I.V. Shadrivov, Y.S. Kivshar, "Tunable fishnet metamaterials infiltrated by liquid crystals", Applied Physics Letters 96 (19), 193103 (2010).

92. A. Minovich, D. N. Neshev, D. A. Powell, Y. S. Kivshar, "Influence of the substrate on negative index fishnet metamaterials" Optics Communications, 283(23), 4770-4774 (2010).

93. J. Yang, C. Sauvan, H. T. Liu, and P. Lalanne, "Theory of Fishnet Negative-Index Optical Metamaterials", Phys. Rev. Lett. 107, 043903 (2011).

94. P. Ding, E.J. Liang, W.Q. Hu, L. Zhang, Q. Zhou, Q.Z. Xue, "Numerical simulations of terahertz double-negative metamaterial with isotropic-like fishnet structure", Photonics and Nanostructures - Fundamentals and Applications, 7, 92-100 (2009).

95. Y. Zhang, W. Jin, X. Dong, Z. Zhao, X. Duan, "Asymmetric fishnet metamaterials with strong optical activity", Opt. Express 20, 10776-10787 (2012).

96. W. Wu, E. Kim, E. Ponizovskaya, Y. Liu, Z. Yu, N. Fang, Y. R. Shen, A. M. Bratkovsky, W. Tong, C. Sun, X. Zhang, S. Y. Wang, R. S. Williams, "Optical Metamaterials at near and mid-IR range fabricated by nanoimprint lithography," Appl. Phys. A-Mater. Sci. Process. 87 (2), 143-150 (2007).

97. L. Gao, K. Shigeta, A. Vazquez-Guardado, C.J. Progler, G.R. Bogart, J.A. Rogers, D. Chanda, "Nanoimprinting techniques for large-area three-dimensional negative index metamaterials with operation in the visible and telecom bands.", ACS Nano. 8(6), 5535-5542 (2014).

98. D. Chanda, K. Shigeta, S. Gupta, T. Cain, A. Carlson, A. Mihi, A. J. Baca, G. R. Bogart, P. Braun, J. A. Rogers, "Large-area flexible 3D optical negative index metamaterial formed by nanotransfer printing", Nat. Nano. 6, 402-407 (2011).

99. J. L. Skinner, L. L. Hunter, A. A. Talin, J. Provine, D. A. Horsley, "Large-area subwavelength aperture arrays fabricated using nanoimprint lithography," IEEE Transactions on Nanotechnology, Vol. 7, No. 5, 527-531, (2008).

100. S. Sung, C. Kim, D. Choi, J. Lee, J. Choi, E. Lee, "Direct Nanoimprint of Metal Bilayer for Tunable Metal Photonic Properties", Jpn. J. Appl. Phys. 52 10MC09 (2013).

101. J. Shi, J. Chen, D. Decanini, Y. Chen, A.-M. Haghiri-Gosnet, "Fabrication and characterization of metallic nanocavities by nanoimprint lithography", Microelectron. Eng. 86, 596 (2009).

102. Z. Jaksic, D. Tanaskovic, J. Matovic, "Fishnet-Based Metamaterials: Spectral Tuning Through Adsorption Mechanism", ACTA Physica Polonica A, 116, 625-627 (2009).

103. Z. Jaksic, S. M. Vukovic, J. Buha, J. Matovic, "Nanomembrane-based plasmonics", J. Nanophoton, 5 (1), 051818 (2011).

104. Z. Jaksic, Z. Popovic, I Djerdj, Z. K. Jacimovic, K. Radulovic, "Functionalization of plasmonic metamaterials utilizing metal-organic framework thin films", Phys. Scr. T149 (2012).

105. I. E. Khodasevych, C. M. Shah, S. Sriram, M. Bhaskaran, W. Withayachumnankul, B. S. Y. Ung, H. Lin, W. S. T. Rowe, D. Abbott, A. Mitchell, "Elastomeric silicone substrates for terahertz fishnet metamaterials", Appl. Phys. Lett. 100, 061101 (2012).

106. G. Dolling, C. Enkrich, M. Wegener, C.M. Soukoulis, S. Linden, "Low-loss negative-index metamaterial at telecommunication wavelengths", Opt. Lett. 31, 1800-1802 (2006).

107. P. B. Johnson and R. W. Christy, "Optical constants of the noble metals", Phys. Rev. B 6, 4370 (1972).

108. D. R. Smith, S. Schultz, P. Markos, and C. M. Soukoulis, "Determination of effective permittivity and permeability of metamaterials from reflection and transmission coefficients", Phys. Rev. B 65, 195104 (2002).

109. T. Koschny, P. Markos, E. N. Economou, D. R. Smith, D. C Vier and C. M. Soukoulis, "Impact of inherent periodic structure on effective medium description of left-handed and related metamaterials", Phys. Rev. B. 71, 245105 (2005).

110. J. Zhou, T. Koschny, M. Kafesaki and C. M. Soukoulis, "Negative refractive index response of weakly and strongly coupled optical metamaterials", Phys. Rev. B. 80, 035109 (2009).

111. C. Rockstuhl, C. Menzel, T. Paul, T. Pertsch, F. Lederer, "Light propagation in a fishnet metamaterial", Phys. Rev. B. 78 155102 (2008).

112. S. S. Kruk, D. A. Powell, A. Minovich, D. N. Neshev, Y. S. Kivshar, "Spatial dispersion of multilayer fishnet metamaterials", Optics Exp. 20(14), 15100-15105 (2012).

113. X. Chen, T. M. Grzegorczyk, B. Wu, J. Pacheco, J. A. Kong, "Robust method to retrieve the constitutive effective parameters of metamaterials", Phys. Rev. E 70, 016608 (2004).

114. V. M. Shalaev, W. Cai, U. K. Chettiar, H. Yuan, A. K. Sarychev, V. P. Drachev, A. V. Kildishev, "Negative index of refraction in optical metamaterials", Optics Lett., 30 (24), 3356-3358 (2005).

115. www.p3sens-project.eu, 20th October 2014

116. W. A. Pulsinelli, "The therapeutic window in ischemic brain injury", Curr. Opinion Neurol., 8, 3-5 (1995).

117. M. D. Ginsberg, W. A. Pulsinelli, "The ischemic penumbra, injury thresholds and the therapeutic window for acute stroke", Ann. Neurol. 36, 553-554 (1994).

118. R. L. Sacco, P. A. Wolf, W. B. Kannel, P. M. McNamara, "Survival and recurrence following stroke: The Framingham study", Stroke, 13, 290-295 (1982).

119. W. Whiteley, M. C. Tseng, P. Sandercock, "Blood biomarkers in the diagnosis of ischemic stroke: a systematic review", Stroke 39 (10), 2902-2909 (2008).

120. W. Whiteley, W. L. Chong, A. Sengupta, P. Sandercock, "Blood markers for the prognosis of ischemic stroke: a systematic review", Stroke 40(5), 380-389 (2009).

121. C.M. Laborde, L. Mourino-Alvarez, F. Akerstrom, L.R. Padial, F. Vivanco, F. Gil-Dones, M.G. Barderas, "Potential blood biomarkers for stroke", Expert Rev Proteomics, 9 (4), 437-449 (2012).

122. M. A. Reynolds, H. J. Kirchick, J. R. Dahlen, J. M. Anderberg, P. H. McPherson, K. K. Nakamura, D. T. Laskowitz, G. E. Valkirs, K. F. Buechler, "Early Biomarkers of Stroke", Clinical Chemistry, 49(10), 1733-1739 (2003).

123. F. Dortu, H. Egger, K. Kolari, T. Haatainen, P. Furjes, Z. Fekete, D. Bernier, G. Sharp, B. Lahiri, S. Kurunczi, J.-C. Sanchez, N. Turck, P. Petrik, D. Patko, R. Horvath, S. Eiden, T. Aalto, S. Watts, N. P. Johnson, R. M. De La Rue, D. Giannone, "Design and process development of a photonic crystal polymer biosensor for point-of-care diagnostics", Proc. SPIE 8087, Clinical and Biomedical Spectroscopy and Imaging II, 80870D (2011).

124. R. Waldhäusl, B. Schnabel, P. Dannberg, E. Kley, A. Bräuer, and W. Karthe, "Efficient Coupling into Polymer Waveguides by Gratings", Appl. Opt. 36, 9383-9390 (1997).

125. M. Moharam, T. Gaylord, "Rigorous coupled-wave analysis of planar-grating diffraction", J. Opt. Soc. Am. 71, 811-818 (1981).

126. Z. Can, S. Jing-Hua, X. Xi, S. Wei-Min, Z. Xiao-Jun, C. Tao, Y. Jin-Zhong, Y. Yu-De, "High Efficiency Grating Coupler for Coupling between Single-Mode Fiber and SOI Waveguides", Chinese Phys. Lett. 30, 014207-014204 (2013).

127. L. Eldada, L. W. Shacklette, "Advances in polymer integrated optics", Selected Topics in Quantum Electronics, IEEE Journal of, 6(1), 54-68 (2000).

128. M. Wang, J. Hiltunen, S. Uusitalo, J. Puustinen, J. Lappalainen, P. Karioja, R. Myllylä, "Fabrication of optical inverted-rib waveguides using UV-imprinting, Microelectron. Eng. 88(2) 175-178 (2011).

129. E. Wagner, R. Dandliker, K. Spenner, "Sensors, Optical Sensors", John Wiley & Sons (2008), page 162.

130. K. Okamoto, "Fundamentals of Optical Waveguides", Gulf Professional Publishing (2000), page 39.

131. William N. Sharpe, "Springer Handbook of Experimental Solid Mechanics", Spinger (2008), page 363.

132. V. E. Borisenko, S. Ossicini, "What is What in the Nanoworld: A Handbook on Nanoscience and Nanotechnology", John Wiley & Sons (2013), page 111.

133. R. Bruck, E. Melnik, P. Muellner, R. Hainberger, M. Lämmerhofer, "Integrated polymer-based Mach-Zehnder interferometer label-free streptavidin biosensor compatible with injection molding", Biosens Bioelectron. 26(9):3832-3837 (2011).

134. J. Homola, "Surface plasmon resonance sensors for detection of chemical and biological species." Chemical reviews 108(2) 462-493 (2008).

135. D. Giannone, F. Dortu, D. Bernier, N. P. Johnson, G. J. Sharp, L. Hou ; A. Z. Khokhar, P. Fürjes, S. Kurunczi, P. Petrik, R. Horvath, T. Aalto, K. Kolari, S. Ylinen, T. Haatainen, H. Egger, "NIL fabrication of a polymer-based photonic sensor device in P3SENS project", Proc. SPIE 8435, Organic Photonics V, 843529 (2012).

136. C. Lu, B. Yang B, "High refractive index organic–inorganic nanocomposites: design, synthesis and application", J. Mat. Chem. 19, 2884-2901 (2009).

137. H. W. Su, W. C. Chen, "High refractive index polyimide–nanocrystalline-titania hybrid optical materials", J. Mat. Chem. 18, 1139-1145 (2008).

138. Y. Imai, A. Terahara, Y. Hakuta, K. Matsui, H. Hayashi, N. Ueno "Transparent poly(bisphenol A carbonate)-based nanocomposites with high refractive index nanoparticles", Eur. Polym. J. 45, 630-638 (2009).

139. A. Cattoni, P. Ghenuche, A. M. Haghiri-Gosnet, D. Decanini, J. Chen, J. L. Pelouard, S. Collin, "λ3/1000 plasmonic nanocavities for biosensing fabricated by soft UV nanoimprint lithography", Nano Lett. 11(9), 3557-3563 (2011).

140. C. Barrios, K. Gylfason, B. Sánchez, A. Griol, H. Sohlström, M. Holgado, and R. Casquel, "Slot-waveguide biochemical sensor", Opt. Lett. 32, 3080-3082 (2007).

141. A. Minovich, D. N. Neshev, D. A. Powell, Y. S. Kivshar, "Influence of the substrate on negative index fishnet metamaterials" Optics Communications, 283(23), 4770-4774 (2010).

142. A. Di Falco, M. Ploschner, T. F. Krauss. "Flexible metamaterials at visible wavelengths." New Journal of Physics 12(11) 113006 (2010).

143. H. Xu, W. Rao, J. Meng, Y. Shen, C. Jin, X. Wang, "Inverted hemispherical mask colloidal lithography", Nanotechnology, 20, 465608 (2009).

144. I. M. Pryce, K. Aydin, Y. A. Kelaita, R. M. Briggs, H. A. Atwater, "Highly Strained Compliant Optical Metamaterials with Large Frequency Tunability", Nano Lett. 10(10), 4222-4227 (2010).

145. R. A. Shelby, D. R. Smith, S. Schultz, "Experimental Verification of a Negative Index of Refraction", Science, 292 (5514), 77-79 (2001).